DISSERTATION FOR THE DEGREE OF DOCTOR OF PHILOSOPHY (PHD)

Studying interactions between peptide toxins and voltage-gated K^+ channels at the molecular level

by Muhammad Umair Naseem

UNIVERSITY OF DEBRECEN
DOCTORAL SCHOOL OF MOLECULAR MEDICINE

DEBRECEN, 2023

DISSERTATION FOR THE DEGREE OF DOCTOR OF PHILOSOPHY (PHD)

Studying interactions between peptide toxins and voltage-gated K^+ channels at the molecular level

by Muhammad Umair Naseem

Supervisor: Prof. György Panyi

UNIVERSITY OF DEBRECEN
DOCTORAL SCHOOL OF MOLECULAR MEDICINE

DEBRECEN, 2023

TABLE OF CONTENTS

LIST OF ABBREVIATIONS

AOX1: Alcohol oxidase 1

APC: Antigen presenting cell

BMGY: Buffered Glycerol-complex Medium

BMMY: Buffered Methanol-complex Medium

CHO: Chinese hamster ovary

ChTx: Charybdotoxin

CRAC: Calcium release- activated calcium channel

CsF: Cesium fluoride

DAG: Diacyl glycerol

EGTA: Ethylene glycol tetraacetic acid

GFP: Green fluorescent protein

HEK: Human embryonic kidney

HEPES: N-2-hydroxyethylpiperazine-N-2-ethane sulfonic acid

IL2R: Interleukin 2 receptor

IP_3: Inositol 1,4,5-trisphosphate

K_{Ca}: Calcium-activated potassium ion channel

KTxs: Potassium channel inhibitor toxins

KTX: kaliotoxin

K_V: Voltage-gated potassium ion channel

LPS: Lipopolysaccharide

MES: 4-Morpholineethanesulfonic acid

Na_V: Voltage-gated sodium ion channel

PBMC: Peripheral blood mononuclear cell

PBS: Phosphate buffer solution

PHA: Phytohemagglutinin A

PIP_2: Phosphatidylinositol 4,5-bisphosphate

PLC-γ: Phospholipase C gamma

RCF: Remaining current fraction

RP-HPLC: Reversed phase high performance liquid chromatography

SDS-PAGE: Sodium dodecyl-sulfate polyacrylamide gel electrophoresis

STIM: Stromal interaction molecule

τ_{act}: Activation time constant

T_{CM}: Central memory T cell

TCR: T cell receptor

TEA^+: Tetraethylammonium-Cl

T_{EM}: Effector memory T cell

TFA: Trifluoroacetic acid

τ_{inact}: Inactivation time constant

TrMgTx: Tagged recombinant margatoxin

UrMgTx: Untagged recombinant margatoxin

CD: Cluster of differentiation

CCR: Chemokine receptor

1. PREFACE

Potassium ion (K^+) channels regulate various physiological functions in both excitable and non-excitable cells. In human T-cells K^+ channels maintain the negative resting membrane potential by the K^+ efflux and thus, regulate Ca^{2+} signaling required for T-cell proliferation and production of cytokines. Voltage-gated K^+ channel $K_V1.3$ is drastically upregulated in effector memory T (T_{EM}) cells that are key mediators of pathological autoinflammation. Since selective blockade of $K_V1.3$ persistently suppresses activation and proliferation of T_{EM} cells, $K_V1.3$ has become an attractive therapeutic target to treat several autoimmune diseases driven by T_{EM} cells such as rheumatoid arthritis and multiple sclerosis. Emerging evidence implicates $K_V1.3$ in activation of microglia, brain-resident macrophages. Thus, $K_V1.3$ is also a potential drug target in treatment of neuroinflammatory disorder such as Alzheimer's and Parkinson's diseases.

Scorpion venom contains a complex mixture of peptide toxins which can bind to K^+ channels with great affinity and module their function. Several peptide toxins have been derived from scorpion venom which inhibit $K_V1.3$ with pico-nanomolar affinity and high selectivity over other K^+ channels, for example, Margatoxin (K_d = 11 pM),) Vm24 (K_d = 3 pM) and HsTX1 (K_d = 11 pM). Their inherent high affinity for $K_V1.3$ makes them attractive lead compounds for drug development and designing a diagnostic tool for autoimmune diseases. These toxins consist of 23-40 amino acid residues and share a common structural motif consisting of an α-helix/β-sheet scaffold stabilized by 3-4 disulfide bridges. A typical functional dyad that consists of a lysine residue and an aromatic residue is also considered a common feature of these toxins. The critically positioned lysine of the dyad that protrudes into the selectivity filter of channel is essential for blocking the current. However, some scorpion toxins completely lacking this dyad, yet block $K_V1.3$ with nanomolar affinity, also exist. Thus, their diverse structural nature and potential application in $K_V1.3$ mediated autoimmune diseases encourages the exploration of different scorpion venoms from various geographic regions for novel toxins.

In the present work, first we describe the pharmacological and functional properties of a novel peptide toxin isolated from Colombian scorpion *Centruroides margaritatus*. Secondly, we characterize a fluorescent analogue of HsTX1[R14A], a potent $K_V1.3$ inhibitor peptide, as a new tool for selective visualization of $K_V1.3$ expression. Thirdly, to meet the demand of large quantities of peptide toxins for pharmacology and therapeutic development, we aim to optimize *Pichia pastoris* expression system for high-level production of margatoxin as an exemplary peptide.

2. INTRODUCTION AND SCIENTIFIC BACKGROUND

2.1 Ion channels

Ion channels are essential membrane proteins that span across the cell membrane to form a hydrophilic pore, driving the selective ions down the electrochemical gradient at a rate of 10-100 million per second. They are expressed in all cell types of the human body and play a crucial role in regulating fundamental physiological functions. From a functional point of view, most of the channels can make transition between conducting (open) and non-conducting (inactive or closed) states [1, 2]. Ion channels can be classified based on their ion selectivity (*e.g.*, K^+, Ca^{2+}, H^+, Cl^-, highly-, mildly- or non-selective), gating mechanism (voltage-gated, signal-gated, ligand-gated, stretch-gated, *etc*.), ionic current direction (outward-, inward- or non-rectifier) [3]. This study mainly revolves around voltage-gated potassium channels so this will be discussed in detail below.

2.1.1 Overview of potassium channels

Potassium channels are multimers of α-subunits which share a highly conserved pore loop (P), that contains the selectivity filter (SF) signature sequence and allow selective transport of K^+ ions across cell membrane. However, these subunits bear a considerable structural diversity among the sensing domains that permits channel gating in response to a variety of signals [4, 5]. K^+ channels are critical in the regulation of multiple physiological processes not only in excitable cells such as neuronal excitability, axonal conduction, hormone and neurotransmitters secretion, but also in non-excitable cells where they participate in controlling cell volume regulation, calcium signaling, proliferation and apoptosis [6, 7]. For these processes, the human genome contains 78 different K^+ channel genes.

According to the International Union of Basic and Clinical Pharmacology's (IUPHAR) Concise Guide to Pharmacology 2019/20 [3], K^+ channels have been categorized into four groups based on the amino acid sequence similarity and the number of transmembrane α helices (TMs) which can be 2, 4, 6 or 7 per subunit as represented in Fig. 1. These α helices are denoted by S0-S6 and commonly used to identify the TM α helices in the ion channels. (i) Inward rectifier K^+ channels (Kir) are assembled by the tetramerization of individual subunits formed by 2TM/1P. Here P is between S1 and S2, the four pore loops will construct one functional pore (Fig. 1). The two transmembrane helices that surround the pore loop and the pore loop itself together will be referred to as pore domain (PD) thereafter (*i.e.*, in case of Kir, S1-P-S2 forms

the PD). Kir channels allow the conduction of K^+ ions into the cell. (ii) The K2P channels (leak or background channels) formed by dimerization of two subunits, each containing 4 transmembrane helices and 2 pore loops (4TM/2P). The first pore loop, P1, is between S1 and S2 and the second pore loop, P2, is between S3 and S4. Essentially, one K2P subunit contains two PDs, the dimerization of two of these subunits will result in a channel that has two functional pores. (iii) K^+ channels consisting of tetramers of 6TM/1P subunits with intracellular N- and C- terminus. The P is located between S5 and S6. This group includes voltage-gated K^+ channels (K_V) and the small- and intermediate- conductance Ca^{2+}-activated K^+ channels (K_{Ca}). (iv) Members of large-conductance K_{Ca} channels are present in the tetrameric assembly of 7TM/1P subunits with extracellular N-terminus TM α helix (S0) and P between S5-S6 [5, 8].

2.1.2 Voltage-gated potassium channels (K_V)

This is an evolutionarily conserved, large and diverse family of channels with high K^+ selectivity. A fully functional K_V channel requires a tetrameric organization of 60-68 kDa polypeptide chains denoted as α-subunits, with the ion conducting pore lying in the axis of four-fold symmetric structure as depicted in Fig. 1. Typically, the polypeptide chain contains six hydrophobic α helices (S1-S6). Voltage-sensing domain (VSD) is formed by the first 4 α-helices (S1-S4) and the pore domain (PD) responsible for K^+ ion conduction is formed by the S5 and S6 α-helices and the connecting pore loop (P) of each polypeptide chains [6, 9]. K_V channel family includes 12 subfamilies consisting of different α-subunits (K_V1-K_V12) and exhibit significant heterogeneity based on their subunit composition, accessory proteins, presence of modifier subunits and post-translational modifications [7]. These subfamilies can be classified according to their functional and biophysical properties. From functional point of view, two distinguished groups (i) conductive group consists of 36 genes of K_V channels: *KCNA* to *KCND* (K_V1.x - K_V4.x corresponding to Shaker, Shab, Shaw, and Shal channels, respectively, in *Drosophila melanogaster*), *KCNQ* (K_V7 family), ether-a-go-go gene (Eag or K_V10.x), ether-a-go-go-related gene (Erg or K_V11.x) and Elk gene (K_V12.x), (ii) nonconductive group of gating modulators: *KCNF* (K_V5), *KCNG* (K_V6), *KCNV* (K_V8), and *KCNS* (K_V9) [3, 5]. Of the conductive group the macroscopic currents can be either characterized as (i) slow or non-inactivating also known as delayed rectifier, and (ii) rapidly inactivating channel which generate A-type current, however, depending on the voltage protocols used to evoke the currents molecular composition of the channels macroscopic currents may have very different shapes. This functional diversity of the recorded K^+ currents stems from the expression of a specific subset of K_V channels in different cell types, hetero-multimerization among the same

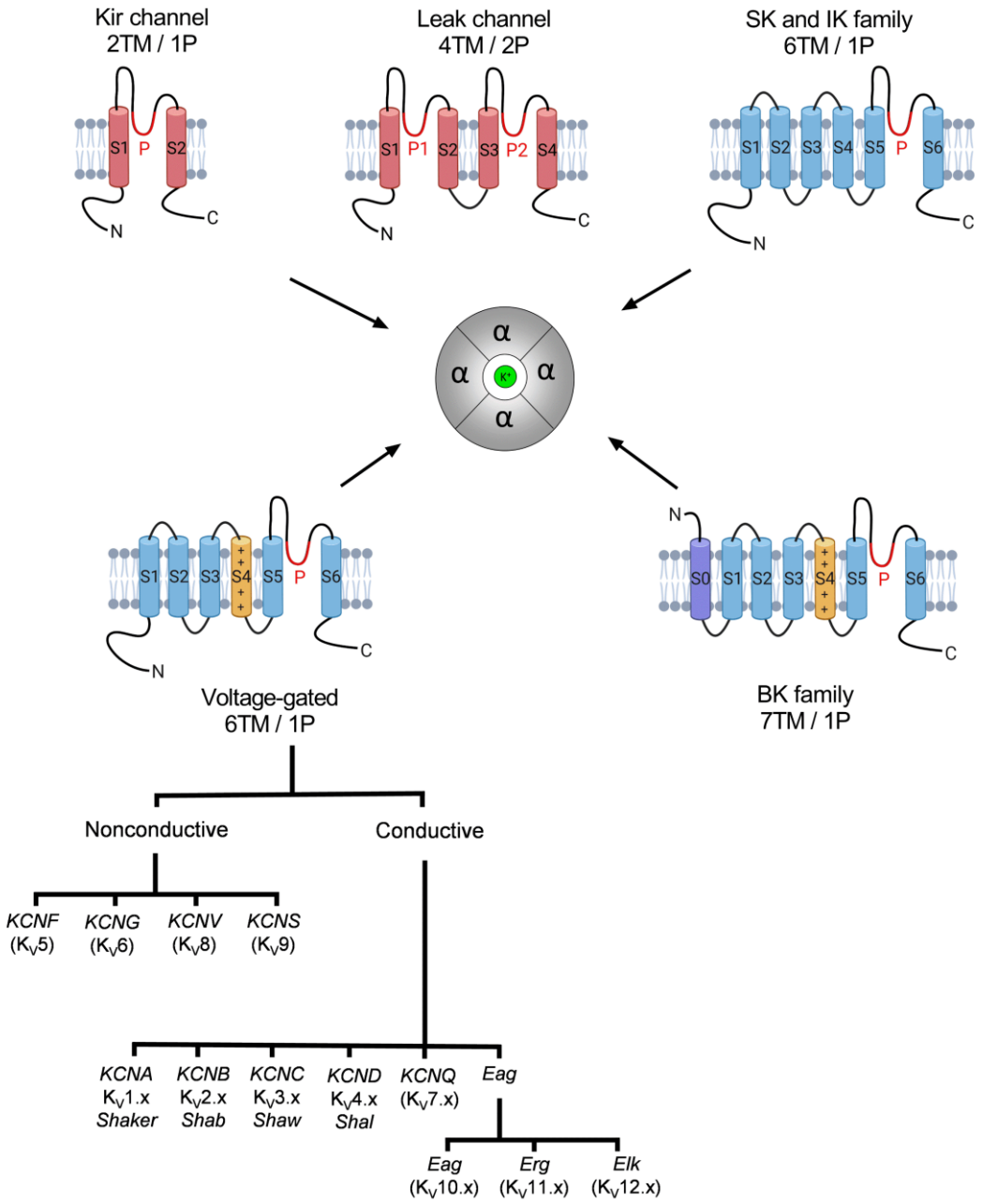

Figure 1: **K^+ channel families represented according to their subunit structure [5, 7].** Inward rectifier K^+ channel (Kir); 2 transmembrane helices (TM) with one pore (1P), leak or background K^+ channel; 4 TM with 2P, voltage-gated (K_V) and Ca^{2+}-gated small- and intermediate- conductance K^+ channels (SK and IK); 6 TM with 1P, Ca^{2+}- and voltage-gated big conductance K^+ channel (BK); 7 TM with 1P. The 6 TM class having voltage-sensor domain can be subdivided into; conductive group which includes voltage-gated (K_V1-4), voltage-gated KCNQ-type, and ether-a-go-go (Eag) K^+ channels, and nonconductive group which includes members of K_V5, K_V6, K_V8 and K_V9. Inset: representation of tetrameric assembly of α-subunits to form a pore for K^+ ion conduction.

family of K^+ channels subunits or with the silent family subunits and multimerization of α-subunits with accessory β-subunits [5, 9]. Table 1 summarizes physiological properties of those K^+ channels that I studied in this work.

2.1.3 Ca^{2+}-activated potassium channels (K_{Ca})

The K_{Ca} channels are activated by intracellular Ca^{2+} and can be subdivided into two major groups [10]. (i) The small- (SK, $K_{Ca}2$) and intermediate-conductance (IK, $K_{Ca}3.1$) K_{Ca} channels are structurally homologous to K_V channels in their TM α-helices and PD (S5-P-S6). However, in contrast to K_V channels, they have less positively charged residues in their S4 α-helix of the VSD, hence, making them insensitive to changes in the transmembrane voltage. (ii) The second group contains the large-conductance (BK, MaxiK, $K_{Ca}1.1$) channels which are activated by both voltage and rise in the cytosolic Ca^{2+}. This group is also structurally distinguished from other K_{Ca} channels as it has an extra TM α-helix (S0) which renders its N-terminus to be localized extracellularly [11, 12]. The K_{Ca} channel family members can also be differentiated based on their unitary K^+ conductance. $K_{Ca}2$ and $K_{Ca}3.1$ channels show conductance of ~10 pS and ~40 pS, respectively, in contrary $K_{Ca}1.1$ has a remarkable single channel conductance of ~200 pS [11].

The $K_{Ca}2$ family has three members, $K_{Ca}2.1$ (SK1, *KCNN1*), $K_{Ca}2.2$ (SK2, *KCNN2*), and $K_{Ca}2.3$ (SK3, *KCNN3*) and they are highly similar across their TM with 80-90% similarity but divergent at their terminus (N and C) regions. $K_{Ca}2$ channels are exclusively expressed in the nervous system [13]. The $K_{Ca}3$ family has only one member, $K_{Ca}3.1$ (IK, SK4, *KCNN4*) which shows only ~40% similarity with the three $K_{Ca}2$ channels. $K_{Ca}3.1$ is present in peripheral tissues such as lymphocytes, erythrocytes, pancreas, lungs, and placenta. The calcium-dependent activation of both families $K_{Ca}2$ and $K_{Ca}3$ is mediated by calmodulin (CaM) that is constitutively bound to the CaM-binding domain to intracellular C-terminus of the channel [14, 15].

Among the BK channel family, the pore-forming polypeptide chain of $K_{Ca}1.1$ channel is encoded by a single gene (*KCNMA1*, Slo) in humans [11]. Each subunit in the tetrameric of $K_{Ca}1.1$ channel has two high affinity Ca^{2+} binding sites which altogether assemble as ring-like structure which is called as gating ring. It is ubiquitously expressed and its phenotype among tissues relies on its alternative splicing, phosphorylation, and association with regulatory subunits. Physiological functions include hyperpolarization of smooth muscle cells and initiation of neurotransmitter release [10, 27].

Table 1: Overview of physiological roles of different ion channels involved in this study

No	Ion Channel	Tissue specific expression and function
1	$K_V1.1$	Present in CNS, skeletal muscles, kidney, and retina. Majorly involve in nerve signaling and regulation of membrane potential [5, 16]
2	$K_V1.2$	Similar distribution pattern to $K_V1.1$ in CNS, smooth muscles, Schwann cells, and pancreatic β-cells. It associates in maintaining membrane potential and modulating electrical excitability in neurons [9, 17]
3	$K_V1.3$	Mainly expresses in immune and CNS systems, additionally in osteoclasts, progenitor lymphocytes, microglia, macrophages pancreatic islets of Langerhans, oligodendrocytes, lung, and spleen. It plays an important role in activation of T lymphocytes and microglia [18, 19]
4	$K_V1.4$	Present in the brain, lung carcinoma cells, skeletal and cardiac myocytes, and pancreatic cells. It plays an important role in the post-hyperpolarization of neurons [20, 21]
5	$K_V1.5$	It expresses in cardiac atrial and ventricular myocytes, aorta, stomach, colon, smooth muscle cells, macrophages, and brain tissue. It has properties like the ultra-rapidly activating I_{Kur} current in the heart and its blockage may cause fibrillation [22, 23]
6	$K_V1.6$	Present in cardiac fibroblast, murine colon myocytes, and brain tissues. It regulates membrane potential in neurons [9, 24]
7	$K_V11.1$	It is expressed in the heart, neuroblastoma, brain, kidney, liver, lung, ovary, pancreas, testis, prostate, small intestine, microglia. The physiological function of the channel is to establish myocardial action potentials [9, 25, 26]
8	$K_{Ca}1.1$	found in smooth muscle, brain, mitochondria, kidney, and cochlea. hyperpolarization of smooth muscle cells and initiation of neurotransmitter release [10, 27]
9	$K_{Ca}3.1$	IK_{Ca} channel expression has been observed in lymphocytes, smooth muscle cells, red blood cells and fibroblasts. They function in concert with the $K_V1.3$ channel to regulate lymphocyte activation and proliferation by providing the negative membrane potential [10, 19]
10	$Na_V1.4$	Present in skeletal muscles and involves in action potential initiation and transmission [28, 29]
11	$Na_V1.5$	Present in cardiac muscle and initiates action potential, defects in function may cause disorders *e.g*., Long QT syndrome and arrhythmia [28, 30]
12	H_V1	It primarily expressed in phagocytes in the immune system and in tissue-resident microglia of CNS and regulates reactive oxygen species (ROS) production, cytosolic pH, migration, and proliferation [31, 32]

2.1.4 Voltage-activated sodium channels (Na_V)

The mammalian Na_V channels consist of a pseudotetrameric pore-forming α-subunit that can be associated with one or two β-subunits. The α-subunit is a large and single-chain polypeptide composed of four homologous domains (DI-DIV); each domain has six TM α helices. S1-S4 form the VSD with positively charged S4 in each domain which is involved in voltage-gating. The S5-P-S6 of each domain contribute to the formation of the pore and selectivity filter for Na^+ ion conduction [29]. In humans there are nine different Nav α-subunits

genes which encode $Na_V1.1$-$Na_V1.9$ channels. Na_V channels are also characterized by a tissue-specific expression profile, $Na_V1.1$-$Na_V1.3$ are expressed in brain tissues. $Na_V1.6$ is present in both the brain and peripheral nervous system, however, $Na_V1.7$-$Na_V1.9$ are mostly confined to the peripheral nervous tissues. $Na_V1.4$ and $Na_V1.5$ channels are predominantly expressed in striated skeletal muscles and cardiac muscles, respectively [30]. Different subtypes of Na_V channels have high degree of similarity (>50%) in TM and extracellular loops, making it difficult to find subtype selective modifiers [28]. One of the best-known subtypes specific Na_V inhibitors is tetrodotoxin (TTX). For $Na_V1.1$, $Na_V1.2$, $Na_V1.3$, $Na_V1.4$, $Na_V1.6$, and $Na_V1.7$ channels the IC_{50} value of TTX ranges between 1−25 nM, therefore, these channel subtypes are considered TTX-sensitive. However, $Na_V1.5$, $Na_V1.8$, and $Na_V1.9$ are blocked by high μM TTX concentration so, these subtypes are classified as TTX-insensitive [29, 33].

2.2 Molecular architecture of $K_V1.3$ channel

The first experimental details about the atomic coordinates in a potassium channel are attributed to Roderick MacKinnon and his colleagues, who determined the structure of the bacterial-derived potassium channel KcsA using X-ray crystallography in 1998 [34]. Later, the atomic structure of a voltage-dependent ion channel (K_VAP) and mammalian $K_V1.2$ channel was also reported by MacKinnon's group [35-37]. However, in the last two years there was a breakthrough regarding the structure of the human voltage-gated $K_V1.3$ ion channel. Structures of $K_V1.3$ alone, complexed with accessory subunit $K_V\beta2$, or bound to blocker Dalazatide (derivative of ShK toxin) or a nanobody inhibitor (Ablynx/Sanofi) or antibody-ShK fusion blocker were solved by cryo-electron microscopy (cryo-EM) [38-40]. The overall architecture of these $K_V1.3$ structures was coherent, and also consistent with the structures of $K_V1.2$ and the $K_V1.2$-$K_V2.1$ chimera [38].

$K_V1.3$ is one of the 8 members of the mammalian K_V1 family (*Shaker*-related) of K_V channels. The basic structural organization of K_V1 channels bears a high degree of similarity [41, 42]. The functional K_V1 channels are assembled from four non-covalently linked α-subunits of similar structure which lie approximately in symmetrical position with respect to each other (Fig. 2A) [43]. Each α-subunit is composed of a large cytoplasmic tetramerization domain called T1, 6 TM α helices called S1-S6. The voltage sensor domain (VSD) consists of first four TM α helices S1-S4 (as shown in Fig. 2B and D), with S3 having a net negative charge and S4 containing multiple positive residues in repeating RXXR motif, thus playing a prominent role in voltage-dependent channel opening [36, 37, 44-46]. S5-P-S6 of each α-

subunit contributes to form the ion conducting pore domain (PD) as illustrated in Fig. 2C and D. The extracellular loop connecting S5-S6 is called pore loop (P) which contributes to form the highly conserved selectivity filter (SF) (Fig. 2C–E), responsible for the selective permeation of K^+ ions [47]. A TXGYGD motif is present in the selectivity filter which is highly conserved among K_V channels and known as K_V signature sequence [48] as illustrated in Fig. 2E. The backbone carbonyl oxygens of the signature sequence point into the pore along the four-fold symmetry axis of channel. The filter structure is evolved to specifically coordinate dehydrated potassium ions and is highly selective for potassium over sodium ions [49]. Structures of K_V channels show that commonly the selectivity filter has four K^+ binding sites, two of which bind K^+ ions at a given time instant and two of which are in free form, allowing K^+ ions free of hydrate shell to pass through the pore by sequential binding [34, 36, 37, 47, 50]. The S6 TM α-helix from each α-subunit of tetrameric channel comes together on the intracellular region of the cell membrane and forms the internal activation gate (A-gate) (Fig. 2D). When the cell is at rest this gate is closed, however, upon membrane depolarization the S4 of each VSD moves towards the extracellular space while undergoing a conformational change. This structural rearrangement is presumably transferred through the S4-S5 linker region (shown in Fig. 2D) to the S6, whose displacement opens the A-gate and allows K^+ ions efflux [51-54]. The opening of the channel is the result of a cooperative interaction among the four α-subunits [55]. The functional properties of the channels are mainly determined by the selectivity filter and the VSD, however, additional subunits can also influence the gating, expression, or sensitivity of the channel to certain molecules.

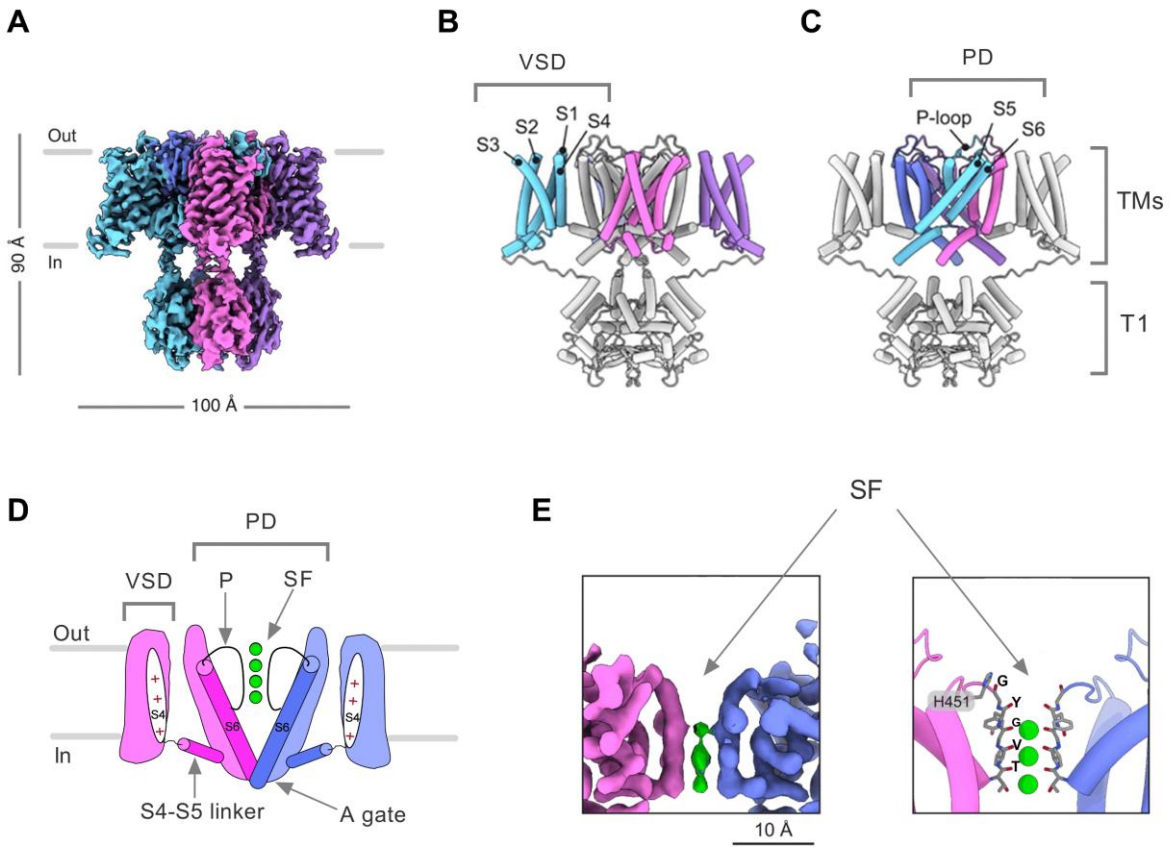

Figure 2: **Structure of human Kv1.3**. (**A**) Cryo-EM density map of human K_V1.3 channel. (**B-C**) Structural model of human K_V1.3. The transmembrane helices (TMs) and T1 domains are indicated. Voltage sensing domains (VSDs, S1-S4) are shown in color in panel B and pore domain (PD,S5-P-S6) are highlighted with color in panel C. (**C**) The front and rear VSDs are omitted for clear side view of PD. (**D**) The cartoon illustrates the side view of differnet parts of VSD and PD. P is the pore loop, SF is the selectivity filter and K^+ ions are highlighted in green. The representation shows two opposing subunits of the four, the other two are omitted for clarity and visibility. (**E**) The close up view of selectivity filter of K_V1.3 shown as density map (left) and structural model (right). The panel highlights the presence of three K^+ ion densities (left) and equivalent ion occupancy (right) in green. The signature sequence (TVGYG) of selectivity filter is indicated with letters. Adopted and modified from Selvakumar *et al*. 2022 [38].

When the K_V1 channels experience prolonged depolarization, it results in a conformational change in the channel causing the channel to enter a functionally non-conducting, inactive state. Inactivation can be induced by two different mechanisms, depending on the type of channel, N- or fast type (in a few ms) or C- or slow type (in a few 100 ms or even s). N-type inactivation is best illustrated practically by the "ball-and-chain" model [56, 57]. For example, in K_V1.4, the high positively charged N-terminal region of the channel, forming the

”inactivation ball”, physically occludes pore from cytoplasmic space and blocks the passage of ions [58]. Some K_V1 channels like $K_V1.3$ lack this inactivation ball but undergo C-type inactivation, a process which is considered to involve conformational changes in selectivity filter that interrupts the ion coordination thereby diminishing K^+ ion permeation [38, 46, 57, 59-63]. Recent studies of Shaker channel and $K_V1.2$–2.1 chimera structures explained that two hydrogen bonds in the pore region between Asp and Trp or between Tyr and Thr/Ser are disrupted during the C-type inactivation [46, 64]. Moreover, these structural studies show that the external part of the selectivity filter dilates causing the partial loss of ion coordination thereby inhibiting ion flux. Molecular dynamics simulation also favors this notion that conformational changes in the selectivity filter impair ion permeation [46].

Among the 8 members of the K_V1 channel family, the selectivity filter and pore regions have many similarities. As mentioned earlier the TXGYGD signature sequence in the selectivity filter region is highly conserved, however subtle differences may exist among the topology of extracellular vestibules of $K_V1.3$ and related channels [37, 39, 40, 45, 65] as shown in Fig. 3A. Among these the so called “turret region” that forms the extracellular vestibule of the channel, is a part of the extracellular loop connecting the S5 to the pore region differs among K_V1 channels, (Fig. 3A). This turret region along with the tip of the S6 and the loop connecting the pore helix to S6 forms the receptor site (Fig. 3B) for animal toxins that plug the pore by docking into the extracellular vestibule of the channels [38, 65, 66]. Although the pore helices (α helical part of the P-loop), the S5 and S6 TM α-helices and selectivity filter of $K_V1.3$ superimposed well onto those of $K_V1.2$ as illustrated in Fig. 3B, there are considerable differences between $K_V1.2$ and $K_V1.3$ in the conformation of the channel regions forming the extracellular vestibule, as highlighted by the box in Fig. 3B [38, 39]. This structural difference among the K_V1 channel types is of great pharmacological importance as it may contribute to the different sensitivity for animal toxins. For example, $K_V1.2$ ion channel is less sensitive to kaliotoxin (KTX, a scorpion derived peptide toxin), which inhibits the $K_V1.3$ ion channel in picomolar concentrations (K_d = 100 – 400 pM). Narrowing the $K_V1.3$ vestibule by replacing Gly380 (short version nomenclature) with the corresponding larger residue (Gln) in $K_V1.2$ channel reduces the sensitivity of $K_V1.3$ to KTX by nearly three orders of magnitude (K_d >1000 nM) [65].

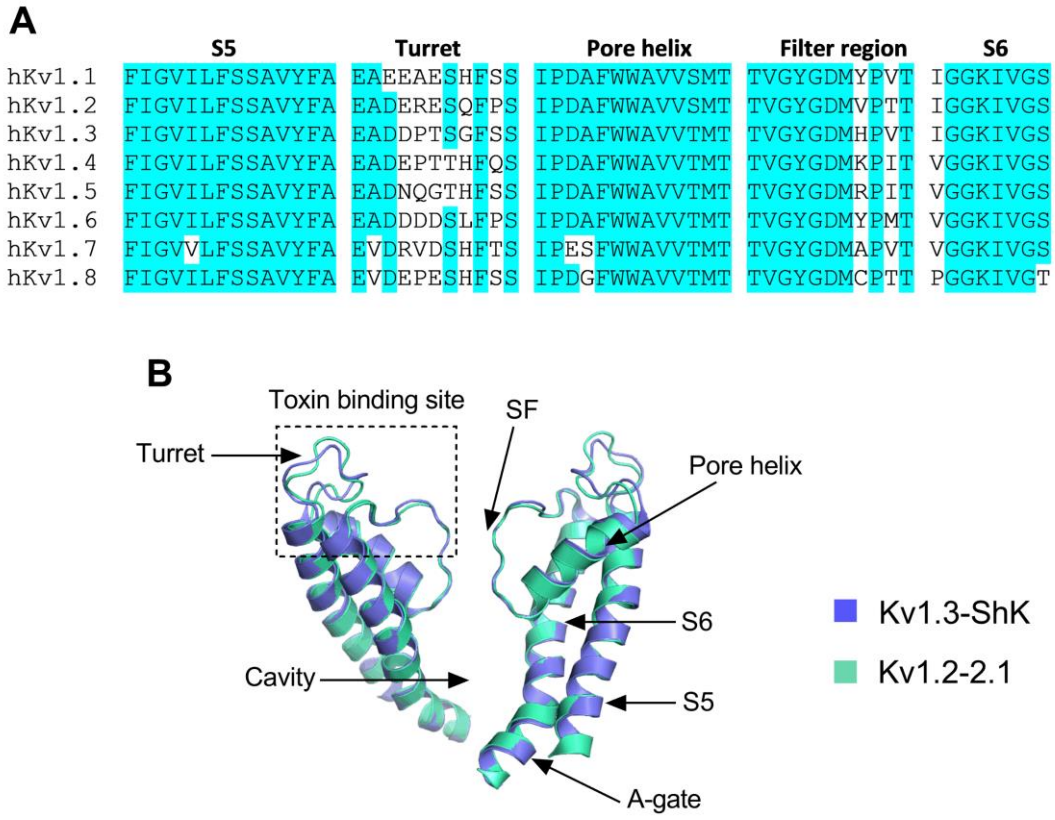

Figure 3: **Comparison of pore conformation of K_V1 channels.** (**A**) Amino acid sequence alignment of the K_V1.1 to K_V1.8 channels. Cyan color shaded letters show identical residues. Different regions of the pore are indicated above the alignment. (**B**) Structural alignments of pore regions of K_V1.2-2.1 [37] and K_V1.3-ShK structures [38]. Arrows indicate different parts of pore region.

2.2.1 Biophysical parameters of K_V1.3

Determination of the voltage- and time dependence that are characteristic of transitions between different structural states of ion channel make it possible to characterize the individual K_V channels, which can also be used to identify the origin of unknown ionic currents (collectively, these parameters are referred as channel gating or simply as biophysical parameters). The biophysical parameters of K_V1.3 gating in T lymphocytes were characterized though single-cell electrophysiology (patch-clamp) technique in both whole-cell [42, 67] and cell-attached patch configurations [68] as shown in Fig. 4. According to these studies, the activation threshold of K_V1.3 channel is around −60 mV, and the open probability increases steeply with increasing depolarization up to 0-10 mV, above this voltage it saturates. The activation time constant of the current when the membrane is depolarized from −120 mV to

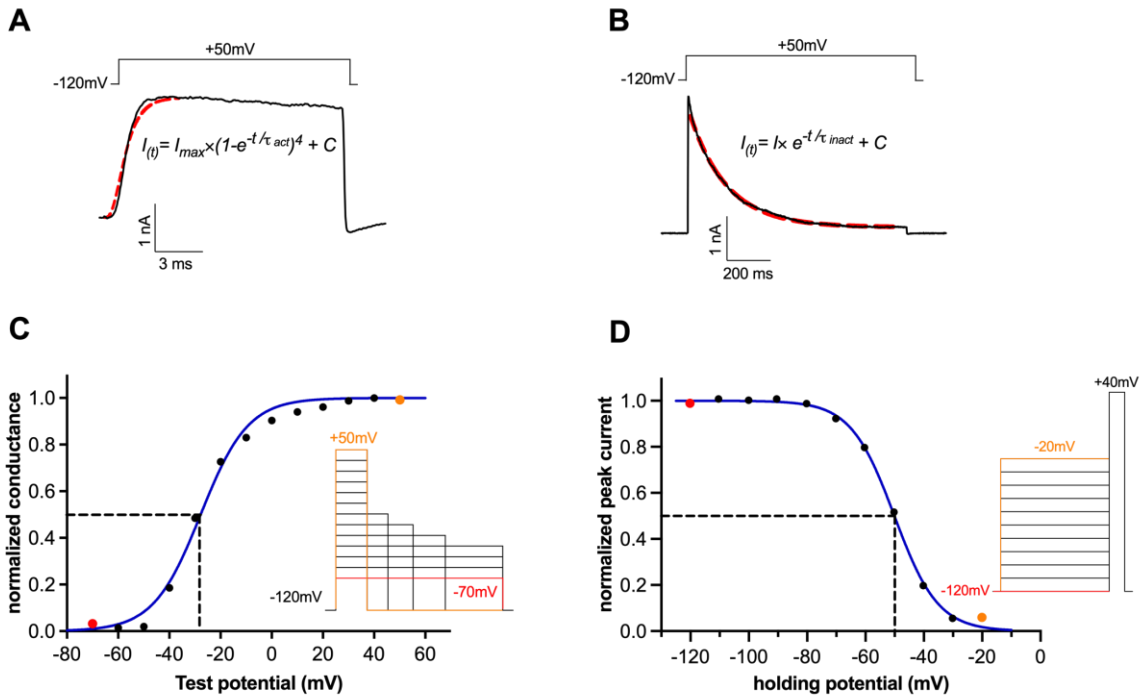

Figure 4: **Biophysical properties of Kv1.3channel. (A, B)** Original $K_V1.3$ currents of activated T cell elicited by voltage steps from -120 mV to +50 for either 15 ms (A) or 1 s (B). **(A)** The activation time constant, that characterizes the activation kinetics of current, is determined by fitting (dashed red line) the current trace using the Hodgkin-Huxley model (inset), where I_{max} is the amplitude of activating current, τ_{act} is activation time constant of the current and C is a constant (offset). **(B)** To characterize the inactivation kinetics of the current, the decaying part of the current is fitted with single exponential decaying function (inset), where I is the inactivating current component, τ_{inact} is inactivation time constant of the decay and C is the non-inactivating (steady state) current. **(C)** The voltage dependence of steady-state activation. The voltage dependence of conductance (G-V) is determined from current-voltage (I-V) relationship which is obtained by measuring peak current at indicated test potentials (voltage protocol in inset, test potentials to –70 mV and +50 mV are highlighted in red and orange, respectively). The cord conductance is calculated for each test potential and normalized conductance is fitted with Boltzmann function (solid blue line) Data points obtained at test potentials to –70 mV and +50 mV are highlighted in red and orange, respectively. Dashed black line indicates the half-activation voltage. **(D)** The voltage dependence of steady-state inactivation. Cells are held at the indicated holding potentials (voltage protocol in inset, holding potential protocols at –120 mV and –20 mV are highlighted in red and orange, respectively) for 2 min and the inactivated fraction of channels is assessed by voltage step to +40mV. The peak currents at different holding potentials (orange: holding potential was –20 mV) are normalized to the peak current evoked from –120mV (indicated in red) and are fitted with Boltzmann function. Dashed black line indicates the half-inactivation voltage. Data are taken from Tajti *et al.* (2021) and Papp *et al.* (2009) [70, 71]

+50 mV is ~0.6 ms (Fig. 4A). The conductance of a single channel is in the order of 10-12 pS. The characteristic parameter for the voltage-dependence of steady-state activation, half-activation voltage or $V_{1/2}$, falls between −30 and −40 mV and its slope is ~10 mV (Fig. 4C). On the other hand, the voltage-dependence of steady-state inactivation has a midpoint of −60 to −70 mV and a slope of ~ −10 mV (Fig. 4D) [69]. The inactivation time constant for depolarization to +50 mV is around 200 ms, and the time required for recovery from inactivation is ~30 –50 seconds (Fig. 4B) [43].

2.3 Role of K^+ channels in T lymphocyte function

2.3.1 Brief overview of the immune system

The primary function of our immune system is to protect the body against harmful foreign pathogens and sterile inflammation. Our immunity can be either innate (natural, native) or adaptive (specifically acquired). In addition to B and T lymphocytes, antibodies, and cytokines produced by these cells are involved in the development of the adaptive immune system. The most important feature of these immune cells is that they carry receptors that specifically recognize antigens. T cells recognize the antigens presented by the MHC (Major Histocompatibility Complex) proteins of the antigen presenting cell (APC-Antigen Presenting Cell) [72]. Naïve T cells ($CCR7^+/CD45RA^+$) circulating in the blood differentiate into lymphoblast after encountering a specific antigen and then develop into effector T cells following rapid clonal proliferation. Following antigen clearance, a significant proportion of effector T cells undergo apoptosis, but a small proportion differentiate into central memory (T_{CM}, $CCR7^+/CD45RA^-$) and effector memory (T_{EM}, $CCR7^-/CD45RA^-$) T cells. These are identified by the absence of CD45RA surface phosphatase and the absence or presence of CCR7 marker, respectively and their function is to rapidly activate the adaptive immune system upon repeated antigenic stimulation [73, 74].

2.3.2 Ca^{2+} signaling in T lymphocytes activation is regulated by $K_V1.3$ and $K_{Ca}3.1$

The first step in T lymphocyte activation is the interaction of specific antigen-loaded MHC molecules with the T cell receptor/CD3 complex (TCR/CD3). This early antigen-reception step involves the rearrangement of cell membrane, forming the immunological synapse (IS) where cholesterol-enriched lipid rafts accumulate and employ the TCR and cytosolic signaling machinery to provide effective transduction and termination of signal. In

the IS tyrosine kinases, for example members of receptor-associated Src-family kinases, recruit the enzyme phospholipase C-γ (PLC-γ) and activate it by phosphorylation, which then hydrolysis its substrate phosphatidylinositol inositol 4, 5-bisphosphate (PIP_2) to diacylglycerol (DAG) and inositol 1,4,5-triphosphate (IP_3). DAG activates the protein kinase C (PKC) enzyme which phosphorylates various cytosolic components of Ras-dependent pathway and contributes to the transcription of cytokines through accumulation of transcription factor AP-1 in the nucleus as illustrated in Fig. 5. The IP_3 molecules diffuse and activate the IP_3 receptors located in the endoplasmic reticulum (ER) membrane, causing the release of ER Ca^{2+} into cytoplasm [75-77]. Consequently, the cytosolic Ca^{2+} concentration increases transiently and Ca^{2+} in ER stores depletes which in turn provokes store operated Ca^{2+} entry (SOCE) through calcium-release activated Ca^{2+} channels (CRAC) [78]. Stromal interaction molecules (STIM)1 and STIM2 located in the ER membrane sense the reduced Ca^{2+} concentration in the store, and dimerize and translocate to the ER-plasma membrane junction, where it binds to four Orai1, the pore-forming subunits to form CRAC channels that allow Ca^{2+} influx from extracellular space (Fig. 5) [79, 80]. The rise in intracellular Ca^{2+} concentration (from 50-100 nM to the micromolar range) stimulates calcineurin, a Ca^{2+} and calmodulin-dependent serine/threonine protein phosphatase, which induces the translocation of the transcription factor NFAT (nuclear factor of activated T cells) to the nucleus after its dephosphorylation [81]. The NFAT initiates the transcription of interleukin 2 (IL-2), early activation markers like CD40L (CD154) and IL-2 receptor (CD25), and other proteins essential for T lymphocyte activation. IL-2 is involved in antigen-independent autoactivation of T lymphocytes and together with other signaling pathways induces T lymphocyte proliferation [19, 76, 82, 83].

Mainly, Ca^{2+} influx during T cell activation occurs via CRAC channels. However, some studies report various other Ca^{2+} channels which contribute to shape the Ca^{2+} signal other than the CRAC channels. Several channels of TRP (transient receptor potential) family such as TRPV6, TRPM2 and TRPM7 are involved in Ca^{2+} signaling in T cells [19, 75, 84]. Two purinergic cation channels P2X4 and P2X7 were shown to be involved in global as well as local Ca^{2+} signal during T cell activation [85].

As a consequence of Ca^{2+} influx through CRAC channels or other channels involved in Ca^{2+} signal following the TCR stimulation, depolarization of membrane reduces electrochemical driving force for sustained Ca^{2+} influx. This effect is significantly counterbalanced by efflux of K^+ ions through two K^+ channels; voltage-gated $K_V1.3$ channel and Ca^{2+}-activated K^+ channel $K_{Ca}3.1$ (IK_{Ca}) [86, 87]. The $K_V1.3$ channels are activated by

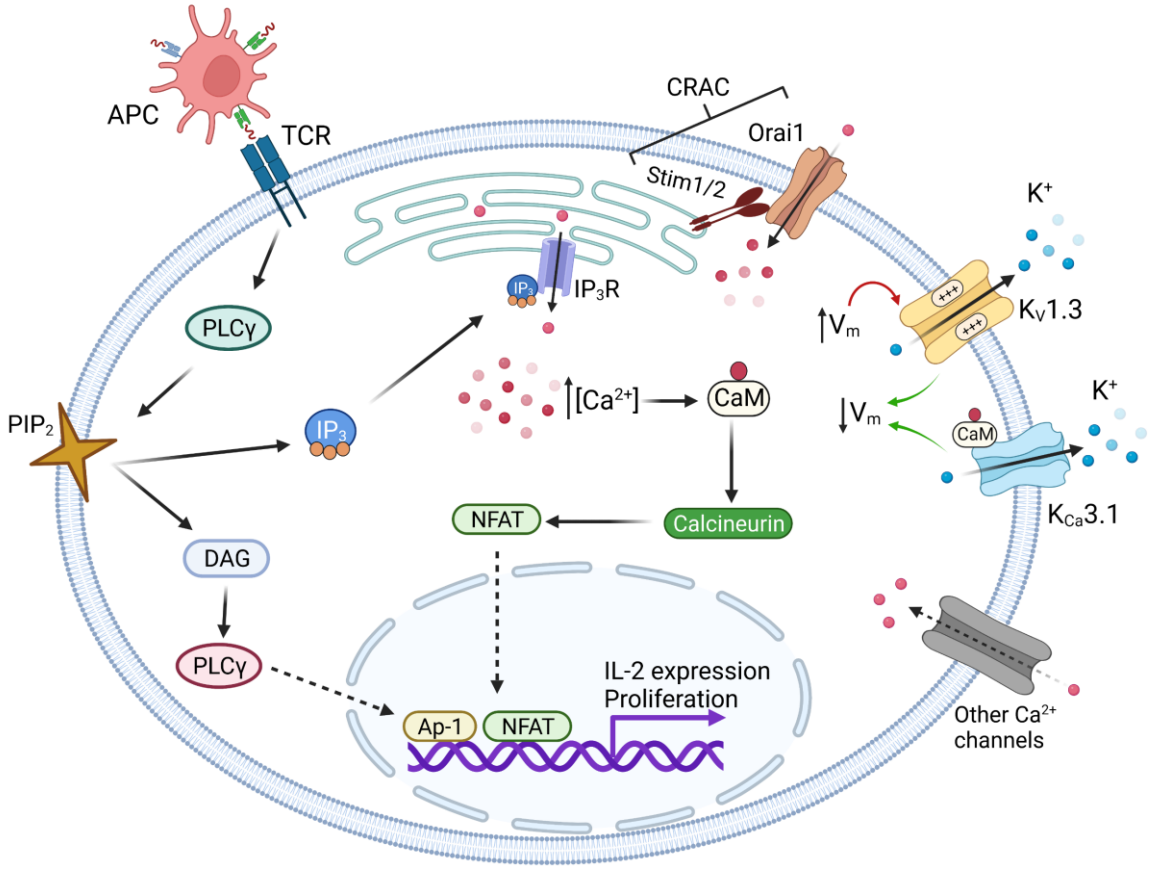

Figure 5: **T cell activation and role of ion channels.** Following, a professional antigen presenting cell (APC) stimulates the T-cell receptor (TCR), cleavage of PIP_2 generates second messengers IP_3 and DAG through the activation of phospholipase C-γ (PLC-γ) signaling cascade. IP_3 activates the IP_3-receptor located in endoplasmic reticulum (ER) causing the release of Ca^{2+} into cytosol. Depletion of Ca^{2+} in ER mobilizes STIM1 and 2 which dimerize and activate the Orai1 subunits of CRAC channel causing Ca^{2+} entry through cell membrane. The other channel types suggested to contribute to Ca^{2+} influx include TRP family voltage-gated Ca^{2+} channels. The upsurge in cytosolic free Ca^{2+} and concomitant membrane depolarization (↑Vm) open the Ca^{2+}-activated $K_{Ca}3.1$ and voltage-gated $K_V1.3$ channels, respectively. The K^+ efflux through $K_V1.3$ and $K_{Ca}3.1$ counterbalances the depolarization effect caused by Ca^{2+} influx and repolarizes the membrane potential (↓Vm) thereby maintaining the driving force for further Ca^{2+} entry. The stabilized Ca^{2+} signal regulates gene expression (*e.g.*, IL-2 expression) leading to cell proliferation and effector functions through a series of signaling molecules.

membrane depolarization induced by Ca^{2+} influx, whereas the elevated intracellular Ca^{2+} mediates the opening of $K_{Ca}3.1$ channels by binding to the calmodulin located in the C-terminal region of the channel (Fig. 5). Following activation of K^+ channels, an outward K^+ flow

reinstates and sustains hyperpolarized membrane potential, thereby maintaining the driving force required for Ca^{2+} entry. This crucial role of K^+ channels in persistent Ca^{2+} signaling, makes the T lymphocyte activation sensitive to K^+ channel inhibitors. Therefore, pharmacological manipulation of T cell function through drugs targeting these K^+ channels bear a great potential in manipulating immune responses [76, 88].

2.3.3 Differential expression of K^+ channel phenotypes in T lymphocyte subsets

The expression pattern of $K_V1.3$ and $K_{Ca}3.1$ channels in T lymphocytes depends on the T cell subset, activation, and differentiation status (Fig. 6). In the resting state, 200-300 $K_V1.3$ and 5-35 $K_{Ca}3.1$ ion channels are present on the cell surface of human naïve T, T_{CM} and T_{EM} cells [76]. However, antigen induced stimulation of T cells leads to differential expression pattern of these K^+ channels in T cell subsets. $CCR7^+$ effector T cells and T_{CM} cells up-regulate the $K_{Ca}3.1$ channel to 500 channels per cell with little or no change in $K_V1.3$ expression [89]. In contrast, following several rounds of antigen-stimulation chronically activated $CCR7^-$ T_{EM} cell drastically up-regulate the $K_V1.3$ expression to 1500 channels per cell (~5-fold increase compared to resting state) with largely unchanged number of $K_{Ca}3.1$ channels [90, 91].

This differential regulation of K^+ channel expression has been identified in both CD4 and CD8 T lymphocytes and an inverse relationship is suggested between expression of CCR7 and $K_V1.3$ channel in T cell subpopulations [92]. The T cell subtype-dependent expression of the Kv1.3 or $K_{Ca}3.1$ ion channels confers differential sensitivity of the proliferation of these T cell subsets to selective K^+ channel inhibitors. Specific blockers of $K_{Ca}3.1$ target the function of $CCR7^+$ naïve and T_{CM} cells however, $K_V1.3$-selective blockers preferentially suppress the proliferation of $CCR7^-$ T_{EM} cells. Since the subtype specific blockade of K^+ channels offer differential suppression of T cell subtype functions, the potent and selective blockers of $K_V1.3$ possess a great therapeutical potential to suppress the chronically overactive T_{EM} cells to autoantigens in autoimmune diseases [74, 90, 93-96].

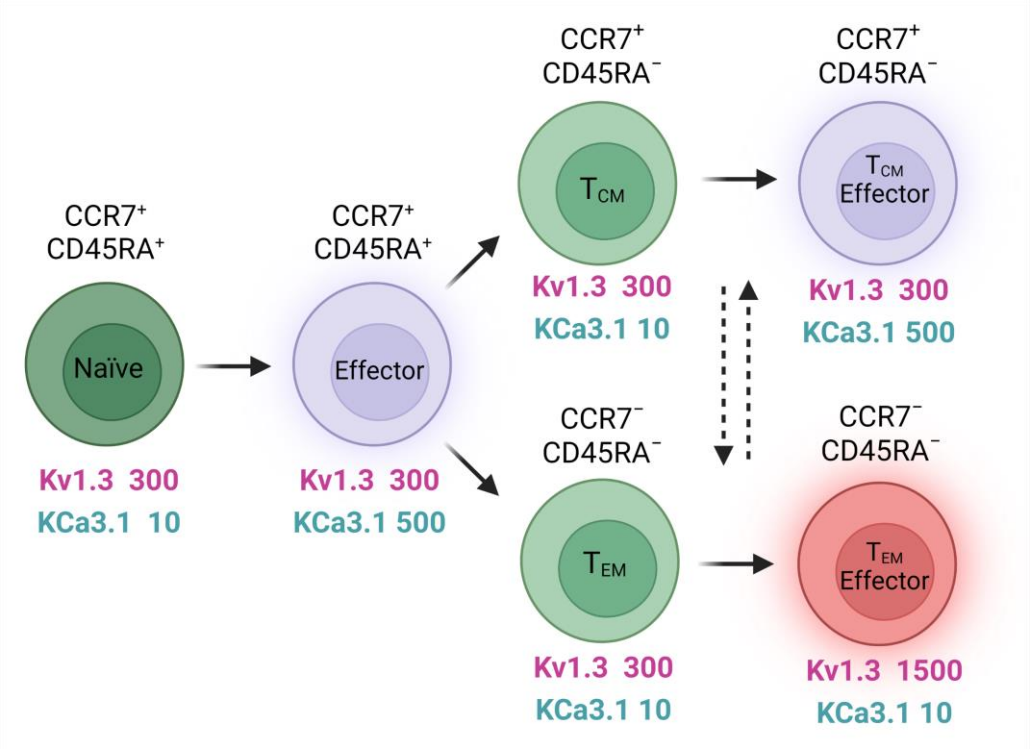

Figure 6: **Expression of K^+ channels in CCR7/CD45RA-distinguished T cell subsets during the quiescent and the activated state.** The average number of $K_V1.3$ and $K_{Ca}3.1$ channels per T cell are shown. Quiescent naïve, central memory T_{CM} and effector memory T_{EM} cells showed a similar expression pattern of $K_V1.3$ (300 channels/cell) and $K_{Ca}3.1$ (10-20 channels/cell). Upon activation, $CCR7^+$ naïve effector and T_{CM} effector cells exhibited upregulation of $K_{Ca}3.1$ channels, however, $CCR7^-$ T_{EM} cells upregulated the $K_V1.3$ channels. Adopted from Cahalan *et al.* [76].

2.4 $K_V1.3$ as therapeutic target in autoimmunity

There are more than 80 different types of autoimmune diseases have been identified and together these affect about 5-8% of global population [97]. The common principles of medication used to halt disease progression are relieving symptoms and non-specifically suppressing the immune responses thereby enhancing the chance of other pathological conditions with long-term side effects [98]. Therefore, an innovative and safer strategy to inhibit the autoantigen-specific immune responses without affecting the protective immune functions is needed for the treatment of autoimmune diseases. The upregulation of $K_V1.3$ channel in autoreactive T cells has emerged as an exciting therapeutic target to remit the autoimmune diseases. Consistent with these, the selective inhibition of $K_V1.3$ channels impairs terminally activated T cell responses in autoimmunity leaving the protective immune responses of naïve and T_{CM} cells unharmed [93, 94, 96, 99].

For several autoimmune diseases, the overexpression of $K_V1.3$ in autoreactive T_{EM} cells has been confirmed such as multiple sclerosis (MS) [90, 100], rheumatoid arthritis (RA), type 1 diabetes mellitus (T1DM) [101], psoriasis/psoriatic arthritis [102], alopecia areata [103] and glomerulonephritis [104]. In a study, the post-mortem brain slices from MS patients showed the high-level $K_V1.3$ expression in T_{EM} cells [105]. Beeton *et al.* showed that T cells in the synovial fluid from affected joints of RA patients were predominantly $CCR7^-$ with high $K_V1.3$ expression, in contrast synovial fluid from non-RA (osteoarthritis) patients mainly contained naïve and T_{CM} cells ($CCR7^+$) with low $K_V1.3$ expression [101]. In the same study, MHC-tetramer-sorted autoantigen-specific peripheral T lymphocytes (specific to GAD65 and insulin) from T1DM patient's blood were $CCR7^-$ with substantially elevated expression of $K_V1.3$. A patient suffering from both MS and T1DM had the high $K_V1.3$ expression in T cells specific for both GAD65 and MBP (myelin basic protein) [93, 101].

Several *in vivo* or *in vitro* studies have demonstrated the applicability of $K_V1.3$ blocker to treat the experimental autoimmune disease models [74, 94]. The animal experiments have been done rat models instead of mice as the expression pattern of K^+ channel in T cells of mice differs from human [106]. Treatment with selective $K_V1.3$ blocker alone or in combination with $K_{Ca}3.1$ significantly improve the disease symptoms of experimental autoimmune encephalomyelitis (EAE), a rat model of MS [100]. Rat models with pristane-induced MHC class II-restricted chronic arthritis showed considerably fewer affected joints during the treatment with $K_V1.3$ blocker (ShK-L5 peptide toxin variant). Similarly, the onset of experimental autoimmune diabetes in rat model of T1DM treated with specific inhibitor of $K_V1.3$ (PAP-1) was 50% less than that of untreated group [101]. Gocke *et al.* showed that $K_V1.3$ knockout mice did not develop the symptoms of EAE [107]. Live cell imaging showed that specific blockade of $K_V1.3$ in T_{EM} cells prevented them from engaging with APC and thus, inhibited T cell stimulation. [108]. All these studies suggest the $K_V1.3$ blockers as a potential drug for the management of autoimmune diseases [93, 101, 109].

2.5 $K_V1.3$ in neuroinflammatory disorders

In the central nervous system (CNS), $K_V1.3$ channels play a role in activation and proliferation of glial cells (microglia, astrocytes, and oligodendrocytes) upon pathological physiological signals. In response to demyelination or general injury, oligodendrocyte precursor cells (OPCs) maturate and can regenerate the neuronal myelin membranes [110]. In proliferating OPCs the upregulation of $K_V1.3$ and other K_V1 channels has been identified [111].

Interestingly, selective blockade of $K_V1.3$ channels halts the S-phase entry thereby inhibiting the OPCs proliferation. Many other studies suggest a good correlation between upregulation of $K_V1.3$ channels and OPC proliferation [18].

Microglia are brain-resident macrophages which play an important role in the innate immune system of CNS. Upregulation of $K_V1.3$ and $K_V1.5$ channels in microglial activation is a hallmark [112]. In quiescent microglial cells the expression of $K_V1.5$ predominates which is required for elevated nitric oxide production but results in cell cycle arrest. In contrast, increase in $K_V1.3$ expression leads to microglial proliferation, migration and proinflammatory cytokines release [113, 114]. Moreover, heterotetramers of $K_V1.3/K_V1.5$ have been identified upon activation of microglial cells with lipopolysaccharide (LPS). Simultaneous upregulation of both K_V1 channels by LPS provokes cytokine production but suppresses the proliferation [115]. $K_V1.5$ channel is crucial for resting cells and $K_V1.3$ expression is needed in case of proliferating microglia. Thus, specific inhibition of $K_V1.3$ holds a great potential to suppress the hyperactive microglia rendering the resting microglial functions untouched in various neuroinflammatory disorders [18, 96] such as Alzheimer's disease (AD) [116], Parkinson's disease (PD) [117], ischemic stroke [118], epilepsy and HIV-1 associated neurotoxicity [119]. For example, in a recent study, inhibition of $K_V1.3$ with PAP-1 reduced inflammation in *in vitro* primary microglial model and ameliorated disease symptoms in mouse PD models [117].

2.6 $K_V1.3$ in other disorders

Other than the above discussed autoimmune disease, there are many other chronic inflammatory diseases in which overexpression of $K_V1.3$ in T_{EM} cells has been observed such as asthma [120], inflammatory bowel diseases (Crohn's disease and ulcerative colitis) [96], allergic contact dermatitis [121], atherosclerosis [122], and chronic kidney disease [123]. In chronic inflammatory diseases, the $K_V1.3$ function is not only mediated by T cells but also other immune cells *e.g.*, B lymphocytes, macrophages, and dendritic cell (DC) are involved [74, 124]. In macrophages, which act as APCs, the leading K^+ currents belong to $K_V1.3/K_V1.5$ heterotetramers and upon stimulation, they upregulate the $K_V1.3$ channels and migrate to the inflammation sites [23]. Macrophages also play a critical role in pathogenesis of atherosclerosis [125].

The involvement of $K_V1.3$ in pathways regulating energy homeostasis and body weight proposes that $K_V1.3$ blockers may be useful for the treatment of obesity, however the function of $K_V1.3$ in adipocytes is not fully explored yet. In an animal study, mice were fed with fat and

fructose enriched diet and treatment with ShK-186 (a variant of a peptide toxin) every other day neutralized the effects of higher caloric diet [74, 126]. Investigations also report that the blockade of $K_V1.1$ and $K_V1.3$ channels with kaliotoxin in rat models improves the cognitive functions *e.g.*, learning [74, 127]. This highlights the potential of $K_V1.3$ in management of memory disorders.

Abnormal/ectopic expression pattern of $K_V1.3$ has been reported across several cancer cell types and stages. Among these, elevated expression of $K_V1.3$ in breast adenocarcinoma, chronic B lymphocytic leukemia, alveolar rhabdomyosarcoma, and certain prostate cancers [128, 129] was reported. $K_V1.3$ inhibition exhibited useful effects *in vitro* by reducing the proliferation and metastasis formation [130]. Thus, $K_V1.3$ may be a novel marker for metastatic phenotype and potential anticancer drug target, specifically for cancers with $K_V1.3$ overexpression [74, 82]. Kv1.3 channels are also present in the inner membrane of mitochondria and have been reported as a therapeutic target for specific cancer types. Membrane permeable small molecule which inhibits mitochondrial $K_V1.3$ are being investigated [131-133].

2.7 $K_V1.3$ channel inhibitors

The vital role of K^+ channels in physiological and pathophysiological functions, and cell- and tissue-specific distribution have made these channels potential pharmacological targets [3]. As discussed in previous sections, several *in vitro* and animal model experiments have established that the inhibition of upregulated $K_V1.3$ channel in autoreactive T_{EM} cells or in activated microglia holds a great potential in the management of autoimmune diseases and many neuroinflammatory disorders. During the last three decades, in parallel to the discovery of cell-specific $K_V1.3$ expression mentioned above, many efforts were made to explore and improve the pharmacological properties of $K_V1.3$ blockers resulting in potent and specific $K_V1.3$ inhibitors [94, 99]. It was initially suggested that the expression of $K_V1.3$ is limited to immune and CNS systems, but later studies described much more widespread distribution of $K_V1.3$ channels and localization of the channel in mitochondrial membrane as well [93, 96]. In addition, studies have also identified the heterotetramer formation of $K_V1.x$ subunits. For example, $K_V1.3/K_V1.5$ heterotetramers are present in macrophages [23] and microglia [115]. On one side, where these diverse structural characteristics of K_V1 channels and their expression pattern cause great challenges in drug discovery, however, on the other side, this diversity is also promising in designing a highly selective and potent blocker of specific type of homo- or heterotetramer channels [93, 99].

There are two large groups of molecules that block $K_V1.3$ channel with high affinity and specificity. Small organic molecules and venom-derived peptide toxins. Small organic molecules typically have less than 800 Da molecular weight, are hydrophobic and membrane permeable. Generally, these small molecules bind to the central cavity located under the selectivity filter of $K_V1.3$ channel (Fig. 3). Due to their small size, these organic molecules make less interaction points with the channel's central cavity, which has high structural similarity among the subtypes of K_V1 channels. This usually causes the low affinity and poor selectivity of $K_V1.3$ blocking small molecules [93, 134]. However, through structure-based drug designing and extensive screening many small molecules (*e.g.*, Psora-4 and PAP-1) have been discovered that inhibit $K_V1.3$ channel with nanomolar affinity but selectivity improvement is still a challenge to make them a drug candidate [135]. PAP-1 is the most potent small-molecule inhibitor of $K_V1.3$ reported to date with IC_{50} of 2 nM and at least 23-fold selectivity over other members of K_V1 family [136]. In contrast, peptide toxins isolated from animal venoms typically have a molecular weight of 3-4 kDa and interact with extracellular pore region of channel with a fairly large interacting surface [137]. The extracellular pore region of $K_V1.3$ has significant structural differences among other K_V channels [38, 65] (Fig. 3). These factors obviously contribute to the high potency (ranging from pico- to nanomolar) and selectivity (more than 1000-fold over other K^+ channels) of the $K_V1.3$ inhibiting peptide toxins. Therefore, from a pharmacological aspect, peptide toxins have advantages over small organic molecules because much smaller concentrations of peptide toxins may be enough for the therapeutic effects. Moreover, the high selectivity of the peptide toxins reduces the possibility of non-specific interactions with other ion channels thereby minimizing side effects [93, 133]. The details about the venom-derived peptides and the mechanisms of K_V1 channel block are discussed in the next section.

2.7.1 Venom-derived K^+ channel blocking peptide toxins

Animal venom (from scorpions, spiders, snakes, sea anemones or cone snails) contain a wide range of peptide toxins that can modulate the ion channel activity. The first peptide toxin ever described in literature was Apamin, isolated from a bee venom, which showed inhibitory effect on small conductance Ca^{2+}-activated K^+ channels (SK, $K_{Ca}2$) [138, 139]. In 1982, the first voltage-gated K^+ channel blocker, noxiustoxin (NTx), was isolated from the venom of scorpion *Centruroides noxius* which blocked $K_V1.2$ (IC_{50} = 2 nM) and $K_V1.3$ (IC_{50} = 1 nM) channels [140]. Subsequently, charybdotoxin (ChTx), a well-studied toxin from scorpion was discovered which blocks various channels like $K_V1.2$, $K_V1.3$, $K_V1.6$ and KCa1.1 in low-

nanomolar affinities [66, 141]. Similarly, margatoxin (MgTx) was initially identified as a potent and selective inhibitor of $K_V1.3$ (K_d = 50−100 pM) from *Centruroides margaritatus* [142] but later on found that it also blocks $K_V1.1$ and $K_V1.2$ with similar affinity. The structural attributes of MgTx are illustrated in Fig. 7A [143]. A sea anemone peptide ShK was isolated from *Stichodactyla helianthus* which blocks $K_V1.3$ (IC_{50} = 11 pM) and some other $K_V1.x$ channel subtypes with picomolar affinity as well [144, 145]. These K^+ channel inhibitor peptide toxins have been remarkably useful not only in characterizing the physiological role of K^+ channels but also helped to better understand the structural features of channel proteins, composition of subunits and mechanisms underlying the channel gating [65, 75, 146, 147].

In the last three decades, several peptide toxins targeting K^+ channels have been described. Currently, the Kalium database, a collection of natural peptides affecting K^+ channels enlists 350 entries [148]. These peptide toxins have different structural features and are blocking various K^+ channels with varying affinities ranging from pM to µM concentration. Based on the structural and functional characteristics, potassium channel inhibitor toxins (KTxs) derived from scorpion are classified into 7 different families: α-KTx, β-KTx, γ-KTx, δ-KTx, ε-KTx, κ-KTx, and λ-KTx [148-150].

The α-KTx family contains peptides with 23–42 amino acid residues and shares a common structural motif known as the cysteine-stabilized α/β scaffold, in which the α-helix and β-sheets are held together by 3–4 disulfide bridges (Fig. 7). Based on the sequence similarity among α-KTx family members, 31 subfamilies of α-KTx have been described previously (https://kaliumdb.org). A common feature of K^+ channel blocking peptides isolated from various animal venoms is the presence of a typical "functional dyad" which consists of a critically positioned Lys residue and an aromatic residue (usually Tyr) nine positions downstream in the sequence. This separates the C_α of the Lys from the center of the benzene ring of the Tyr by ~6.6 Å in three-dimensional (3D) structure [75, 137, 151]. The structural models of a few α-KTxs are illustrated in Fig. 7A-C with highlighted positions of functional dyad residues. These K^+ toxins employ "cork in the bottle" blocking model, the side chain of the critical Lys protrudes into the selectivity filter of the channel and plugs the pore, thereby preventing the K^+ ion efflux [38, 66] as demonstrated by computational model of interaction between Vm24 (α-KTx 23.1), a peptide toxin isolated from *Vaejovis mexicanus smithi*, and $K_V1.3$ channel in Fig. 8 [152]. This central Lys is considered important for the high affinity toxin binding. The aromatic residue of the functional dyad interacts with the external vestibule region including the turret and pore-S6 linker domains of the channel which has more

significant differences in the amino acid sequences among subtypes of K_V1.x family as described in earlier sections and shown in Fig. 3. This interaction of an aromatic residue with external vestibule of K_V1 channels is considered responsible for selectivity among K_V1.x channel subtypes [66, 75, 99, 153, 154].

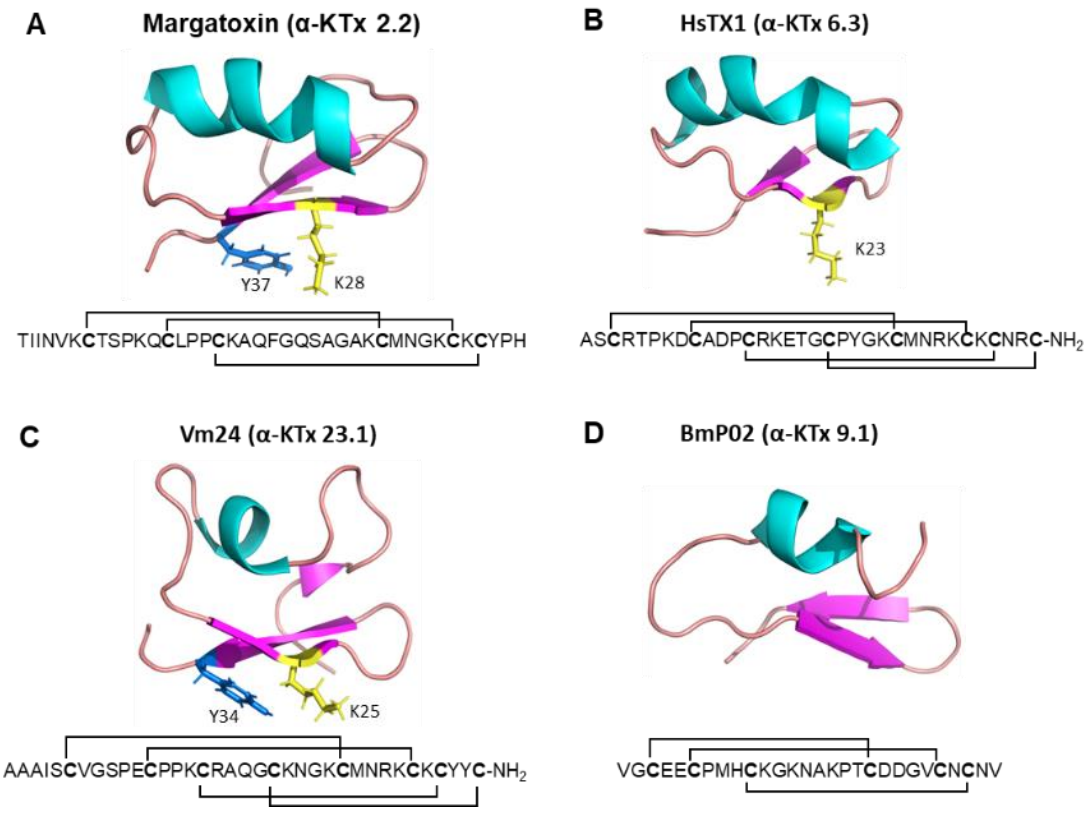

Figure 7: **The structural models of representative of α-KTxs.** The amino acids sequences (disulfide bonds are indicated with connecting lines) and 3D structures of **(A)** margatoxin (PDB: 1MTX), **(B)** HsTX1 (PDB: 1QUZ), **(C)** Vm24 (PDB: 2K9O), **(D)** BmP02 (PDB: 1DU9). Residues of typical functional dyad are shown by sticks (Lys: in yellow and Tyr: in blue). HsTX1 bears only Lys residue of function dyad (B) and BmP02 lacks the functional dyad (D).

Some α-KTxs bear only the critically positioned Lys residue of functional dyad but lack the aromatic residue. For example, a potent inhibitor peptide isolated from *Heterometrus spinnifer*, HsTX1 (α-KTx 6.3) has only Lys of typical dyad at position 23 as shown in Fig. 7B [155]. More interestingly, scorpion toxins lacking this signature dyad have been identified but are still active on K_V1 channels [156]. For example, BmP02 (α-KTx 9.1), a short peptide toxin from Chinese scorpion *Buthus martensi* Karsch lacks the typical functional dyad (Fig. 7D) however, it still inhibits K_V1.3 with K_d of 7nM [157]. Similarly, Tc32 (α-KTx 18.1) toxin from

Tityus cambridgei does not have this dyad but nevertheless blocks $K_V1.3$ with decent affinity (K_d = 10 nM) [158]. This suggests that for stable toxin–channel interaction, other influential residues of toxins may interact pairwise with the channel residues contributing to their high affinity and selective binding to different $K_V1.x$ channels [65].

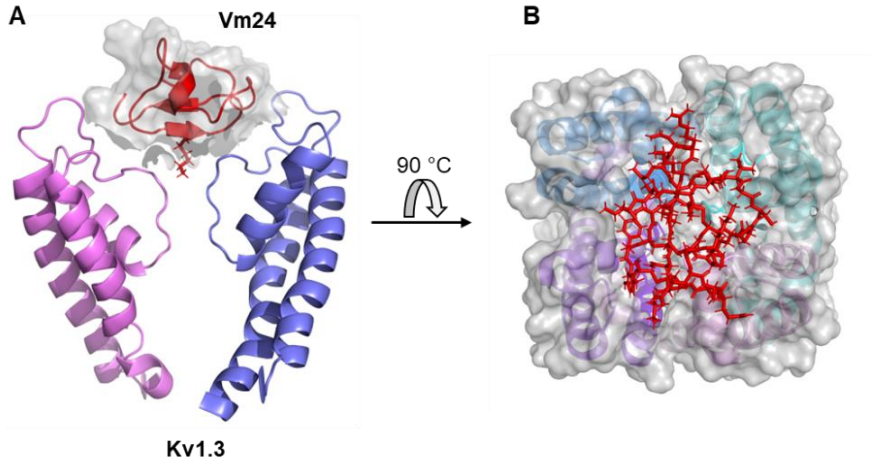

Figure 8: **Docking model of the Vm24 and $K_V1.3$ interaction. (A)** Pore-blocking mode of Vm24 on $K_V1.3$. The channel pore region is shown as side view and front and rear pore domains are omitted for clarity. The surface of the toxin is colored light gray, and the backbone is displayed in red color. **(B)** Top view of channel toxin interaction, where Vm24 is exhibited by red sticks and the molecular surface of the channel pore is colored light gray. Vm24 and $K_V1.3$ docking model is adopted and modified from Gurrola *et al.* (2012) [152].

The other mechanism through which toxins inhibit K^+ channel function is the "gating modifier" effect in which toxins bind to the voltage sensor domains (VSD) and cause a prominent shift in the voltage dependence of steady-state activation towards more depolarized potentials and consequently, reduce the K^+ current [159]. For example, a spider venom peptide Hanatoxin is a gating modifier and inhibits K^+ current by interaction with VSD of $K_V2.1$ channel [160].

2.7.2 Affinity and selectivity improvement of peptide toxins

Most potent peptide toxins affect multiple ion channel subtypes with comparable affinities due to the topological similarity of the outer pore region among K^+ channels. For example, in addition to $K_V1.3$ inhibition with pM affinity, OSK1 blocks Kv1.1 and $K_V1.2$ [161]; ShK inhibits $K_V1.1$, $K_V1.4$ and $K_V1.6$ [144, 145], anuroctoxin (AnTx) blocks $K_V1.2$ [162],

while HsTX1 blocks K_V1.1 [155] with nM affinities. Vm24, described by our group, is the only known natural peptide from scorpion with highest affinity (K_d = 2.9 pM) and selectivity for K_V1.3. It has more than 1500-fold selectivity for K_V1.3 over ten channels tested including K_V1.1, K_V1.2, K_{Ca}3.1 [152, 163]. High affinity toxins are attractive lead peptides for the development into therapeutically usable drugs. Therefore, substantial efforts have been invested to improve the selectivity of natural toxins for K_V1.3 over other channels to minimize the off-target effects. A minimum of 100-fold selectivity for a particular channel type over other channel types is desired for claiming a drug to be specific [75, 164]. Multiple protein engineering strategies such as mutation of amino acid residues that are determinants of strong binding with the channel, chemical modification, residue truncation/elongation and binding interface modulation have been employed to tailor the selectivity of toxins towards the desired direction [99, 164]. The amino acid substitution method was first used to enhance the specificity of scorpion toxin OSK1 and the OSK1-E16K /K20D double mutant was tested as a potent inhibitor of K_V1.3 with high affinity (K_d = 3 pM) but without any change in selectivity. However, trimming the three amino acid residues from C-terminus of OSK1-E16K /K20D significantly improved the selectivity for K_V1.3 over K_V1.1 (200-fold) and K_V1.2 (1000-fold), although C-terminus truncation slightly reduced the affinity for K_V1.3 [165]. HsTX1[R14A] mutant retained high affinity for K_V1.3 and showed 2,000-fold selectivity over K_V1.1 [166]. Similarly, by using sequence analysis our group engineered an analog of Anuroctoxin (α-KTx-6.12, AnTx) with double substitution (N17A/F32T) which preserved its natural potency for K_V1.3, while gaining 16,000-fold selectivity over K_V1.1, K_V1.2 and K_{Ca}3.1 [167]. Vm24, which is naturally a highly selective and potent blocker of K_V1.3, was mutated by substituting a single residue (K32E) based on the transcriptome analysis by our group. sVmKTx is still a high affinity blocker of K_V1.3 while gaining the ~9000-fold selectivity over K_V1.2 while K_V1.1 and K_{Ca}3.1 were insensitive to the engineered peptide at 2.5 μM concentration [168]. The best example to demonstrate how the pharmacological properties can be refined through protein engineering is the generation of ShK analogues [94]. To improve the selectivity of ShK for K_V1.3 over other targets, many analogues have been designed by chemical modification and amino acid substitution [169]. ShK-186 with N-terminus phospho-Tyr moiety and C-terminus amidation is potent and selective inhibitor of K_V1.3. ShK-186, now known as Dalazatide, has been approved as a first toxin-based drug to enter clinical trial for autoimmune diseases [170, 171].

The ongoing discovery of K^+ channel blocker peptides suggests that scorpion venoms are remarkably rich sources of attractive peptides. The diverse nature of their primary sequence, robust interaction pattern with their receptors and valuable therapeutic potential encourages the scientists to explore the different scorpion venoms from various geographic regions for novel peptides.

2.7.3 Fluorescent toxins as probes for $K_V1.3$ channel

As described in earlier sections the upregulation of $K_V1.3$ in immune and CNS cells has emerged as an appealing target for autoimmune and neurological diseases and its role is beginning to be understood in non-immune cells during pathological states. Therefore, a selective molecular visualization tool is much needed to investigate the contribution of $K_V1.3$ to pathogenesis, to study the expression of $K_V1.3$ in intact cells from various tissues, for all stages of therapeutic development and as a diagnostic tool.

The venom-derived toxins bind selectively and with extremely high affinities to channel thus, these toxins have been exploited to create fluorescently labeled probes for $K_V1.3$. However, unlike $K_V1.3$ specific antibodies, which bind to the epitopes located on the outer vestibule of single subunit [172], peptide toxins bind to the tetrameric functional channel and can easily recognize folded from unfolded channel or distinguish homotetrameric from heterotetrameric assembly of channel. Previously, $K_V1.3$-targeted probes were developed by chemically conjugating a fluorophore with toxins or recombinantly linking to the fluorescent proteins. For example, fluorescein-6-carboxyl (F6CA) was conjugated to N-terminus of ShK toxin which showed picomolar affinity for $K_V1.3$ with IC_{50}= 48 pM [173]. MgTx, AgTx and OSK1 were conjugated with green fluorescent protein and resulting chimera exhibit nanomolar affinity for $K_V1.3$ [174-176]. So, there is still space to expand the available toolkit for visualization of $K_V1.3$. A fluorescently labeled analogue of highly potent and selective toxin for $K_V1.3$ can be designed as a tool for *in vivo* and *ex vivo* imaging, to track the biodistribution of drug peptides and for diagnostic of chronic inflammatory diseases.

2.8 Recombinant production of peptide toxins

Although several peptide toxins have been identified which potentially act on $K_V1.3$ channel, only a few peptides have been investigated in detail. The major challenge in characterizing the pharmacological and structural properties of peptide toxins and their therapeutic development and application is the constraint of the native toxin material that can

only be extracted from animal venom in extremely limited amounts. Due to the complex structural features and presence of multiple disulfide-bridges the preparation of peptide toxins faces several technical challenges [137]. The chemical synthesis offers an approach to artificially produce disulfide rich peptides and their analogs. However, it is expensive and yields a small quantity of active conformers of peptide toxins [177]. On the other hand, heterologous protein expression system is a cost-effective and most widely used technique to produce large quantities of recombinant proteins. However, recombinant expression of proteins of eukaryotic origin in bacteria needs post translational modifications and *in vitro* refolding for proper activity of peptides [178]. Although some engineered *E. coli* strains are capable of disulfide bond formation and refolding the peptide, their yield is still very low [179, 180]. For example, margatoxin was previously produced in *E. coli* yielding 3−4 mg/L of functional peptide [142, 181]. The yeast expression system can over overcome all these limitations as discussed in detail in the next section. In comparison to yeast expression systems, the production of recombinant proteins in insect cells and animal cell cultures is complicated and more expensive [182].

2.8.1 Yeast expression system

Pichia pastoris is a methylotrophic yeast described by Koichi Ogata for the first time in 1969 [183]. During the 1980s, it was developed as a heterologous expression system and has become widely popular because of its numerous advantages over bacterial system [184]. It offers an economical and better approach for higher yields of correctly folded recombinant peptides. Foreign genes are expressed under the alcohol oxidase 1 (*AOX1*) promoter, tightly induced by methanol (MeOH) which regulates alcohol oxidase expression, an enzyme involved in MeOH metabolism. Around 30% of the total soluble protein in MeOH feed cells consists of alcohol oxidase, which is testimony of the strength of *AOX1* promoter [185]. High biomass production in simple medium, ease of genetic manipulation and capability of performing posttranslational modifications are other advantages of this system. Additionally, the recombinant proteins are secreted directly into the medium with very few endogenous proteins which simplifies the downstream processing [186-188]. For example, Anangi *et al.* expressed and purified the His-tagged margatoxin and agitoxin in *Pichia* expression system with a yield of 12−15 mg/L and 14−18 mg/L, respectively [189]. Our group has also reported a high yield of AnTx and Ts6 peptide toxin in the *P. pastoris* system recently [190].

Pichia pastoris has the tendency to incorporate multiple copies of foreign gene cassettes at a single locus through homologous recombination, facilitating high level heterologous

expressions as depicted in Fig. 9. Moreover, the overexpression of foreign proteins can be enhanced considerably by codon optimization, screening for multiple copy integrant and choice of efficient promoter [188, 191]. For example, codon-optimized glucanase was expressed 10-fold higher than the wild-type gene in *P. pastoris* [192]. Nordén *et al.* reported that hyper-resistance against Zeocin was intimately correlated with enhanced expression of foreign proteins in *P. pastoris* [193]. Similarly, several studies have proved that optimization of the cell fermentation conditions such as biomass production, pH of the medium, induction duration and percentage of MeOH induction for individual protein resulted in an improved expression of heterologous proteins in *Pichia pastoris* system [194].

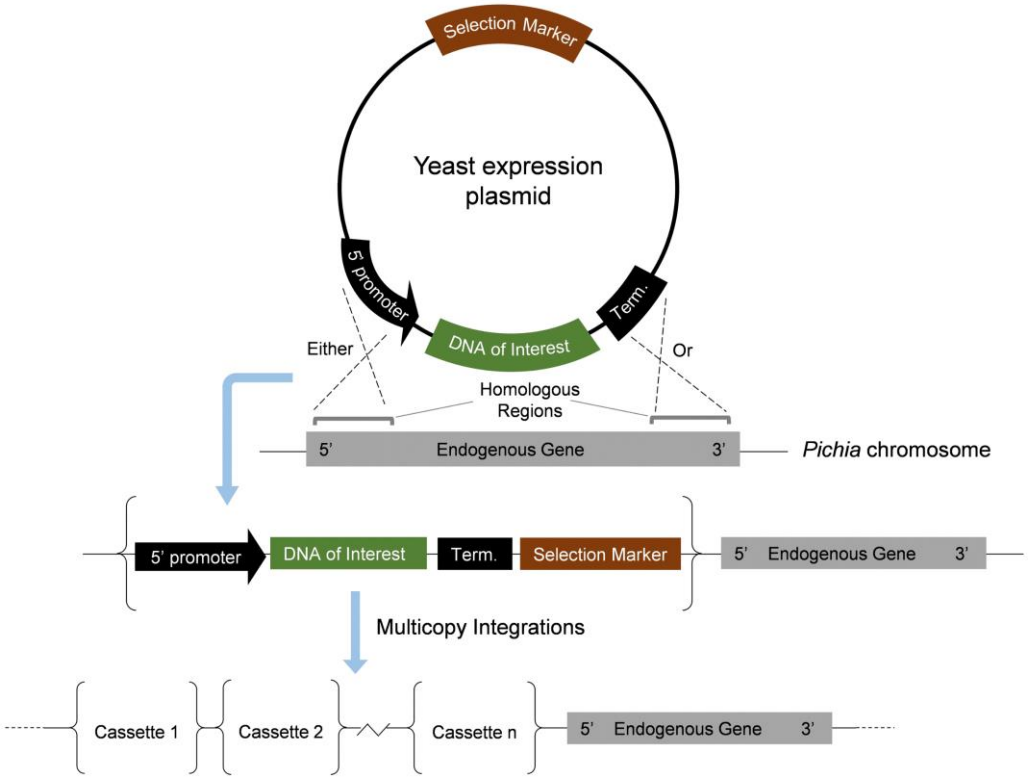

Figure 9: **Illustration of multiple copy integration of expression cassette in *Pichia pastroris* genome.** Linearized yeast expression plasmid containing the gene of interest integrates at alcohol oxidase 1 gene locus in the *Pichia pastoris* genome though homologous recombination either at 5′ *AOX1* promoter or 3′ *AOX1* terminator regions. Multiple copies of plasmid (indicated as cassette n) can be inserted at the same locus.

3. AIMS OF THE STUDY

3.1 Pharmacological and functional characterization of a novel K_V1.3 inhibitor toxin from *C. margaritatus* scorpion

As described in the introduction, scorpion venom is a rich source of K_V channel affecting peptide toxins. In quest for novel K_V1.3 blockers a unique new peptide toxin, named Cm28, was identified from the Colombian scorpion *Centruroides margaritatus* by our collaborators. Our aims were:

1. To characterize the pharmacological properties of Cm28 against a battery of K^+ and Na^+ channels through single-cell electrophysiology
2. To investigate the mechanism of block of K_V1.2 and K_V1.3 channels by Cm28
3. To study the biological effect of Cm28 on human T lymphocyte activation

3.2 Characterization of a fluorescent peptide toxin as a probe for K_V1.3

A fluorescent analogue of a potent scorpion toxin HsTX1[R14A] as a tool to visualize the K_V1.3 expression was developed by conjugating the cyanine dye Cy5 to the chemically synthesized toxin by our collaborators. Our aims were:

1. To analyze the binding affinity of Cy5-HsTX1[R14A] with various K^+ channels including the K_V1.3/K_V1.5 hetrotetrameric channel using single-cell electrophysiology
2. To demonstrate the ability of Cy5-HsTX1[R14A] to detect K_V1.3 expression level in flow cytometry

3.3 Optimization of recombinant production of margatoxin and the functional characterization of the tagged and untagged versions of the peptide

Due to structural complexities, preparation of larger amounts of toxins faces a number of technical challenges. Meanwhile the produced peptides should maintain their biological functions. Our aims were:

1. To improve the yield of recombinant MgTx in the Pichia pastoris (yeast) expression system through optimizing multiple factors at genetic level and the fermentation conditions
2. To test the effect of conjugation of MgTx with the His-tag on the binding to K_V1.2 and K_V1.3 channels
3. To validate the biological activity of rMgTx variants on human T lymphocyte activation

4. MATERIALS AND METHODS

4.1 Reagents and Chemicals

All the chemicals and reagents used in this study were procured from Sigma-Aldrich, St. Louis, MO, USA, and enzymes were purchased mainly from Thermo Fisher Scientific, Waltham, MA, USA unless stated otherwise.

4.2 Toxins

4.2.1 Cm28

The native Cm28 peptide toxin was isolated from the venom of the Colombian scorpion *Centruroides margaritatus* in Prof. Lourival Possani's laboratory (our collaborator from UNAM, Mexico). Scorpions were collected from Patia valley, Cauca, Columbia, and venom was obtained by electrical stimulation. The toxic peptides were isolated by three-step purification as described in detail previously [195]. First, the venom was fractioned by size exclusion chromatography then, the main peak was subjected to ion-exchange chromatography (IEC). Finally, all the IEC fractions were further separated by reverse-phase high performance liquid chromatography (RP-HPLC) using analytical C_{18} column. The amino acid sequencing of Cm28 peptide was performed by automatic Edman degradation using Biotech PPSQ-31A Protein Sequencer equipment (Shimadzu Scientific Instruments, Inc., Colombia, MD, USA).

4.2.2 Cy5-HsTX1[R14A] Fluorescent toxin

HsTX1[R14A] is a modified scorpion toxin originally isolated from the venom of *Heterometrus spinifer*. A fluorescent analogue of this toxin was developed by Prof. Ray Norton's laboratory (our collaborators from University of Monash, Australia). HsTX1[R14A] was prepared using solid phase chemical synthesis and the cyanine dye Cy5 was conjugated at its N-terminus, and spectral properties of Cy5-HsTX1[R14A] were characterized using fluorescence spectroscopy.

4.2.3 Margatoxin

Recombinant margatoxin (rMgTx) in two versions; His-tagged (TrMgTx) and untagged (UrMgTx) was produced using *Pichia pastoris* expression system in this study. A detailed methodology is described in the next section.

4.3 Recombinant margatoxin production protocol

4.3.1 Construction of expression plasmid

The amino acid sequence of margatoxin (MgTx) was retrieved from an online protein (Uniprot P40755) database. The MgTx gene cassette was designed by placing the 6x His-tag at N-terminus to facilitate the purification, and factor Xa protease site was introduced in-between them to obtain native N-terminus MgTx, as demonstrated in Fig. 10. The codon-optimized DNA sequence of this MgTx cassette for *Pichia pastoris* was generated according to the codon usage database available at (www.kazusa.or.jp/codon) and synthesized by IDT technology, Coralville, IA, USA. The codon-optimized MgTx cassette was cloned into yeast expression vector pPICZαA (Invitrogen, Waltham, MA, USA) using *EcoRI* and *XbaI* restriction sites following the standard cloning procedures.

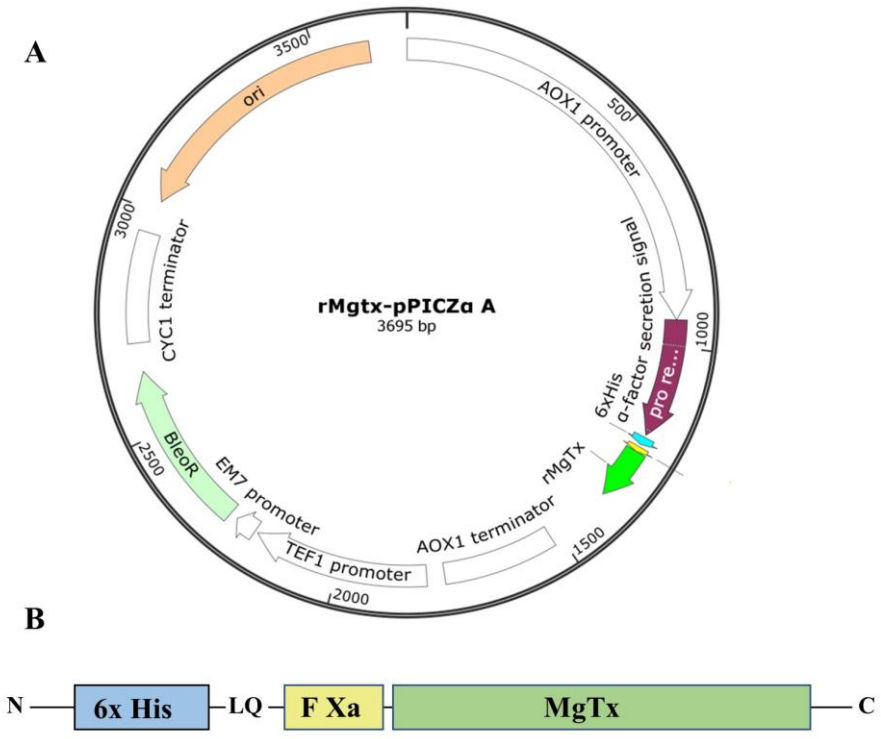

Figure 10: **Structure of the yeast expression vector.** (**A**) Graphical representation of recombinant plasmid TrMgTx-pPICZαA designed using SnapGene® tool (**B**) Schematic demonstration of TrMgTx cassette, **FXa**; factor Xa protease site, **MgTx**; margatoxin.

Competent cells of *Escherichia coli* TOP 10F′ were prepared using ice-cold $CaCl_2$ method, transformed with ligation mixture using heat-shock method following standard protocol [196] and spread on LB agar plates (1% NaCl, 1% tryptone, 0.5% yeast extract and

pH 7.0) containing 30 µl/ml of Zeocin (selection antibiotic). After overnight incubation at 37 °C, first, positive clones for rMgTx-pPICZαA were screened by performing colony PCR then, in-frame ligation and nucleotide sequence of MgTx gene was confirmed by DNA sequencing using plasmid specific primer given in Table 2 and aligning the obtained DNA sequence with theoretical sequence of MgTx.

Table 2: **List of primers for pPICZα A plasmid**

Primer	Sequence	Length
5′ AOX1	GACTGGTTCCAATTGACAAGC	21
3′ AOX1	GCAAATGGCATTCTGACATCC	21

4.3.2 Transformation of *Pichia pastoris* X-33 and selection of hyper-resistant transformants against Zeocin

The expression plasmid rMgTx-pPICZαA was linearized by digesting with *SacI* endonuclease enzyme and transformed into *P. pastoris* X-33 competent cells using Pichia EasyComp Transformation Kit (Invitrogen, Waltham, MA, USA) following the protocol specified by the manufacturer. Transformed X-33 cells were spread on YPD agar plate (2% peptone, 1% yeast extract, 2% agar, 2% dextrose and pH 7.0) supplemented with 100 µg/ml of Zeocin. After 3-day incubation at 28 °C, 24 prominent colonies were re-grown on YPD plates containing progressively increasing Zeocin 0.5, 1 and 2 mg/ml for the selection of clone showing hyper-resistance against Zeocin. To confirm the integration of expression construct into genome of *Pichia* transformants (survived on 2 mg/ml Zeocin) colony PCR analysis was performed using plasmid specific primers (Table 2).

4.3.3 Time-course study of rMgTx expression and optimization of pH of the medium and MeOH induction

Selected clone from the YPD plate containing 2 mg/ml of Zeocin was grown overnight in 5 ml of YPD medium and next day, it was diluted to an OD_{600} = 0.2 in 5 ml of BMGY medium (1% yeast extract, 2% peptone, 100 mM potassium phosphate, pH 6.0, 1.34% YNB, 4×10^{-5} % biotin and 2% glycerol) for biomass production at 30 ℃ with constant shaking (230 rpm) until the optical density at 600 nm (OD_{600}) reached between 15 and 20 (after 24-36 h). Cells were collected by centrifugation, re-suspended in 5 ml of BMMY induction medium (same as BMGY with 0.5% MeOH instead of glycerol) and grown for five days at 28 ℃ with constant shaking (230 rpm). 0.5% (v/v) MeOH induction was maintained by adding absolute

MeOH every 24 h. To find the suitable concentration for MeOH induction, cells were induced with 0.5, 1 and 1.5% (v/v) MeOH and for pH optimization, cells were grown in media of different pH values of pH 5, pH 6, and pH 7 and in unbuffered media. 15 µl of supernatant samples were taken from indicated time points and analyzed on 16% tricine SDS-PAGE. The amount of TrMgTx in the gel image was determined by comparing the band intensities with the standards (TrMgTx with known concentration) using Image Lab tool (Bio-Rad). All the experiments were run in triplicates.

4.3.4 Large scale Fed-batch fermentation and purification of TrMgTx

Large-scale flask-level production was executed following the optimized conditions as described earlier. The clone with the highest expression level of TrMgTx was inoculated in a 2-liter flask containing 250 ml BMGY medium and when OD_{600} reached between 15 and 20, cells were shifted to 250 ml BMMY induction medium and induced with 0.5% (v/v) MeOH for 72 h.

Two-step purification was employed to efficiently isolate secreted TrMgTx from the culture. The supernatant of the cell culture was separated from the *Pichia* cells by centrifugation at 4000 RPM for 20 min. The collected supernatant 2× diluted with buffer (50 mM potassium phosphate, pH 7.4) and 60 mM imidazole was added. The filtered supernatant was loaded on pre-equilibrated His-trap column packed with Ni^{2+} Sepharose™ High Performance (GE Healthcare, Chicago, IL, USA) with binding buffer (50 mM potassium phosphate, 300 mM NaCl, pH 7.4) at a flow rate of 3 ml/min using liquid chromatography system (Shimadzu Scientific Instruments, Inc., Colombia, MD, USA). After washing the column with 3 column volume (CV) wash buffer (binding buffer+ 60 mM imidazole), bound proteins were eluted by running 3 CV of elution buffer (binding buffer+ 500mM imidazole) and additional 3 CV of 1 M imidazole in isocratic mode. Fractions collected from affinity column were directly applied on reversed phase (RP) C_{18} semi-prep column (10 mm × 250 mm, 5 µM bead size, 300 Å pore size, Vydac® 218TP, HiChrom, UK) using Prominence HPLC System at flow rate of 1 ml/min. Then, a linear gradient of 10-30% of solvent B (0.1 % TFA in 95% acetonitrile) in Solvent A (0.1% TFA in deionized distilled water) was run over 30 min. Absorbance was monitored at 230 nm with PDA detector. Peak fractions were collected manually and tested on 16% tricine-SDS PAGE. Purity level was judged by reloading the fraction on analytical C_{18} column and calculated using equation [(area under the peak of interest)/ (cumulated area under all peaks) x 100]. Purified peptide was stored at –20 ℃ for further assays.

4.3.5 Tricine SDS-PAGE and Western blot

16% tricine SDS-PAGE was performed as described hitherto [197]. Protein sample was mixed with tricine sample buffer (Bio-Rad, Hercules, CA, USA) in 1:1, incubated at 95℃ for 5 min and subsequently centrifuged at 10,000 rpm for 30 seconds before loading. Electrophoresis was carried out at constant 120 V for 90 min. For protein visualization, the gel was stained with Coomassie Brilliant Blue (CBB) R-250 for 45 min and de-stained using 40% MeOH and 10% acetic acid mixture for 2-3 h.

For Western blotting, the resolved proteins were electro-transferred in wet conditions onto charged Immobilon-P PVDF membrane (Merck, Rahway, NJ, USA). Non-specific binding of antibody in the subsequent steps was prevented by membrane blocking with 5% (w/v) skim milk in TBST (50 mM Tris-HCl, pH 7.5, 150 mM NaCl, and 0.1% Tween 20) for overnight at 4 ℃. The washed membrane was probed with mouse anti-histidine monoclonal antibodies conjugated with horseradish peroxidase (Bio-Rad, Hercules, CA, USA) in TBST (1:2500) and incubated for 1 h at room temperature. The bands were visualized using Pierce™ enhanced chemiluminescent (ECL) substrate (Thermo Fisher Scientific, Waltham, MA, USA).

4.3.6 Cleavage of His-tag from TrMgTx

Hexahistidine residues fused at N-terminus of TrMgTx were cleaved using factor Xa protease (Thermo Fisher Scientific, Waltham, MA, USA, Cat. # 32521) to generate UrMgTx. 300 µg of TrMgTx was mixed with factor Xa at enzyme to substrate ratio of 1:100 in TBS buffer (50 mM Tris, 100 mM NaCl, 6 mM $CaCl_2$ and pH 8.0) and incubated overnight at 25 ℃. Next day, samples treated with or without enzyme were analyzed on 16% tricine/6M urea-SDS PAGE. To purify UrMgTx, the cleaved His-tag and undigested peptide fragments were captured with pre-charged Ni^+ beads, centrifuged at high speed for 1 min to remove the beads and supernatant was loaded on reversed phase C_{18} analytical column (4.6 mm × 250 mm, 5 µM bead size, Vydac® 218TP) using a HPLC system and eluted with a linear gradient of 10-30% of solvent B (0.1 % TFA in 95% acetonitrile) in Solvent A (0.1% TFA in deionized distilled water) over 25 min. Purified UrMgTx was vacuum dried and stored at –20 ℃ for further experiments.

4.4 Cell culture

4.4.1 CHO

Chinese hamster ovary (CHO) cells were cultured following standard procedures in Dulbecco's modified Eagle's medium (DMEM, Thermo Fisher Scientific, Waltham, MA, USA, Cat. # 11965084) containing 10% fetal bovine serum (FBS), 2 mM L-glutamine and 100 µg/ml streptomycin and 100 U/ml penicillin-g (Sigma-Aldrich) in a humidified incubator at 37 °C and 5% CO_2. Cells were passaged thrice in a week following a 2–5 min incubation in 0.05% trypsin-EDTA solution.

4.4.2 Isolation and activation of PBMCs

Human venous blood from anonymized healthy donors was obtained from blood bank. (Blood samples were collected by having approval from the Ethical Committee of the Hungarian Medical Research Council (36255-6/2017/EKU)). Peripheral blood mononuclear cells (PBMCs) were isolated through Histopaque1077 density gradient centrifugation. Cells obtained were resuspended in Roswell Park Memorial Institute (RPMI) 1640 medium containing 10% fetal calf serum (Sigma-Aldrich), 100 µg/ml penicillin, 100 µg/ml streptomycin, and 2 mM L-glutamine, seeded in 24-well culture plate at density of 5×10^5 cells per ml and grown in a 5% CO_2 incubator at 37 °C for 3 to 6 days. Phytohemagglutinin A (PHA) was added in 5, 7 and 10 µg/ml concentration to the medium to active the PBMCs and boost up the $K_V1.3$ channel expression.

4.5 Single-cell electrophysiology

4.5.1 Plasmid Construction for Tandem Dimers

To construct the $K_V1.3$–$K_V1.3$ tandemly linked dimer, the *KCNA3* gene (GenBank accession no. NM_002232.5) was amplified from $K_V1.3$-pCMV6-XL4 vector (Cat. # SC118765, OriGene Technologies, Rockville, MD, USA) by PCR using primers set (P1 and P2 shown in Table 3) in such a way that it lacks the stop codon and have coding sequence for a short flexible linker (GSG) at 3′-end as shown in Fig. 11A and cloned into the pEGFP-C1 vector using *Bgl*II and *Eco*RI restriction sites. Subsequently, a second copy of the *KCNA3* gene (including the stop codon) was amplified using the primer set (P3 and P4 listed in Table 3). The reverse primer added two additional restriction sites *Hind*III and *Xho*I at 3′-end for the ease of cloning multiple tandemly linked domains. The second copy of *KCNA3* gene cloned

downstream of the first copy of *KCNA3* in the K_V1.3-pEGFP-C1 plasmid using *Eco*RI and *Sal*I restriction sites as shown in Fig. 11B. The *KCNA5* gene (GenBank accession no. NM_002234.4) was amplified from K_V1.5-pEYFP-C1 plasmid (a kind gift from A. Felipe, University of Barcelona, Barcelona, Spain) using primer set (P5 and P6 given in Table 3) The K_V1.3–K_V1.5 tandem dimer was made by replacing the second copy of the *KCNA3* gene in K_V1.3-K_V1.3 pEGFP-C1 plasmids with the *KCNA5* gene using *Eco*RI and *Hind*III endonucleases as demonstrated in Fig. 11C. All the PCRs were performed using Phusion™ high-fidelity DNA polymerase (Thermo Fisher Scientific, Waltham, MA, USA) following manufacturer's instructions. In-frame ligation and gene sequences were confirmed by DNA sequencing.

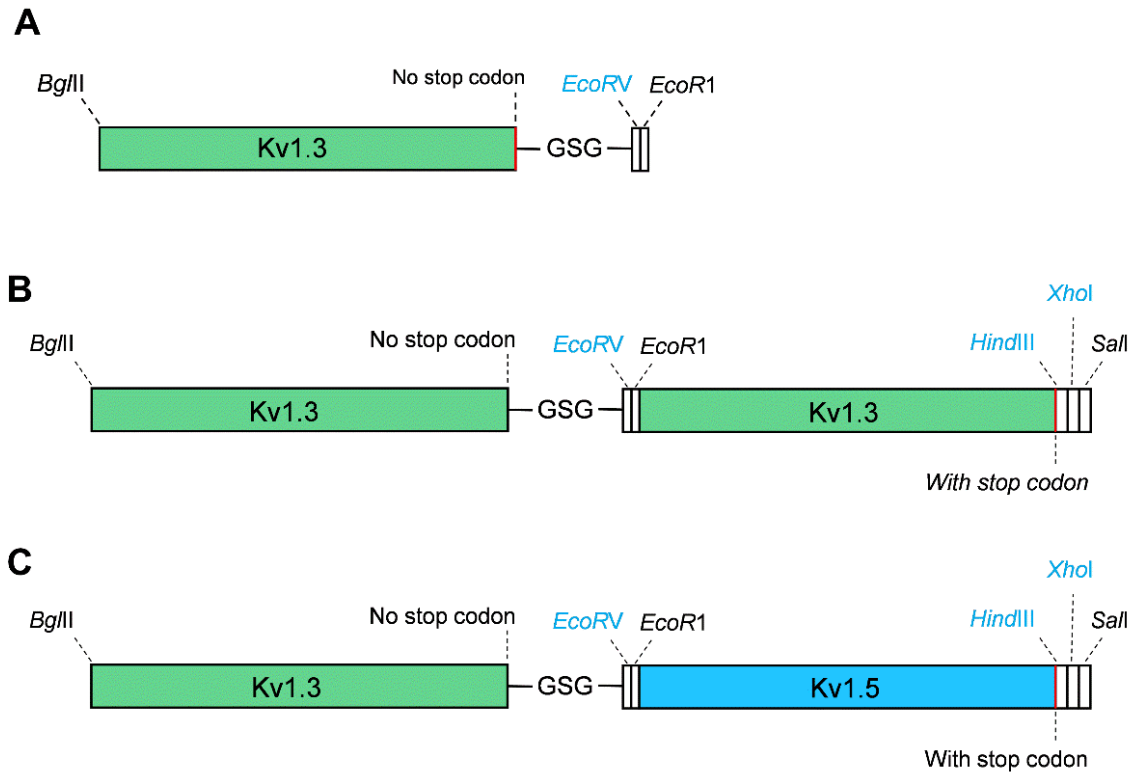

Figure 11: **Representation of the scheme for generating expression cassettes for tandemly linked K_V1 domains.** (**A**) expression cassette for K_V1.3 lacking the stop codon. (**B**) tandemly linked dimer of K_V1.3-K_V1.3 (**C**) tandemly linked dimer of K_V1.3-K_V1.5

Table 3: **List of primers to amplify the *KCNA3* and *KCNA5* genes for tandemly linked dimer homo/heterotetramers.**

Primer	Sequence	Length
P1	CAAGATCTATGGACGAGCGCC	21
P2	GAATTCACCGATATCTCCAGAGCCAACATCGGTGAATATC	40
P3	TCGAATTCATGGACGAGCGCCTC	23
P4	ATGTCGACCGTCTCGAGTCCAAGCTTTTAAACATCGGTGAATATC	45
P5	AAGAATTCATGGAGATCGCCCTGG	24
P6	TGAAGCTTTTACAAATCTGTTTCCCGGCTG	30

Underlined sequences represent the restriction sites; *Bgl*II, *Eco*R1, *Eco*RV, *Sal*I, *Xho*I, HindIII.

4.5.2 Heterologous expression of ion channels

CHO cells were transiently transfected using Lipofectamine 2000 kit (Invitrogen, Waltham, MA, USA) according to manufacturer's protocol with the ion channel coding vectors shown in Table 4. Cells were co-transfected with a GFP expressing plasmid when the target ion channel gene lacked the fluorescent tag. GFP or YFP-positive transfectants were identified with a Nikon TS-100 fluorescence microscope (Nikon, Tokyo, Japan) using bandpass filters of 455−495 nm and 515−555 nm for excitation and emission, respectively and currents were recorded 20−30 h post-transfection.

Table 4: **List ion channel-coding plasmids for heterologous expression**

Ion channel	Gene name	Plasmid	Source
$hK_V1.1$	*KCNA1*	pCMV6-AC-GFP	OriGene Technologies, Rockville, MD, USA
$hK_V1.2$	*KCNA2*	pCMV6-AC-GFP	OriGene Technologies, Rockville, MD, USA
$hK_V1.4$	*KCNA4*	pcDNA3	Heike Wulff, University of California, Davis, CA, USA
$hK_V1.5$	*KCNA5*	pEYFP-C1	A. Felipe, University of Barcelona, Barcelona, Spain
$hK_V1.6$	*KCNA6*	pCMV6-AC-GFP	OriGene Technologies, Rockville, MD, USA
$hK_{Ca}3.1$	*KCNN4*	pEGFP-C1	Heike Wulff, University of California, Davis, CA, USA
$hNa_V1.5$	*SCN5A*	pcDNA3	H. Abriel, University of Bern, Bern, Switzerland
hH_V1	*VCN1*	pcDNA3	Kenton Swartz, NIH, Bethesda, MD, USA
$K_V1.3$-Kv1.3 tandemly linked dimer		pEGFP-C1	Created in this study
$K_V1.3$-Kv1.5 tandemly linked dimer		pEGFP-C1	Created in this study

Human embryonic kidney (HEK) 293 cells stably expressing $hK_V11.1$ (*hERG1*, *hKCNH2* gene, a kind gift from H. Wulff, University of California, Davis, CA, USA), $mK_{Ca}1.1$(BK_{Ca}, *mKcnma1*, a kind gift from C. Beeton, Baylor College of Medicine, Houston, TX, USA) and $hNa_V1.4$ (*hSCN4A* gene, a kind gift from P. Lukács, Eötvös Loránd University, Budapest, Hungary) were used.

4.5.3 Patch-clamp electrophysiology recording conditions

Whole-cell currents were measured using patch-clamp technique in voltage-clamp mode following standard protocols [198]. All recordings were performed using Multiclamp 700B amplifier connected to a personnel computer with Axon Digidata1440 digitizer and for data acquisition, Clampex 10.7 software was used (Molecular Devices, Sunnyvale, CA, USA). In general, current traces were lowpass-filtered by using the built-in analog four-pole Bessel filters of the amplifier and sampled (4-50 kHz) at least twice the filter cutoff frequency. Micropipettes were pulled from GC150F-7.5 borosilicate capillaries (Harvard Apparatus, Kent, UK) with tip resistance typically ranging 3-6 MΩ in the bath solution. Only those records were used for data analysis when the leak current at holding potential was <10% of peak current at the test potential. Recordings were carried out at room temperature (20-25°C). Control and test solutions were perfused to the cell through gravity flow perfusion system. Excess bath solution was removed constantly with vacuum suction.

4.5.4 Solutions

For patch-clamp measurement extracellular and intracellular solutions were, generally, prepared according to recipes given in Table 5 and 6 for respective channels. To record the tail current of $K_V1.2$ the bath solution (HK-20) contained 130 mM NaCl and 20 mM KCl, other components remained unchanged. In the HK-150 bath all Na^+ was substituted by K^+ to yield 150 mM K^+ concentration. In the Na^+-free extracellular solution all Na^+ was substituted by Choline-Cl, other components remained unchanged. Equimolar substitution of Na^+ for tetraethylammonium-Cl was used in the various TEA^+-containing solutions. The osmolarity of the extracellular solutions was between 302 and 308 mOsm/L and for internal solutions was ~ 295 mOsm/L. All the bath solutions were supplemented with 0.1 mg/ml bovine serum albumin (BSA) to prevent toxin adsorption to the plastic surfaces of the perfusion system.

Table 5: **Recipe for extracellular/bath solution for patch-clamp recordings**

	K_V1.x, mK_{Ca}1.1 and Na_V1.x	**K_V11.1**	**K_{Ca}3.1**	**hH_V1**
NaCl (mM)	145	-	-	-
KCl (mM)	5	5	5	-
$CaCl_2$ (mM)	2.5	2	2.5	-
$MgCl_2$ (mM)	1	2	1	6
HEPES (mM)	10	10	10	-
Glucose (mM)	5.5	20	5.5	5.5
Cholin Cl (mM)	-	140	-	-
$CdCl_2$ (mM)	-	0.1	-	-
Na^+-aspartate (mM)	-	-	145	60
MES (mM)	-	-	-	80
pH	7.35	7.35	7.4	7.4

Table 6: **Recipe for intracellular/pipette solution for patch-clamp recordings**

	K_V1.x and mK_{Ca}1.1	**K_V11.1**	**K_{Ca}3.1**	**Na_V1.x**	**hH_V1**
KF (mM)	140	-	-	-	-
KCl (mM)	-	140	-	-	-
$CaCl_2$ (mM)	1	-	8.5	-	-
$MgCl_2$ (mM)	2	2	2	-	6
HEPES (mM)	10	10	5	10	-
EGTA (mM)	11	10	10	10	-
NaCl (mM)	-	-	-	10	-
CsF (mM)	-	-	-	105	-
K^+-aspartate (mM)	-	-	150	-	-
Na^+-aspartate (mM)	-	-	-	-	90
MES (mM)	-	-	-	-	80
Glucose (mM)	-	-	-	-	3.3
pH	7.22	7.30	7.22	7.2	6.17

4.5.5 Voltage protocols

In general, for all the measurements the holding potential (V_h) was kept at −120 mV and the pulses were delivered every 15 s except when indicated. For recording the currents of K_V1.x and tandemly linked K_V1.3-K_V1.5 channels, 15-2000 ms long voltage pulses to +50 mV were applied. To record the K_V1.3 currents for conductance-voltage (G-V) relationship, activated T cells were depolarized to voltages ranging from -70 mV to +50 mV in steps of 10 mV every 15

s. For instantaneous current-voltage (I-V) relationships of $K_V1.2$ and $K_V1.3$, currents were evoked with 200-ms-long voltage ramps to +50 mV. For recording $K_V11.1$ current, the voltage step to +20 mV for 1.25 s from a V_h of −80 mV was followed by a step to −40 mV for 2 s, applied every 30 s, and the peak (tail) currents were recorded during the latter step. $mK_{Ca}1.1$ currents were evoked by depolarizing the cells to +100 mV for 600 ms from a V_h of −100 mV. For $K_{Ca}3.1$ currents, 150-ms-long voltage ramp to +50 mV from −120 mV was applied every 10 s. Current through human proton channel (hH_V1) was elicited by applying 1.0-s-long voltage ramp to +100 mV from a V_h of −60 mV every 15 s. For the recording of Na^+ currents through $Na_V1.4$ and $Na_V1.5$, 15-ms-long voltage steps to 0 mV were applied every 10 s.

4.5.6 Patch-clamp data analyses

For patch-clamp data analyses, pClamp 10.7 software package (Molecular Devices) was used. Current traces were digitally filtered with a 3-poins boxcar filter and were corrected for ohmic leakage when needed. The inhibitory effect of a peptide toxin at a given concentration was calculated as remaining current fraction (RCF = I/I_0, where I_0 is the peak current in the absence of the toxin, and I is the peak current at equilibrium block at a given toxin concentration). The data points (average of 3-5 individual records) in the dose-response curve were fitted with the Hill equation.

$$\mathrm{RCF} = \frac{\mathrm{K_d^H}}{\mathrm{K_d^H} + [\mathrm{TX}]^{\mathrm{H}}} \tag{1}$$

where [TX] is the concentration of the toxin, K_d is the dissociation constant, and H is the Hill coefficient. To construct the voltage-dependance of steady-state activation of $K_V1.3$, peak conductance (G) at each test potential was calculated from peak current (I) at a test potential (E_m) and the K^+ reversal potential (E_K) using chord-conductance equation $G = I/(E_m - E_K)$. Normalized conductance (G_{norm}) values were calculated by dividing the G values obtained at different test potentials by the maximum value of G and G_{norm} values were plotted as a function of the test potential. The Boltzmann sigmoidal equation was fitted to the data points:

$$G_{norm} = \frac{1}{1 + e^{\left(\frac{V_{50} - E_m}{k}\right)}} \tag{2}$$

where V_{50} is the midpoint voltage, E_m is the test potential, and k represents slope factor of the function. For determination of voltage dependence of steady-state activation of $K_V1.2$,

the membrane was depolarized to different test potentials (ranging from −70 to +80 in 10 mV steps) for 300 ms and the tail currents were recorded at −120 mV. Peak tail currents recorded following various test potentials were normalized to the maximum tail current value and plotted against the corresponding test potential. Data points were fitted with a Boltzmann sigmoidal equation as stated above.

To examine the binding kinetics, normalized peak currents ($I_{norm} = I_t/I_0$, where I_t is peak current in the presence of the toxin at time t and I_0 is peak current in the absence of toxin) were plotted as function of time. Association and dissociation time constants (τ_{on}, τ_{off}) were determined by fitting the data points during the wash-in and wash-out procedures, respectively, with the single exponential functions as shown in Eq. 3 (wash-in) and Eq. 4 (was-out).

$$I_{norm}(t) = RCF + \left((1 - RCF) \times e^{-\frac{t}{\tau_{on}}}\right) \tag{3}$$

$$I_{norm}(t) = RCF + \left((1 - RCF) \times \left(1 - e^{-\frac{t}{\tau_{off}}}\right)\right) \tag{4}$$

These time constants were utilized to calculate the association rate constant (k_{on}) and dissociation rate constant (k_{off}) considering a simple bimolecular interaction between the channel and the toxin, and using Eq. 5 and Eq. 6, also described previously in detail [66, 199]. The dissociation coefficient (K_d) was calculated using Eq. 7.

$$k_{on} = \frac{1 - (\tau_{on} \times k_{off})}{\tau_{on} \times [toxin]} \tag{5}$$

$$k_{off} = \frac{1}{\tau_{off}} \tag{6}$$

$$K_d = \frac{k_{off}}{k_{on}} \tag{7}$$

4.6 Biological assays

4.6.1 Isolation of CD4$^+$ Effector memory T lymphocyte

PBMCs were isolated from healthy donor's blood and cultured as explained above (3.4.2). Dead Cell Removal Microbead Kit (Miltenyi Biotec B.V & CO. KG, Bergisch Gladbach, Germany) was used to eliminate the dead cells and CD4$^+$ T_{EM} lymphocytes were isolated through magnetic cell sorting (negative selection) with the CD4$^+$ Effector Memory T

Cell Isolation Kit (Miltenyi Biotec B.V & CO. KG, Bergisch Gladbach, Germany). Briefly, all types of cells except $CD4^+$ T_{EM} lymphocytes were labeled with a cocktail of monoclonal antibodies (biotin-conjugated anti-CD8, CD14, CD15, CD16, CD19, CD34, CD36, CD45RA, CD56, CD123, CD235a, TCR γ/δ and APC-conjugated anti-CCR7). Next, cells were incubated with anti-APC and anti-biotin secondary antibodies, both coupled with magnetic microbeads. The cell preparation was passed through LD Column (Miltenyi Biotec B.V & CO. KG) mounted on MidiMACS Separator (Miltenyi Biotec B.V & CO. KG) and untouched $CD4^+$ T_{EM} lymphocytes were collected as flow through.

4.6.2 Activation of $CD4^+$ T_{EM} lymphocyte

To compare the effect of TrMgTx and UrMgTx on T cell activation, four treatment groups were designated: 1) unstimulated, 2) stimulated, 3) stimulated + TrMgTx (8.5 nM), and 4) stimulated + UrMgTx (5 nM). For Cm28 functional assay, $CD4^+$ T_{EM} lymphocytes were divided into five different treatment groups: 1) unstimulated and non-treated, 2) unstimulated and treated with Cm28 (1.5 µM), 3) stimulated only, 4) stimulated and treated with Cm28 (1.5 µM), 5) stimulated and treated with margatoxin (UrMgTx, 5 nM, used as control here). The high concentrations of peptide toxins were used to ensure the complete blockade of $K_V1.3$ channels throughout the entire treatment duration and to counterbalance peptide adsorption to plastic surfaces and biological degradation [200-202]. To stimulate lymphocytes through the T cell receptor (TCR), anti-human CD3 monoclonal antibody (clone OKT3, BioLegend, San Diego, CA, USA) was bound to the surface of 96-well cell culture plate (Corning, NY, Cat. # 3599) at 1µg/well or 24-well plate (Corning Inc., Corning, NY, USA, Cat. # 3527) at 5 µg/well in phosphate buffered saline (PBS) at 4 °C overnight. Wells were washed twice with PBS to get rid of unbound antibody. $CD4^+$ T_{EM} cells were suspended at a density of 1×10^6 cells/ml in RPMI 1640 medium supplemented with 10% FBS, 2 mM L-glutamine and 100 µg/ml streptomycin and 100 U/ml penicillin-G. To ensure the complete blockade of $K_V1.3$ prior to activation, cells were incubated with the toxins for 5 min in case of rMgTx and 30 min in case of Cm28 and the plate was incubated in a humidified incubator at 37 °C in 5% CO_2 for 24 h. Each experiment included two technical duplicates and was performed on three different donors.

4.6.3 Cytotoxicity assay

Cellular cytotoxicity mediated by peptide toxins was measured using Pierce lactate dehydrogenase (LDH) Cytotoxicity Assay Kit (Thermo Fisher Scientific, Waltham, MA, USA)

following manufacturer's instructions. Briefly, to determine the LDH activity of a medium 50 µl samples were obtained from the cultures following 24 h growth of the cells (stimulated or unstimulated in the presence or absence of toxin, spontaneous and maximum LDH activity controls) and were mixed with 50 µl reaction mix (substrate) in the flat bottom 96-well plate (Corning, NY, Cat. # 3599) and incubated for 30 min in dark. After adding the 50 µl of stop solution, absorbance was measured at 490 nm and 680 nm using Spark® Multimode Microplate Reader (Tecan Trading AG, Switzerland). LDH activity was determined by subtracting A_{680} (background) from the A_{490} and % cytotoxicity was calculated using Eq. 8.

$$\% \text{ Cytotoxicity} = \frac{\text{Toxin treat LDH activity} - \text{spontaneous LDH activity}}{\text{Maximum LDH activity} - \text{spontaneous LDH activity}} \times 100 \quad (8)$$

Cells treated with sterile water and lysis buffer for 45 min at 37 °C were used as spontaneous and maximum LDH activity controls, respectively. For experimental positive control, cells were treated with 50 mM Sodium Azide (NaN_3). The experiment was repeated for three different donors.

4.6.4 Flow cytometry

For assessing the cell viability, Zombie NIR fixable viability Dye (Cat. # 423105, BioLegend, San Diego, CA, USA) was used. Cells were washed with PBS and incubated with Zombie NIR dye (at 1:500 dilution in 100 µl PBS) at room temperature for 20 min in dark. For staining the cells with fluorescent antibodies, cells were washed with PBS supplemented with 1% FBS and stained with PerCP/Cyanine5.5 conjugated anti-human CD25 (IL2R) antibody (clone BC96, BioLegend) and fluorescein isothiocyanate (FITC) conjugated anti-human CD154 (CD40L) antibody (clone 24−31, BioLegend, San Diego, CA, USA) in 100 µl PBS+1% FBS at 4 °C for 20 min in dark. Cells were then washed with the PBS+1% FBS buffer and finally, resuspended in 150 µl PBS+1% FBS for flow cytometer analysis. For staining the CHO or stably expressing mGFP-K_V1.3 CHO cells with Cy5-HsTX1[R14A] cells were washed twice with PBS containing 2% (v/v) FBS and incubated with 10 nM Cy5-HsTX1[R14A] in the dark at room temperature for 20 min. Cells were then washed with PBS containing 2% (v/v) FBS and resuspended in the same buffer for flow cytometry analysis. For the competition assay, cells were preincubated for 20 min with 100 nM unconjugated HsTX1[R14A] or 1 µM rMgTx before adding the Cy5-HsTX1[R14A].

Samples were measured using a NovoCyte 3000 RYB flow Cytometer (ACEA Bioscience Inc., San Diego, CA, USA). Zombie NIR dye was excited by red laser (640 nm) and

780/60 nm emission filter was used. FITC and PerCP/Cyanine5.5 were excited by using blue laser (488 nm), and 530/30 nm and 695/40 nm emission filters were used, respectively. GFP and Cy5 were excited with blue (488 nm) and red (640 nm) lasers, and the emission filters 530/30 nm and 660/20 nm were used for GFP and Cy5, respectively. 10,000–20,000 events were recorded for each sample and data were analyzed using FCS Express 6.0 (De Novo Software, Glendale, CA, USA). Briefly, live cells were gated based on their forward scatter (FSC) and side scatter (SSC) parameters. Histograms corresponding to IL2R (CD25), CD40L and Cy5-HsTX1[R14A] were generated as peak-normalized overlays. Unstained cell controls (negative) were always used for comparison. Mean fluorescent intensities (MFIs) of IL2R (CD25) and CD40L were normalized to that of their stimulated but not treated control. To determine cell viability, positive staining with the Zombie NIR and changes in FSC were considered as indicators of dead cells. Cells treated with 30% of DMSO were used as positive control for the viability dye.

4.6.5 Statistics

Statistical analyses and graph generation was executed in GraphPad Prism software (version 8.0.1, San Diego, CA, USA). For all the experiments, data were presented as mean ± SEM. For pairwise comparison, student's *t* test with Mann-Whitney rank sum test and for multiple comparisons, one-way ANOVA with post hoc Tukey's test was performed. Statistical significance is indicated in terms of P values.

5. RESULTS

5.1 Pharmacological and functional characterization of a novel K_V1.3 inhibitor toxin from *C. margaritatus* scorpion

Our laboratory has a more than 20-year long history of collaboration with Prof. Lourival D. Possani and his colleagues (institute of Biotechnology, UNAM, Mexico). In the past we have described several peptide toxins isolated for scorpion. The collection of scorpions, venom extraction and purification of peptides is performed in Prof. Possani's laboratory, while the pharmacological and biological properties are mainly studied in our facility using single-cell electrophysiology and cellular assays.

Centruroides margaritatus is a scorpion belonging to the *Buthidae* family and classified as a synanthropic species whose venom is less toxic with LD_{50} of 59.9 mg/kg [203]. The venom of this scorpion has not been explored fully except a well-known peptide MgTx which was isolated and characterized a long time ago. Recently, a detailed proteomic analysis of *C. margaritatus* venom was performed by our collaborators [195] and in addition to a K_V11.1 inhibitor toxin CmERG1 (γ-KTx 10.1) they found a novel peptide with molecular weight (MW) 2820.5 Da. This peptide was named "Cm28" corresponding to the scorpion's name *C. margaritatus* and its MW. Cm28 has a unique and short primary structure with only 27 amino acid residues and three potential disulfide bridges. Sequence comparison with all the known KTx scorpion toxins revealed it has less than 40% similarity with α-KTxs and lacks the typical functional dyad (Lys-Tyr) required to block K_V channels with high affinity (Fig. 12). In this

```
                                      10        20        30        40    len    %ID
                                ....|....|....|....|....|....|....|....|..
Cm28                            -----KCRECGN--TSPSC------YFSGNCVNGKCVCPA--    27    100
ε-KTx_1.1|T. serrulatus|P0C174  ---KP..GL.RYRCC.GG.-------S..K....A.D.S---    29     42
ε-KTx_1.2|T. serrulatus|P0C175  ---TV..GG.NRKCCAGG.-------R..K.I...Q.Y*--    30     39

α-KTx_13.4|T. stigmurus|P0C8L2  --------G.RQ--CGGG.------NKH.K.I...K.Y*--    24     33
α-KTx_13.1|T. obscurus|P83243   -----A.GS.RKK-CKG----------..K.I..R.K.Y---    23     32
α-KTx_13.3|T. pachyurus|P84630  -----A.GS.RKK-CKG----------P.K.I..R.K.Y*--    24     29
α-KTx_23.2|V. mexicanus|P0DJ32  -AAAIS.VGSKE--CL.K.KA--QGCK..K.M.K..K.YC--    35     29
α-KTx_2.1|C. noxius|P08815      TIINV..TSPKQ--C.KP.KELYGSSAGAK.M...K.YNN*    40     25
α-KTx_2.8|C. elegans|P0C161     TVINV..TSPKQ--CLKP.KDLYGPHAGAK.M...K.YNN-    39     23
```

Figure 12: **Multiple alignment of Cm28 with other representative KTx.** Len; indicates mature chain length; %ID; indicates percent amino acid identity. Conserved cysteine residues are highlighted in yellow. Identical positions to those in Cm28 are indicated by dots and (*) indicates that the C-terminus is amidated. The Uniprot ID of Cm28 is α-KTx 32.1.

section of my thesis, I characterized the pharmacological and immunological activities of this novel toxin Cm28.

5.1.1 Cm28 inhibits human $K_V1.2$ and $K_V1.3$ with low-nanomolar affinity

The primary structural features of Cm28 are unusual and exceptional among other scorpion toxins. Therefore, to assess whether this toxin has any pharmacological activity against K^+ channels, we first aimed to test the effects of Cm28 on two human K^+ channels; $K_V1.2$ and $K_V1.3$. The whole-cell $K_V1.2$ currents were measured in transiently transfected CHO cells (see Materials and Methods for detail). Channels were activated by series of depolarization pulses to +50 mV from −120 mV. Due to highly variable activation kinetics of $K_V1.2$ [204], 15-500-ms long pulses every 15 s were applied to maximize open probability of the channel. The slower inactivation rate of $K_V1.2$ prevented inactivation even at 500-ms-long depolarization pulses. For $K_V1.3$ current measurements, human peripheral T lymphocytes were activated by Phytohemagglutinin A (PHA) to boost up the expression of $K_V1.3$ channels and the pipette-filling solution was Ca^{2+} free to avoid $K_{Ca}3.1$ channel activation. Thus, the whole-cell currents were recorded exclusively through $K_V1.3$ channels, as previously [152, 163]. The $K_V1.3$ currents were evoked by 15-ms-long depolarization pulses to +50 mV. The use of short pulses every 15 s ensured that there is no cumulative inactivation of $K_V1.3$ channel. Cm28 dissolved freshly in the extracellular solution was applied through a custom-built micro perfusion system at rate of 200 µl/min. The complete exchange of solution in the bath chamber *i.e.*, the proper operation of the perfusion apparatus was confirmed frequently using fully reversible inhibitors as positive controls at a concentration equivalent to their K_d values (*i.e.*, 14 nM ChTx for $K_V1.2$ (Fig. 13A) and 10 mM tetraethylammonium (TEA^+) for $K_V1.3$ (Fig. 13B), and the approximate 50% reduction in peak current was an indicator of both the ion channel and the proper operation of the perfusion system.

Fig. 13A represents the whole-cell currents through $K_V1.2$ recorded sequentially in the same cell, before (control trace, black) and after perfusing the cell with 2 nM Cm28 till the equilibrium block (purple trace). At equilibrium block, Cm28 showed ~70% reduction in current amplitude. The block was almost fully reversible upon washing the perfusion chamber with toxin-free solution (wash-out trace, green in Fig. 13A). The onset and recovery from the block of $K_V1.2$ currents at 2 nM Cm28 are shown in Fig. 13C. Normalized peak currents were plotted as a function of time. Both the association and dissociation processes of Cm28 were very slow, accordingly, development of equilibrium block and recovery up to ~85% of control

current took several minutes. In a similar set of experiments for $K_V1.3$, 2 nM Cm28 inhibited ~58% of the $K_V1.3$ current upon reaching the block equilibrium. Fig. 13B displays the current traces recorded sequentially in the same T lymphocyte, in the presence (red trace) and absence (black trace) of Cm28 peptide. Like $K_V1.2$, the block of $K_V1.3$ was also reversible (90% recovery took 10 min) upon perfusing the cell with toxin-free solution (wash-out trace, green in Fig. 13B). The onset of steady-state block and relief from the block took comparatively less time than for $K_V1.2$ indicating that the association and dissociation steps are faster for $K_V1.3$ than $K_V1.2$ (Fig.13D).

To determine the concentration-dependent block of $K_V1.2$ and $K_V1.3$ channels by Cm28 different concentrations of Cm28 were applied to the cells for an adequate duration to reach equilibrium block, considering the slow blocking kinetics especially at low toxin concentrations. The remaining current fractions (RCF) value for each given concentration of toxin were calculated and fitted with Hill equation (Eq. 1, see Materials and Methods section for detail) to obtain dose-response curves. The resulting dissociation constant (K_d) values and Hill coefficients (H) were K_d = 0.96 nM, H = 1.04 for $K_V1.2$ (Fig. 13E) and K_d = 1.3 nM, H = 0.93 for $K_V1.3$ (Fig. 13F). Cm28 showed a similar affinity for both channels.

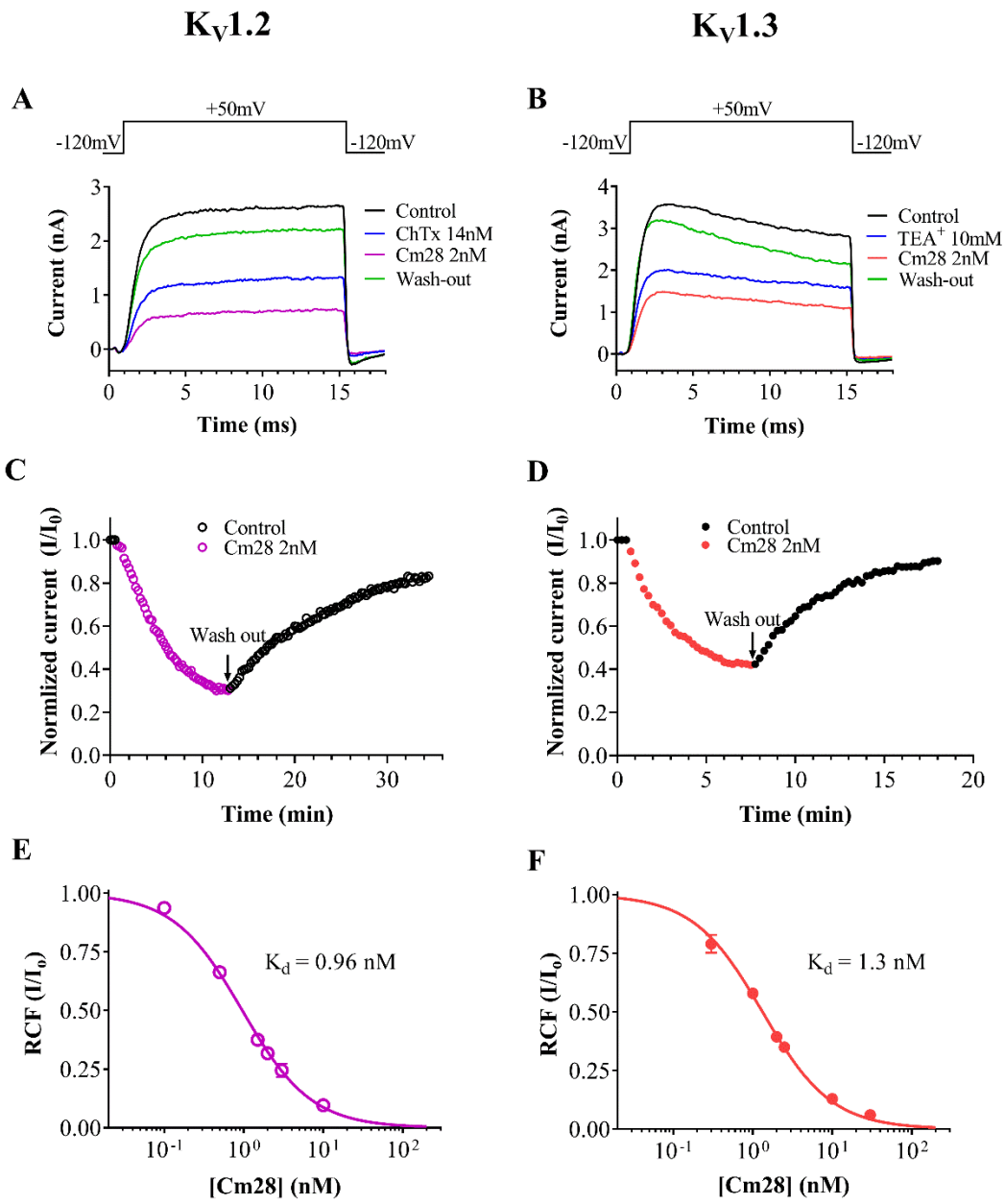

Figure 13. **Inhibition of K_V1.2 and K_V1.3 currents by Cm28. (A, B)** Whole-cell currents of K_V1.2 (A) and K_V1.3 (B) were recorded in transiently transfected CHO cells and in activated human T lymphocytes, respectively, by applying 15-ms-long voltage pulses to +50 mV from a V_h of −120 mV every 15 s. Representative current traces show the K^+ current in control solution (black), at equilibrium block in the presence of 14 nM ChTx: Charybdotoxin for K_V1.2, and 10 mM TEA^+: tetraethylammonium for K_V1.3, (blue traces in panel A and B, respectively) as a perfusion control, at equilibrium block upon application of 2 nM Cm28 (purple for K_V1.2, red for K_V1.3) and after recovery from the block upon application of toxin-free solution (green, wash-out). **(C, D)** Time course of development and recovery of the K^+ current inhibition. Normalized peak currents were plotted as a function of time. Data points in purple (C, K_V1.2) and in red (D, K_V1.3) represent the application of 2 nM of Cm28 to the bath solution. Upon reaching the block equilibrium, cells were perfused with toxin-free solution (arrow, wash out) to

demonstrate reversibility of the block (data points in black). **(E, F)** Concentration-dependent block of $K_V1.2$ (E) and $K_V1.3$ (F) by Cm28. A Hill equation (Eq. 1) was fitted to the RCF values calculated at different toxin concentrations (solid lines). The best fit resulted in K_d = 0.96 nM, H= 1.04 for $K_V1.2$ (E) and K_d = 1.3 nM, H = 0.93 for $K_V1.3$ (F). Error bars represent SEM and n = 3-5.

5.1.2 Mechanism of block

Generally, most of the known toxins inhibit the K_V channels either by physically occluding the pore region or by modulating the voltage-sensor of the channel as discussed in detail under section 2.7.1. To determine the mechanism behind the $K_V1.2$ and $K_V1.3$ block by Cm28 we studied the effect of Cm28 on the threshold voltage of activation and voltage dependence of steady-state-activation of both ion channels. Instantaneous current-voltage relationship (I-V) was recorded using CHO cells for $K_V1.2$ and activated T cells for $K_V1.3$ (Fig. 14A-B). Currents were evoked by applying 200-ms-long voltage ramps from −120 mV to +50 mV every 15 s. Cm28 did not shift the threshold voltage of activation of either current. The current traces in control solution and at the equilibrium block with 2 nM Cm28 showed a similar threshold voltage of activation; ~ −23 mV for $K_V1.2$ (Fig. 14A) and ~ −40 mV for $K_V1.3$ (Fig. 14B).

For construction of conductance-voltage (G-V) relationship for $K_V1.2$, isochronal tail current peaks were recorded in CHO cells at −120 mV followed by 300-ms long depolarizations ranging from −70 to +80 in 10 mV steps from V_h −120 mV in HK-bath containing 20 mM K^+ to increase the tail currents. Due to highly variable activation properties [204], only those records were considered for analysis which had similar gating mode. Normalized tail current peaks were plotted as a function of membrane potential (E_m) in Fig. 14C, the solid lines represent the best fit Boltzmann sigmoidal function (Eq. 2). Cm28 did not introduce any substantial shift in the G-V curve of $K_V1.2$ (Fig. 14C). The midpoint voltage (V_{50}) of the G-V relationship for $K_V1.2$ was 21 ± 3 mV in the control solution (n = 5) and 15 ± 4 mV at equilibrium block with 2 nM Cm28 (n = 5). Fig. 14E indicates that the difference between V_{50} for $K_V1.2$ in the presence or absence of Cm28 was statistically nonsignificant. For the G-V relationship of $K_V1.3$, whole-cell currents in the activated human T lymphocytes were measured in response to voltage pulses ranging from −70 to +50 mV in 10 mV steps from V_h of −120 mV and conductance values were calculated for each test potential and normalized for the maximal conductance. The best fit of the Boltzmann sigmoidal function (Eq. 2) to the averaged data points yielded the superimposed solid lines as shown in Fig. 14D and indicating that there is no change in the voltage dependence of steady state activation of $K_V1.3$ in the presence of Cm28

at 2 nM, like for $K_V1.2$. The V_{50} values for $K_V1.3$ were similar in the control solution (V_{50} = −20 ± 3, n = 4) and at equilibrium block with 2 nM Cm28 (V_{50} = −19 ± 2, n = 4) as shown in Fig. 14E. As the voltage dependence of steady-state-activation and threshold voltage of activation were not affected by the Cm28 for both $K_V1.2$ and $K_V1.3$ ion channels, it suggests that Cm28 is not a gating modifier rather it interacts with the pore region of ion channels.

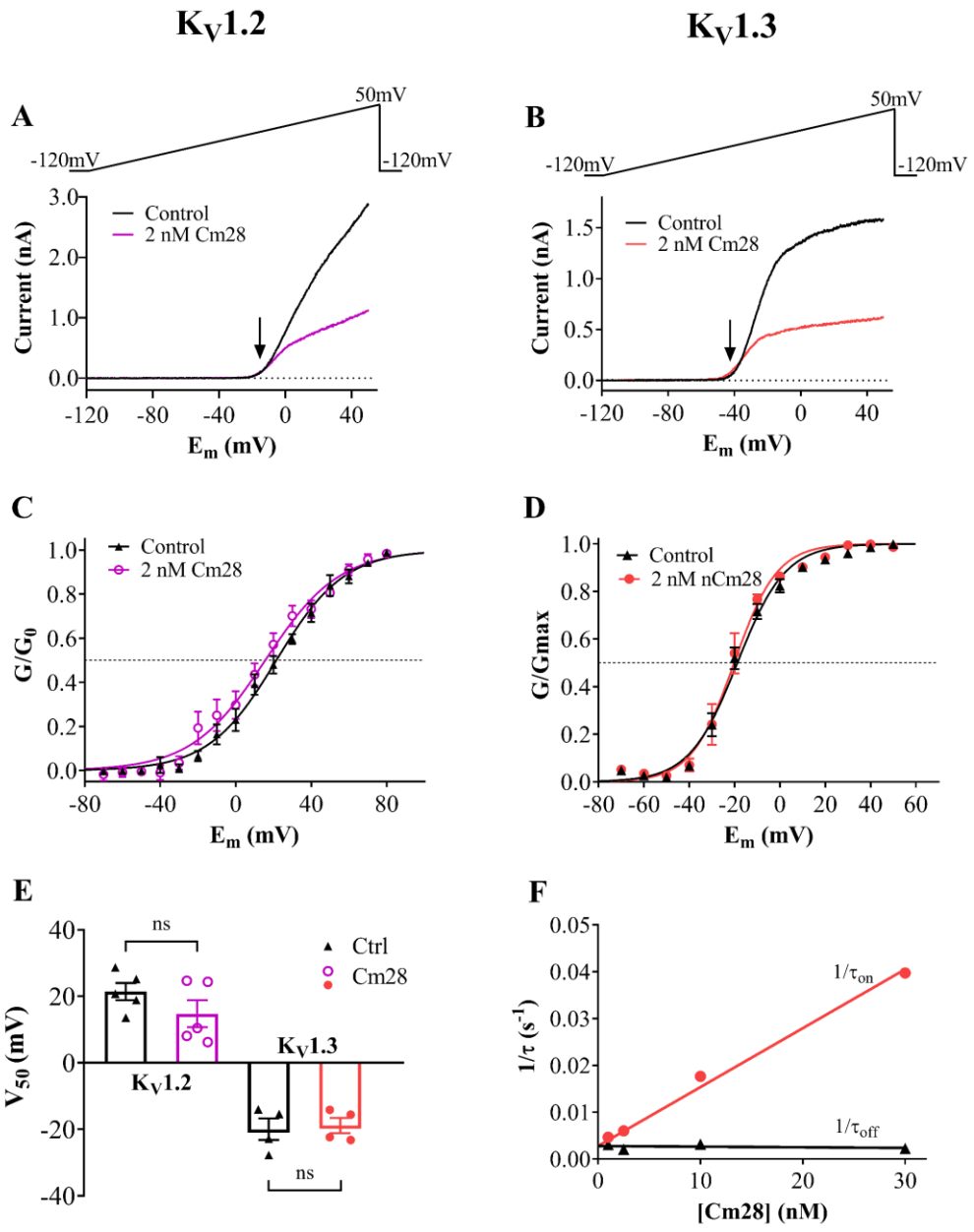

Figure 14: **Mechanism of blocking $K_V1.2$ and $K_V1.3$ by Cm28. (A, B)** Instantaneous current-voltage relationship for $K_V1.2$ (A) and $K_V1.3$ (B). Cells were held at −120 mV and depolarized to +50 mV in 200 ms using a voltage ramp protocol (at a rate of 0.85 mV/ms). Test pulses were applied every 15 s. Representative traces show the average of three traces either in control solution (black) or at equilibrium

block in the presence of 2 nM Cm28 (purple for $K_V1.2$ in panel A and red for $K_V1.3$ in panel B). Arrows (in black) indicate the activation threshold voltages. **(C, D)** G-V curve for $K_V1.2$ (C) was constructed from isochronal tail current amplitudes recorded in CHO cells at −120 mV. Currents were activated by 300-ms-long depolarizing test potentials ranging from −70 to +80 mV in 10 mV increments from a V_h of −120 mV. Tail currents were normalized to maximum and plotted as a function of membrane protentional (E_m). To obtain the G-V curve of $K_V1.3$ (D), whole-cell currents were recorded by applying voltage pulses ranging from −70 to +50 mV in 10 mV steps from V_h of −120 mV. Then, normalized conductance was calculated using the chord-conductance equation (see Materials and Methods) and plotted against membrane potential (E_m). The Boltzmann sigmoidal equation (Eq. 2) was fitted to the averaged data points (solid lines). The voltage dependence of steady-state activation curve was determined in the absence (filled up triangles in black) or in the presence (empty circles in purple for $K_V1.2$ and filled circles in red for $K_V1.3$) of 2 nM Cm28. **(E)** V_{50} values from G-V curves of individual cells were averaged and plotted as bar graphs. Symbols indicate individual data points. Mann-Whitney test, P = 0.23 ($K_V1.2$) and P = 0.57 ($K_V1.3$) **(F**) Effect of Cm28 concentrations on the binding kinetics to $K_V1.3$. The $1/\tau_{on}$ values, (filled circles in red) and dissociation rate constant ($1/\tau_{off}$ or $k_{off,}$ up triangles in black) were plotted as a function of Cm28 concentrations. Data points were fitted with linear regression ($r^2 = 0.99$). **(C-F)** Error bars represent SEM and $n \geq 3$.

Furthermore, the binding kinetics of Cm28 toxin were also studied. Fig. 14F displays the analysis of kinetic parameters of the development of $K_V1.3$ current inhibition at different Cm28 concentrations. The time constant for the development of the block (τ_{on}, association or wash-in time constant) was obtained by fitting a single-exponential equation (Eq. 3) as decay function to the normalized peak currents in the presence of Cm28 (Fig. 13D). The time constant for the recovery from block (τ_{off}, dissociation or wash-out time constant) was determined by fitting a single exponential equation (Eq. 4) as rising function to the normalized peak currents during the wash-out procedure (Fig. 13D). With the assumption of a simple bimolecular reaction between the toxin and the channel, the resulting wash-in and wash-out time constants can be expressed as follows:

$$\tau_{on} = \frac{1}{k_{on} \times [Cm28] + k_{off}} \tag{9}$$

$$\tau_{off} = \frac{1}{k_{off}} \tag{10}$$

where k_{on} is second-order association rate constant and k_{off} is the first-order dissociation rate constant and [Cm28] is the toxin concentration. Plotting the $1/\tau_{on}$ and dissociation rate constant ($1/\tau_{off}$ or k_{off}) values as a function of the Cm28 concentrations showed that the $1/\tau_{on}$

increases linearly with toxin concentration, whereas the dissociation rate remains constant with $k_{off} = 0.0028 \pm 2.15 \times 10^{-4}$ s^{-1}, similar to ChTx binding to *Shaker* as described previously [66]. The slope of superimposed regression line fitted to the $1/\tau_{on}$ data points, using 0.0028 s^{-1} as the y-intercept, corresponds to second-order rate constant of association with $k_{on} = 0.0013 \pm 2.6 \times 10^{-5}$ nM^{-1} s^{-1} ($r^2 = 0.99$) (Table 7).

Similarly, the association (τ_{on}) and dissociation (τ_{off}) time constants of $K_V1.2$ blockade at 2 nM Cm28 were determined by fitting the single exponential function to data points during the wash-in procedure and wash-out procedure (Fig. 13C). Like $K_V1.3$, assuming the bimolecular interaction between the toxin and the channel k_{on} and k_{off} rate constant were calculated using the above-mentioned equations and time constants (Table 7). The dissociation constants ($K_d = k_{off}/k_{on}$) calculated from the block kinetics yielded 1.18 nM for $K_V1.2$ and 2.15 nM for $K_V1.3$, as given in Table 7, that are in good agreement with the K_d values obtained from equilibrium block (Fig. 13E-F).

Table 7. **Kinetic parameters for binding of Cm28 to $K_V1.2$ and $K_V1.3$ channels**

	$K_V1.2$	$K_V1.3$
k_{on} ($nM^{-1}s^{-1}$)	$0.0011 \pm 7.17 \times 10^{-5}$	$0.0013 \pm 2.63 \times 10^{-5}$
k_{off} (s^{-1})	$0.0013 \pm 2.94 \times 10^{-5}$	$0.0028 \pm 2.15 \times 10^{-4}$
K_d (nM)	1.18 ± 0.047	2.15 ± 0.12

For $K_V1.2$, the k_{on} and k_{off} were calculated from time constants (τ_{on}, τ_{off}) for the onset and recovery of the block in the presence of 2 nM Cm28. For $K_V1.3$, k_{on} and k_{off} were determined by fitting the $1/\tau_{on}$ and $1/\tau_{off}$ values with linear regression function (Fig. 14F, see Results for details). K_d was determined as k_{off}/k_{on}. Values are given as mean ± SE, n = 4.

5.1.3 Selectivity profile of Cm28

Next, to fully characterize the pharmacological properties of Cm28, we investigated its effect on various physiologically crucial ion channels. First, we tested whether two other members of voltage-gated *Shaker* family channels, $hK_V1.1$ (Fig. 15A) and $hK_V1.5$ (Fig. 15B), that are closely related to Cm28, are sensitive to Cm28. Additionally, we also tested the effect of Cm28 on $hK_V11.1$ (hERG1, Fig. 15C), a voltage-gated cardiac K^+ channel; $hK_{Ca}3.1$ (IKCa1, SK4, Fig. 15D), the Ca^{2+} activated K^+ channel expressed in T lymphocytes; $mK_{Ca}1.1$ (BK, Slo1, MaxiK, Fig. 15E), the large conductance voltage- and Ca^{2+}-activated channel; two voltage-gated Na^+ channels, $hNa_V1.4$ (Fig. 15F) and $hNa_V1.5$ (Fig. 15G), expressed in skeletal and

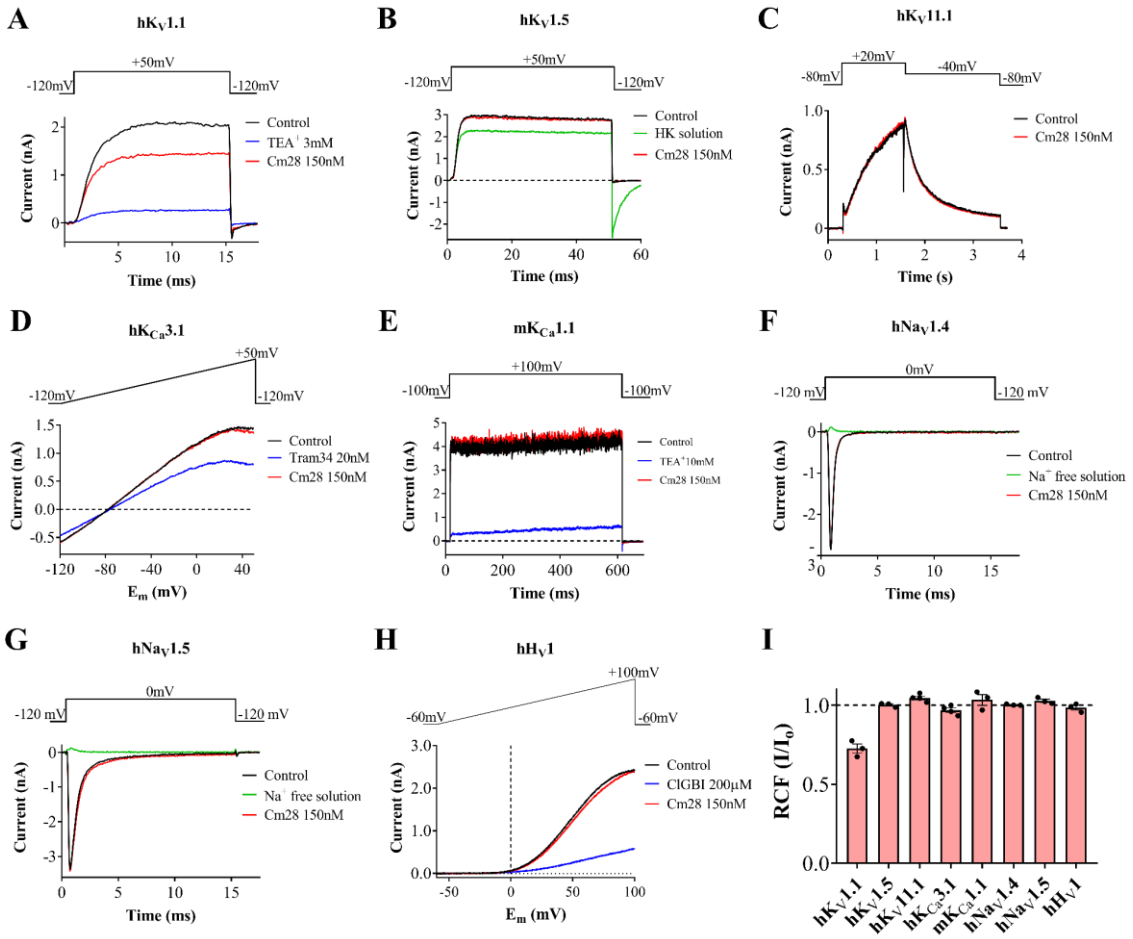

Figure 15: **Selectivity profile of Cm28. (A-H)** Representative current traces of various channels are shown in the absence of (indicated as control in black) and presence of 150 nM Cm28 (>100× of K_d value for K_V1.3) of Cm28 (in red). The proper operation of solution exchange in recording chamber was tested frequently using fully reversible blockers (shown in blue) or solutions (in green) as positive control (HK: HK-150 solution with 150 mM extracellular K^+ to reduce the K^+ driving force or TEA $^+$: tetraethylammonium chloride, Tram34 and ClGBI are known blockers of appropriate channels). Voltage protocols are shown in the inset of each panel. For external and internal solution composition see Materials and Methods section. The traces shown in the presence of 150 nM Cm28 were recorded at equilibrium block (A) or after 8-20 pulses (2−5 min) in the presence of Cm28 (B-H). **(I)** Summary of the remaining current fractions for the indicated channels. Bars and error bars indicate the mean ± SEM (n ≥ 3).

cardiac muscles respectively; and hH_V1 (Fig. 15H), a voltage-gated proton channel. We found that, except K_V1.1, none of the ion channels tested (Fig. 15A-I) were inhibited by Cm28 at 150nM concentration. This concentration is more than150-fold higher than the K_d for K_V1.2 and more than 100-fold higher than the K_d for K_V1.3. Cm28 caused ~27% reduction in K_V1.1

current at 150nM concentration and the average RCF value was 0.73 ± 0.03 (n = 3). The estimated K_d value for $K_V1.1$ from a single concentration, based on a bimolecular interaction, yielded ~0.4 µM. Due to the limited availability of native peptide construction of a complete dose-response curve at this peptide concentration range was not possible.

5.1.4 Cm28 peptide does not compromise cell viability but suppresses the expression of activation markers in CD4$^+$ T_{EM} cells

To investigate whether the pharmacological properties of this unique Cm28 peptide are reflected in biological functional studies, we evaluated the effect of Cm28 on the TCR-mediated activation of CD4$^+$ T_{EM} cells. Before performing the T cell activation assay, we first had to determine whether the Cm28 compromises cell viability. After 24 h treatment with 1.5 µM Cm28 or 50 nM rMgTx, the viability of CD4$^+$ T_{EM} cells were not impaired either in quiescent or TCR-activated cells as analyzed by two different assays (Fig. 16). Fixable viability dye Zombie NIR identified in flow cytometric analysis that ≥90% cells were viable in the presence of either toxin. 30% dimethyl sulfoxide (DMSO) was added to the cells for 30 min as positive control for dead cells (Fig. 16A). In parallel, we found that in lactate dehydrogenase (LDH) activity assay the cytotoxicity of Cm28 was <1% and that of rMgTx was <2% for either quiescent or TCR-activated T_{EM} cells after 24 h culture period. 50 mM Sodium azide (NaN_3), as positive control, showed 15% cytotoxicity (Fig. 16B).

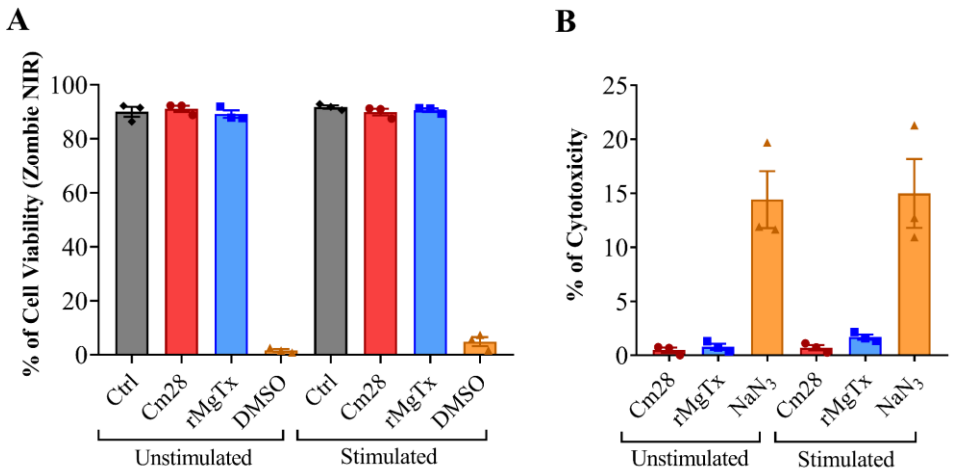

Figure 16: **Cm28 does not compromise the cell viability of either quiescent or stimulated CD4$^+$ T_{EM} lymphocytes. (A)** Cell viability of cells treated with 1.5 µM Cm28 or 50 nM rMgTx for 24 h was assessed by staining the cells with fixable viability Dye Zombie NIR using flowcytometry. Changes in

FSC and positive staining with the Zombie NIR were considered as indicators of dead cells (see Materials and Methods). Percentage of cell viability was calculated as: 1 − fraction of Zombie NIR positive cells. Cells treated with 30% DMSO for 30 min before staining were used as a positive control for dead cells. Control cells (Ctrl) were not exposed to peptides. **(B)** The cytotoxic effect of 1.5 µM Cm28 or 50 nM rMgTx on T_{EM} cells after 24 h of treatment determined using the lactate dehydrogenase (LDH) cytotoxicity assay. LDH activity of the medium was determined, and percentage of cytotoxicity was calculated (see Materials and Methods for details). For positive control, 50 mM Sodium Azide (NaN_3) was added to the cells. **(A, B)** Data from three independent experiments (two technical repeats in each) are shown as mean ± SEM.

TCR-mediated activation of human T lymphocytes leads to the up-regulation of Ca^{2+}-dependent early activation markers such as IL2R and CD40 ligand. These activation markers have been widely used as a readout to assess the $K_V1.3$-dependence of T cell activation [201, 202, 205]. $CD4^+$ T_{EM} cells were pre-incubated for 30 min with either 1.5 µM Cm28 (>1000× concentration of its K_d for $K_V1.3$) or 5 nM rMgTx (100× concentration of its K_d for $K_V1.3$, as positive control) and cells were then activated for 24 h with plate-bound anti-human CD3 antibody in the continuous presence of toxins. The flow cytometric overlayed histograms in Fig. 17 A and C show that Cm28 (red traces) significantly reduced the fraction of CD40L (Fig. 17A) and IL2R (Fig. 17C) expressing T_{EM} cells, like rMgTx (blue trace), as compared to the control cells stimulated identically in the absence of toxin (green trace). The expression of CD40L (Fig. 17B) and IL2R (Fig. 17D) in Cm28 treated T cells, normalized to that of stimulated but not treated cells, is reduced to ~47% and ~55% respectively. Similarly, positive control rMgTx decreased the CD40L and IL2R expression level to ~51% and ~48%, respectively. There was no change in expression of CD40L or IL2R in unstimulated $CD4^+$ T_{EM} cells regardless of the presence (US+Cm28) or absence of Cm28 (US) (Fig. 17).

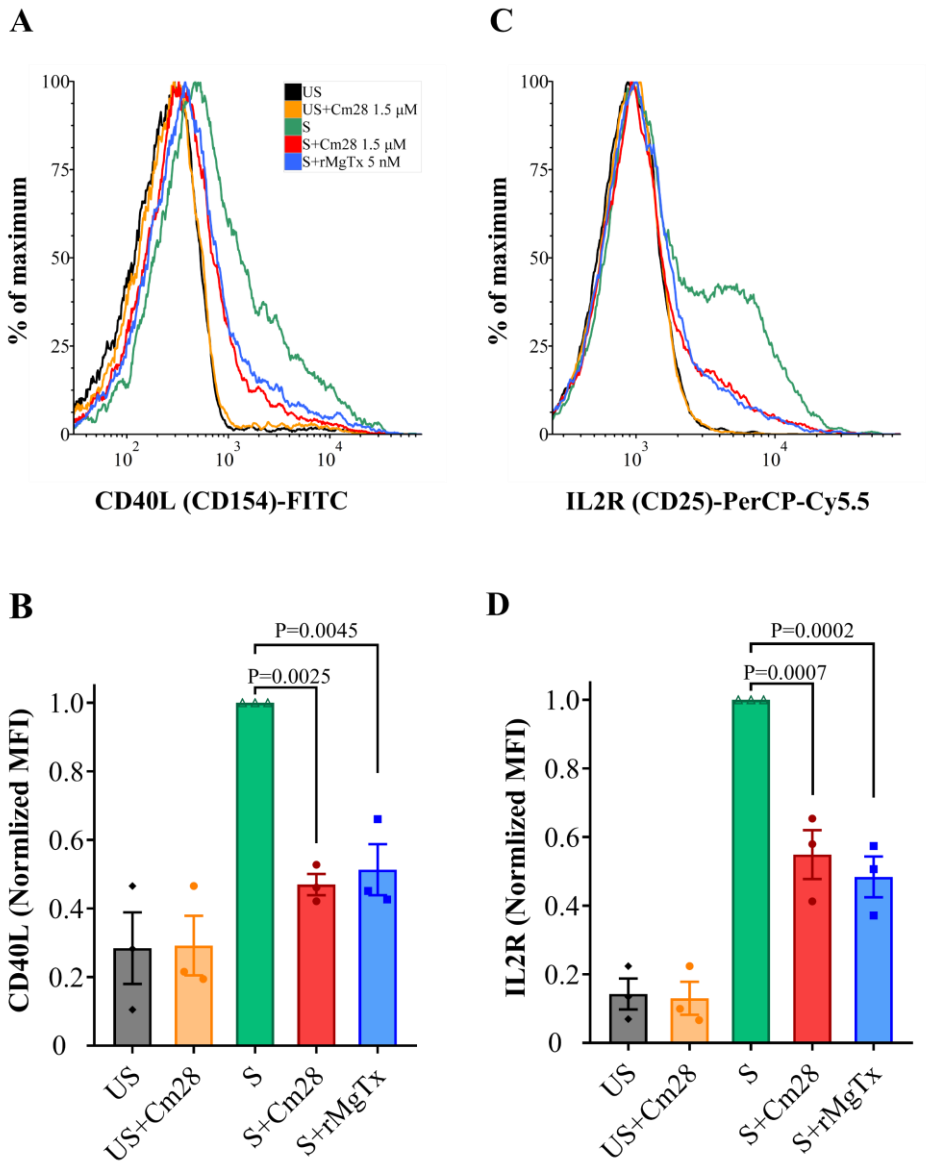

Figure 17: **K_V1.3 blockade by Cm28 inhibits the expression of CD40L and IL2R**. Isolated $CD4^+$ T_{EM} lymphocytes were stimulated for 24 h through TCR with plate-bound anti-human CD3 antibody in the presence or absence of toxins and labelled with anti-CD154 (CD40L) **(A, B)** and anti-CD25 (IL2R) antibodies **(C, D)**. Treatment labels: **US**; unstimulated (black), **US+Cm28**; unstimulated in the presence of Cm28 (1.5 µM, orange) **S**; stimulated with anti-human CD3 antibody coated wells (1µg/well, green), **S+Cm28**; stimulated in the presence of Cm28 (1.5 µM, red), **S+rMgTx**; stimulated in the presence of rMgTx (5nM, blue). **(A, C)** Fluorescence histograms were obtained from T lymphocytes gated on FSC vs. SSC density plot (10,000 events were recorded) and then, peak-normalized overlay histograms were plotted. **A**-**D** follow the same color code. **(B, D)** Mean fluorescence intensities (MFI) were determined from the histograms and normalized to that of their stimulated but not treated control (S). Bars with individual data points represent values from 3 independent experiments (two technical repeats in each). Error bars indicate SEM. Statistically significant change in expression level of CD40L and IL2R is indicated with P values (all pairwise multiple comparison with Tukey's test).

5.2 Characterization of a fluorescent peptide toxin as a probe for $K_V1.3$

HsTX1 is a peptide toxin consisting of 34 amino acid residues with amidation of the C-terminus, originating from the venom of the scorpion *Heterometrus spiniferion*. It bears potent activity against $K_V1.3$ as well as $K_V1.1$ with K_d of 12 pM and 7 nM, respectively [155]. An engineered analogue HsTX1[R14A] was developed by substituting the Arg14 with Ala which showed improved selectivity for $K_V1.3$ over $K_V1.1$ (>2000-fold) while retaining high affinity for $K_V1.3$ (K_d = 41 pM) [166]. In collaboration with Prof. Raymond S. Norton' laboratory, Monash University, Australia, we created a fluorescent analogue of HsTX1[R14A]. Cyanine dye Cy5 was conjugated to the N-terminus of chemically synthesized HsTX1[R14A] as the N-terminus does not take part in the interaction with the channel and thus its modification is likely to have less effects on $K_V1.3$ binding. This has also been demonstrated by Naseem *et al.* that His-tagged rMgTx at its N-terminus retained the affinity for $K_V1.3$ comparable to native version [202]. The ^{1}H nuclear magnetic resonance (NMR) studies confirmed the correct folding of the Cy5 labelled peptide toxin. The fluorescence absorption and emission spectra of Cy5-HsTX1[R14A] show an excitation maximum at 650 nm and an emission maximum at 666 nm. These spectral properties were identical to those measured for Cy5 under same conditions indicating that peptide conjugation did not affect the Cy5 excitation/ emission spectra. The chemical synthesis and structural and spectral properties were performed in Norton's laboratory [206]. This section describes the electrophysiological characterization of Cy5-HsTX1[R14A] and demonstrates its ability to detect $K_V1.3$ expression using flow cytometry.

5.2.1 Biophysical characterization of Cy5-HsTX1[R14A]

Although it has been previously known that HsTX1[R14A] holds a great selectivity for $K_V1.3$ over many other physiologically important ion channels, small modification in the peptide, core or N- /C- terminus conjugation may change the selectivity profile of the modified peptide [167, 175, 207]. Therefore, patch-clamp electrophysiology was conducted to confirm the retained affinity and selectivity for $K_V1.3$ of Cy5-HsTX1[R14A]. We found that Cy5-HsTX1[R14A] inhibits $K_V1.3$ with K_d = 853 pM which is ~20 times larger than K_d (41 pM) for HsTX1[R14A], however it is still in picomolar range (Fig. 18). Further, we experimentally determined the selectivity profile of Cy5-HsTX1[R14A]. We investigated its effect on four other members of K_V1 family, $hK_V1.2$, $hK_V1.4$, $hK_V1.5$ and $hK_V1.6$ (Fig. 19A−D), which are close relative to $K_V1.3$.We also tested the effect of Cy5-HsTX1[R14A] on $mK_{Ca}1.1$ (BK, MaxiK), the large conductance voltage- and Ca^{2+}-activated channel, and $hK_{Ca}3.1$ ($IK_{Ca}1$, SK4),

the Ca^{2+}-activated K^+ channel expresses in T lymphocytes (Fig. 19E−F). Cy5-HsTX1[R14A] did not inhibit any of these ion channels tested (Fig. 19A−G) at 100 nM concentration, which is about 100-fold larger than the K_d for $K_V1.3$.

When $K_V1.3$ subunit is co-expressed with other $K_V1.x$ subunits, heterotetramers can be formed with various stoichiometries and intermediate characteristics regarding the biophysical and pharmacological properties [57, 208]. As described earlier, hyperactivated disease-relevant immune cells such as microglia and macrophages express $K_V1.3/K_V1.5$ heterotetramers [23, 209]. HsTX1[R14A] binds selectively to $K_V1.3$ homotetramers however, its affinity for heterotetramers has not been investigated previously. The ability of a probe to distinguish between homo- and heterotetrameric assembly of $K_V1.3$ channels would be highly beneficial.

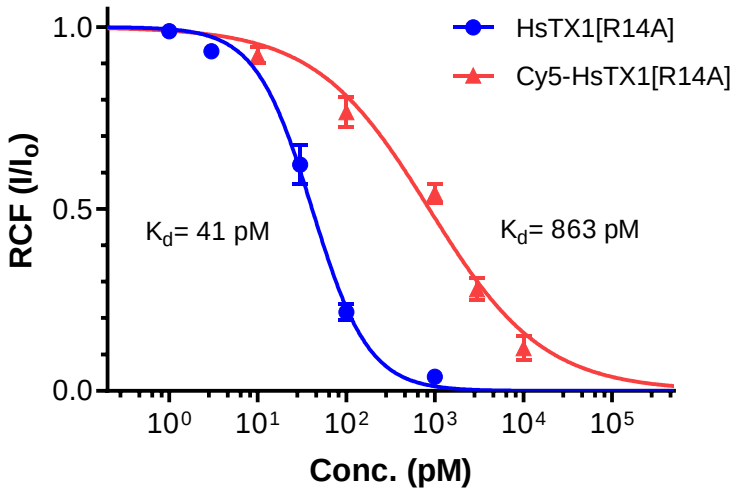

Figure 18: **Dose-dependent effect of HsTX1[R14A] and Cy5-HsTX1[R14A] on $K_V1.3$ in activated human T lymphocytes**. RCF values at various concentrations of peptides were determined and fitted with Hill equation (Eq. 1), resulting in K_d = 41 pM and H = 1.3 for HsTX1[R14A] (blue) and K_d = 853 pM and H = 0.6 for Cy5-HsTX1[R14A] (red). Error bars indicate SEM and $n \geq 3$.

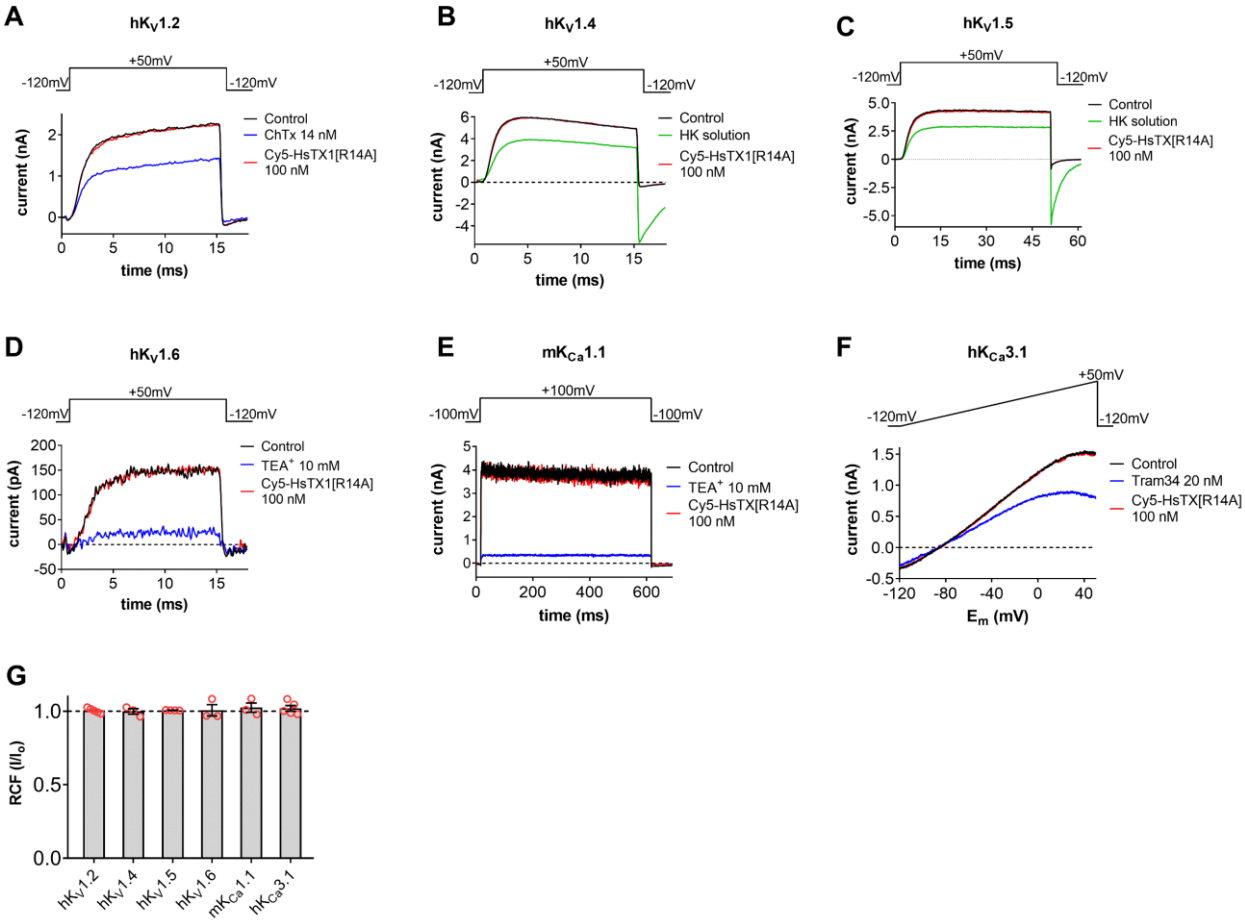

Figure 19: **Selectivity profile of Cy5-HsTX1[R14A]. (A-F)** Representative current traces in the absence (control, black) and presence (red) of 100 nM of Cy5-HsTX1[R14A]. The appropriate operation of solution exchange in the bath chamber was confirmed frequently using fully reversible blockers (blue) or solutions (green) as positive control (HK: HK-150 solution with 150 mM extracellular K^+ to decrease the K^+ driving force. TEA^+: tetraethylammonium chloride, ChTx: charybdotoxin, and Tram34 are known inhibitors of the relevant channels). The voltage sequences are given above the current traces in each panel. The traces shown for 100 nM Cy5-HsTX1[R14A] were recorded 3–5 min after application of the peptide. **(G)** Normalized RCF (I/I_0) values were calculated as the ratio of the peak currents in the absence (I_0) or presence (I) of 100 nM Cy5-HsTX1[R14A] after 10–20 repeated depolarization pulses. Symbols (empty circles in red) indicate individual values, bars heights and error bars indicate the mean ± SEM (n = 3–5).

We directly tested the affinity of Cy5-HsTX1[R14A] for K_V1.3-K_V1.5 homotetramers using tandemly linked dimers of K_V1.3-K_V1.5. To confirm the suitability of the tandem dimers we first generated K_V1.3-K_V1.3 tandem dimers and confirmed that the biophysical hallmarks of K_V1.3 were remained unchanged upon channel assembly from the dimers, *i.e.*, inactivation

kinetics of the current during long depolarization pulses, and the affinity for the small inorganic blocker TEA^+ and the peptide blocker Cy5-HsTX1[R14A] were similar to those values obtained for channels composed of $K_V1.3$ monomers. Fig. 20A shows a $K_V1.3$ current measured in a CHO cell expressing tandem dimer $K_V1.3/K_V1.3$ constructs. The current inactivates with single exponential decay kinetics with the characteristic time constant for this decay of 170 ± 25 ms (n = 5, Fig. 20A), similar to the reported inactivation kinetics of $K_V1.3$ composed of four monomers (~150−200 ms) [57, 208]. Cy5-HsTX1[R14A] at 1 nM concentration inhibited ~50 % of the current (Fig. 20D), the RCF value was 0.56 ± 0.02 (n = 4, Fig. 20F), consistent with the K_d for the monomeric assembly of $K_V1.3$ (853 pM). Similar results were obtained for the TEA^+ affinity on $K_V1.3$ assembled from dimers where a ~50% current inhibition was found at 10 mM extracellular TEA^+ concertation, consistent with the data on $K_V1.3$ assembled from monomers (Fig. 20G, I). These results confirm the proper biophysical and pharmacological properties of channels assembled from tandemly linked $K_V1.3$ dimers.

Upon confirming the suitability of the tandem dimer $K_V1.3$ constructs for pharmacology, we expressed $K_V1.3$-$K_V1.5$ tandem dimers and determined the inactivation kinetics of the current which can be used as an indicator of the heteromeric assembly of the channels [57, 209]. Fig. 20B shows a typical outside-out patch current recorded in a CHO cell transfected with the $K_V1.3$-$K_V1.5$ tandem dimer construct. The inactivation kinetics of the current were well-fit using a single exponential function with a time constant (τ_{in}) of 561 ± 42 ms (n = 6, Fig. 20B), which are significantly slower than the inactivation kinetics of $K_V1.3$. This is consistent with the formation of heterotetramers with 1:1 stoichiometry of $K_V1.3$-$K_V1.5$ subunits since the very slow inactivating $K_V1.5$ (inactivation time constant (τ_{in}): 4046 ± 310 ms, n = 8, Fig. 20C) and relatively quick inactivating $K_V1.3$ subunits are mixed, and the overall kinetics of inactivation is determined by the cooperative interaction between the subunits [57, 210]. Fig. 20E shows that the affinity of the heterotetramers for Cy5-HsTX1[R14A] is significantly reduced, 1 nM of the conjugated peptide blocks a negligible proportion of the current as compared to the inhibition of the $K_V1.3$-$K_V1.3$ tandem construct (Fig. 20F), the peptide concentration had to be increased to 10 nM to see current reduction. A similar effect of reduction in affinity for heterotetramers was observed in case of TEA^+ (Fig. 20H-I) The estimated K_d for the inhibition of the $K_V1.3$-$K_V1.5$ heterotetrameric current by Cy5-HsTX1[R14A] was ~18 nM (Fig. 20J).

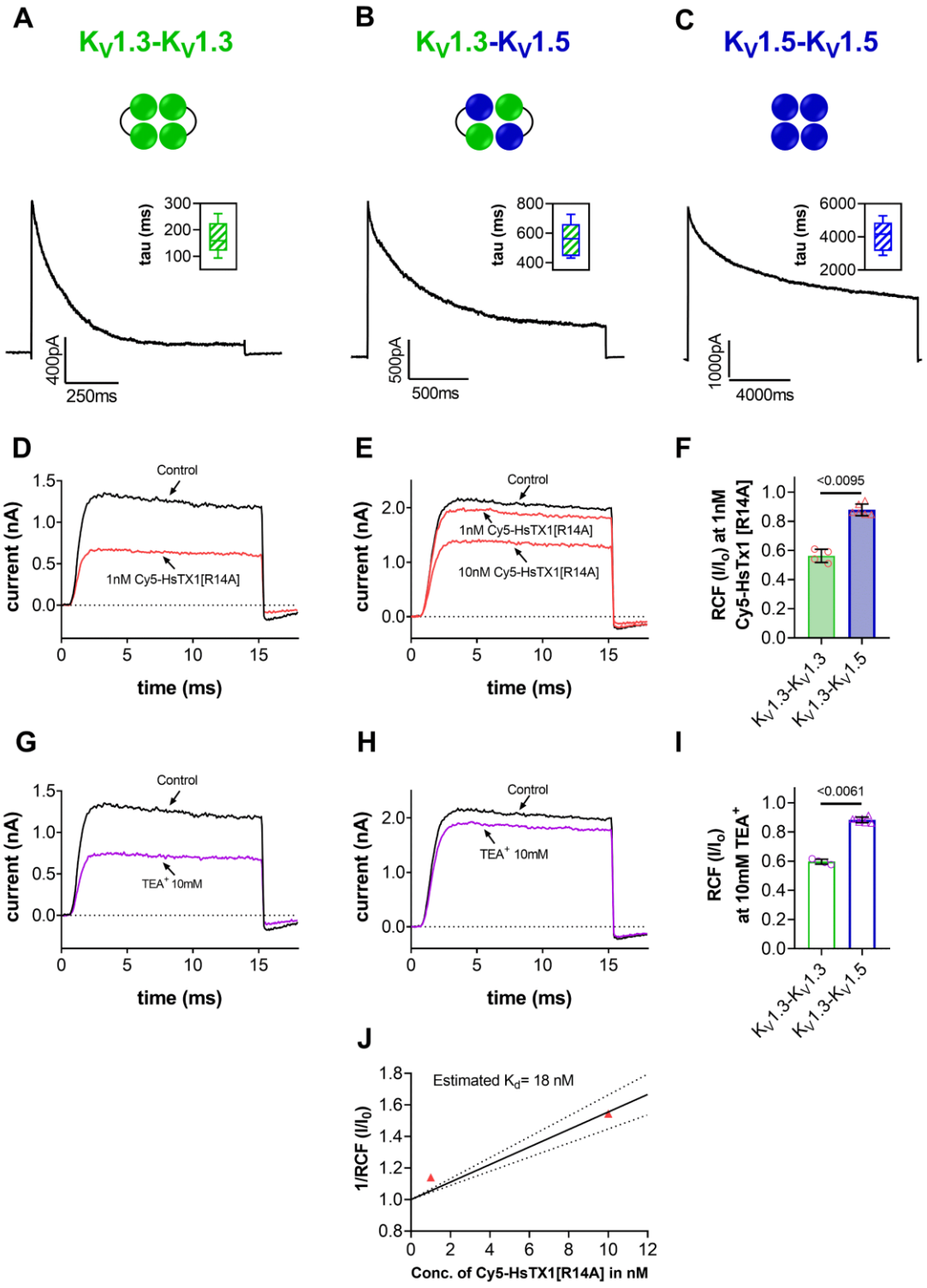

Figure 20: **Affinity of Cy5-HsTX1[R14A] for channels assembled from tandem dimers of K_V1.3/ K_V1.5.** CHO cells transfected with the K_V1.3-K_V1.3 or K_V1.3-K_V1.5 tandem dimer construct or K_V1.5 monomer construct were patched in whole-cell or outside-out patch configuration. K^+ currents were evoked by a voltage step from holding potential −120mV to +50mV for 1 s (A), 2 s (B), 20 s (C) or for 15 ms (D, E, G and H). **(A-C)** Current traces recorded in the presence of control solution for the

constructs represented in pictograms above the traces; green and blue spheres are $K_V1.3$ and $K_V1.5$ subunits, respectively, while the black lines represent linkers. The inset show the box plot of inactivation time constants (τ_{in}) determined by fitting of a single-exponential decay function to the current trace for $K_V1.3$-$K_V1.3$ homotetramer (170 ± 25 ms n = 5), $K_V1.3$-$K_V1.5$ heterotetramers (561 ± 42 ms, n = 6) and $K_V1.5$ homotetramers (4046 ± 310 ms, n = 8). **(D, E, G and H)** K^+ current traces in the absence of (control) and upon achieving equilibrium block in the presence of 1 nM or 10 nM Cy5-HsTX1[R14A] or 10 mM TEA^+ (as indicated). **(F, I)** RCF (I/I_0) for $K_V1.3$-$K_V1.3$ homotetramers or $K_V1.3$-$K_V1.5$ heterotetramers at equilibrium block in the presence of 1 nM Cy5-HsTX1[R14A] (F) or 10 mM TEA^+ (I). **(J)** Concentration dependence of the block of $K_V1.3$-$K_V1.5$ heterotetrameric channels by Cy5-HsTX1[R14A]. K_d was estimated from the Lineweaver-Burk analysis, where 1/RCF is plotted as a function of toxin concentration and fitting a line to the data points yields an approximate K_d = 1/slope = 18 nM assuming 1:1 channel-toxin interaction. The dotes lines indicate 95% confidence interval (22.135−15.085 nM). **(A-C, F, I, J)** Error bars indicate the mean ± SEM (n = 4–6). The p-values are indicated above the bar plots.

5.2.2 Cy5-HsTX1[R14A] can be used to detect $K_V1.3$-expressing cells in flow cytometry

We also determined whether the fluorescent toxin Cy5-HsTX1[R14A] can be used to detect the $K_V1.3$ channel expression in transfected CHO cells using flow cytometry. We stained both control CHO cells and CHO cells expressing GFP-$K_V1.3$, and the gating strategy of the optical signals is shown in Fig. 21A-D. Non-transfected live CHO cells were identified based on the FSC-SSC dot-plot (as indicated by Region of Interest (ROI) in Fig. 21A), and the fluorescence signal of the non-transfected CHO cells in the GFP channel was used to set the quadrant for the GFP negative cells (lower left quadrant in Fig. 21B). Based on the ROI and the quadrant in Fig.21 A and B the GFP-$K_V1.3$ expressing live CHO cells were identified in Fig. 21D. The fluorescence histograms of unstained, non-transfected CHO cells and non-transfected CHO cells stained with 10 nM Cy5-HsTX1[R14A] overlap completely (Fig. 21F), indicating that staining with Cy5-HsTX1[R14A] at the applied concentration does not bind to the CHO cells nonspecifically in the absence of $K_V1.3$ expression. When CHO cells expressing GFP-$K_V1.3$ were stained with Cy5-HsTX1[R14A], a significant population of the cells showed increased fluorescence in the Cy5 channel. This cell population is represented by the right-shifted peak in the histogram at fluorescence intensities corresponding to ~10-fold to ~100-fold over the non-labelled cells (Fig. 21F). The flow cytometric dot-plot in Fig. 21E shows that most cells that have high $K_V1.3$ expression, *i.e.*, high GFP signal, also show strong fluorescence in

the Cy5 channel. Overall, about ~40% of the cells showed increased Cy5-HsTX1[R14A] signal (sum of upper quadrants), which corresponds to ~80% of the cells that display increased GFP signal as well (upper right quadrant over the sum of the right quadrants, Fig. 21E). The specificity of K_V1.3 labelling by Cy5-HsTX1[R14A] was also confirmed using a competition assay. In this experiment, GFP-K_V1.3 expressing CHO cells were incubated first with either excess unconjugated HsTX1[R14A] (Fig. 21F) or excess recombinant margatoxin (rMgTx) (Fig. 21H) and were subsequently stained with Cy5-HsTX1[R14A]. As the profiles in Fig. 21G-H clearly demonstrate, pre-incubation of the cells with excess unconjugated pore-blocking toxins resulted in histograms that were superimposable to the control, unstained CHO population. This indicates that excess unconjugated HsTX1[R14A] or rMgTx completely inhibited labelling of the K_V1.3 channels with Cy5-HsTX1[R14A].

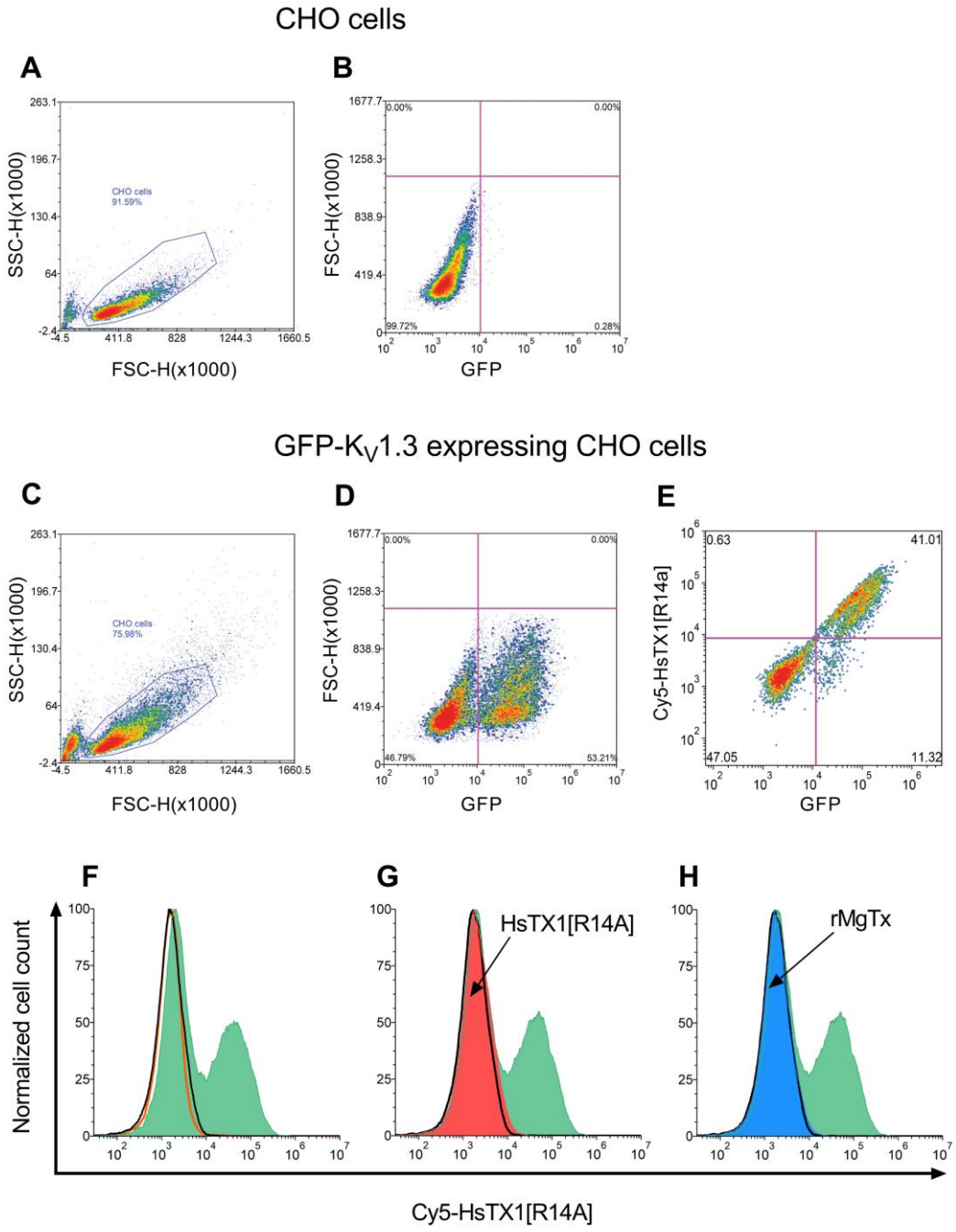

Figure 21: **Cy5-HsTX1[R14A] labelling detects heterologously expressed K_V1.3 channels in flow cytometry. (A-D)** Flow cytometric dot-plots showing the gating of CHO cells lacking K_V1.3 (A, B) or stably expressing GFP-K_V1.3 (C, D) based on their FSC (forward scatter height) vs SSC (side scatter height) parameters (A, D) and FSC vs GFP dot-plot showing the GFP positive (K_V1.3 expressing) cell population (C, D). **€** Representative flow cytometry dot plot of CHO cells stably expressing GFP-K_V1.3 and stained with Cy5-HsTX1[R14A], showing correlation of the GFP (K_V1.3) expression levels and the Cy5 signal. **(A-E)** Values indicate the percentage of the cell population in the corresponding quadrants. **(F-H)** Flow cytometry profiles of unstained (black line) or stained with 10 nM Cy5-HsTX1[R14A] (green shaded) CHO cells stably expressing GFP-K_V1.3 and control CHO cells stained with 10 nM Cy5-

HsTX1[R14A] (orange line). For Competition of label-free toxins and Cy5-HsTX1[R14A], GFP-K_V1.3 expressing CHO cells preincubated with 100 nM HsTX1[R14A] (red shaded in panel G) or 1 µM rMgTx (blue shaded in panel H) prior to staining with 10 nM Cy5-HsTX1[R14A].

5.3 Optimization of recombinant production of margatoxin and the functional characterization of the tagged and untagged versions of the peptide

5.3.1 Generation of rMgTx expressing *P. pastoris* X-33 clones and selection for hyper-resistant clone against Zeocin

The MgTx expression cassette, as illustrated in Fig. 10B, was synthesized following codon optimization for *P. pastoris* and cloned downstream to α-factor secretion signal under the control of *AOX1* promoter in pPICZαA expression vector (Fig. 10A). The TrMgTx-pPICZαA plasmid was linearized using *Sac*I enzyme and transformed into *Pichia* X-33 competent cells. After 3 days of incubation at 30 °C, >40 colonies showed prominent growth on YPD agar plate containing 100 µg/ml of Zeocin as antibiotic selection. According to Nordén *et al.* increased resistance against Zeocin directly correlates with higher expression of heterologous protein in *P. pastoris* [193]. The initially chosen colonies were grown under gradually increasing Zeocin concentrations 0.5, 1 and 2 mg/ml in YPD agar media. Most of the clones exhibited strong resistance against antibiotic selection *i.e.*, 0.5 and 1 mg/ml of Zeocin, however, comparatively few *Pichia* clones showed prominent growth at 2 mg/ml of Zeocin as evident from the growth after 2 days (Fig. 22) and presumably these clones have high copy

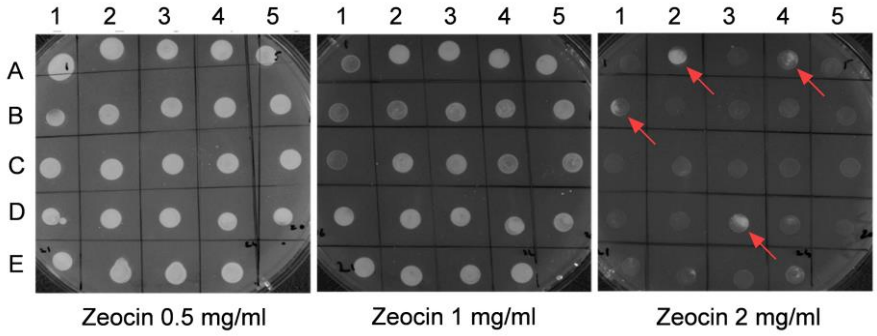

Figure 22: **Growth of *Pichia pastoris* X-33 clones on different concentrations of Zeocin.** Selected *Pichia* transformants after transformation were allowed to grow for 2 days on YPD agar medium supplemented with gradually increasing Zeocin concentration (0.5, 1 and 2 mg/ml). Red arrows indicate the clones survived at the highest concentration of Zeocin.

number of expression cassettes incorporated in the genome. The clones, survived at highest concentration of Zeocin (2 mg/ml), were subjected to colony PCR which confirmed the integration of TrMgTx-pPICZαA cassette by single crossover at 5′ *AOX1* locus of *P. pastoris* genome.

5.3.2 Overexpression of TrMgTx as a function of culturing time, MeOH induction and pH of the medium

For expression analysis, supernatant samples were collected from the cultures every 24 h post-MeOH induction for 5 days and 16% tricine SDS-PAGE was performed. A peptide band of ~6.5 kDa MW was detectable in the sample collected 24 h post-MeOH induction. The intensity of this band increased gradually to maximum after 72 h of induction, however, then it declined on the 4^{th} and 5^{th} day following induction (Fig. 23A-B). The molecular mass of the TrMgTx estimated from gel was slightly higher than the theoretical mass (~5.9 kDa) most likely because of its higher isoelectric point (pI) which is 9.10. The maximum concentration of peptide in supernatant was 78 ± 7 mg/L after 72 h of induction which was significantly higher than any other time point with $P < 0.05$ in pairwise multiple comparison (Tukey's test).

To optimize the MeOH concentration for induction, biomass *Pichia* clone was induced with 0.5, 1 and 1.5% MeOH in a medium of pH 6. The gel scanning assay revealed that the highest concentration of TrMgTx was in the supernatant sample induced with 0.5% MeOH for 72 h (71 ± 13 mg/L) and it was substantially higher than other two samples induced with 1 and 1.5% MeOH as shown in Fig. 23C. Similarly, to find the suitable pH of the medium for improved expression of the peptide, biomass was induced with 0.5% MeOH in media having pH 5, pH 6, pH 7 or "not adjusted" for 72 h. The supernatant sample taken from the culture at pH 6 showed 76 ± 8 mg/L expression of TrMgTx which is greatly higher than other samples from cultures with pH 5 or pH 7 or "not adjusted" as shown in Fig. 23D.

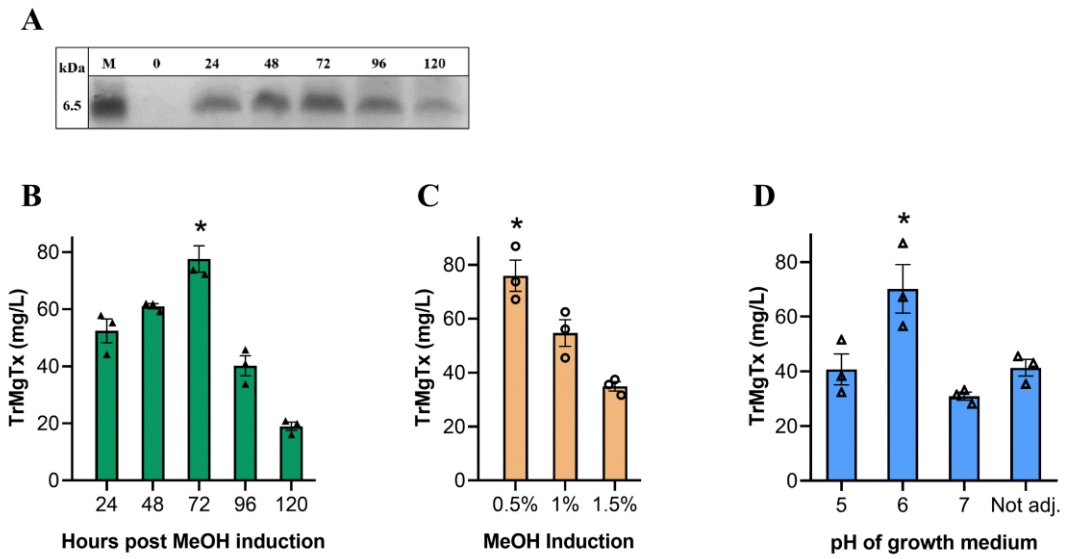

Figure 23: **Optimization of TrMgTx expression in shake-flask fermentation.** (**A**) 15 µl of supernatant samples from indicated time points were analyzed by 16% tricine SDS-PAGE (stained with R-250 CBB). Protein band at ~6.5 kDa in samples from 24 to 120 h represents the TrMgTx. (**B-D**) The amount of TrMgTx in different supernatant samples was quantified comparing the gel band intensity with that of standards using Image Lab software (Bio-Rad). (**B**) TrMgTx expression was induced by 0.5% MeOH at pH = 6.0 of the media. **(C)** Secretion of TrMgTx in culture (at pH 6) induced with different MeOH concentrations for 72 h. **(D)** Level of TrMgTx expression when induced with 0.5% MeOH for 72 h at the indicated pH values of the medium. Label "Not adj." means unbuffered medium. **(B-D)** Data represent the individual values (filled triangles in B, empty circles in C and empty triangles in D), bar heights indicate mean of three independent experiments where error bars are SEM. Asterisks indicate significant difference in all pairwise multiple comparison (Tukey's test), *P <0.05.

5.3.3 Purification of TrMgTx

The best *Pichia* X-33 clone in trial expression study was subjected to large-scale shake-flask fermentation under optimized conditions as described above (72 h, pH 6 and 0.5% MeOH) and secreted TrMgTx was purified to homogeneity by two-step purification strategy (Table 8). His-tagged MgTx was efficiently captured using His-trap column packed with Ni^{2+} Sepharose and eluted with imidazole (Fig. 24A). The tricine SDS-PAGE analysis of fraction from affinity chromatography showed a clear and dense band of TrMgTx around 6.5 kDa in imidazole eluates, however no such band was observed in the fractions collected during loading the supernatant (flow through) and washing of the column (Fig. 24B) demonstrating that resin has efficiently captured all His-tagged peptides from cultured supernatant. The moderately purified TrMgTx was further purified by RP-HPLC using C_{18} semi-preparative column (Fig. 24C).

Analysis of the HPLC fractions by Tricine SDS-PAGE revealed the fraction corresponding to the peak eluted at about 28 min retention time (R_T), indicated as peak 2 in the chromatogram of Fig. 24C, contained TrMgTx (Fig. 24D). To confirm the MW of the product ESI-QTOF-MS analysis was performed in our collaborator's laboratory (Prof. Attila Gáspár, Faculty of Sciences, University of Debrecen). The determined average molecular mass of TrMgTx 5980.86 Da was in full agreement with the theoretical average mass of 5980.96 Da.

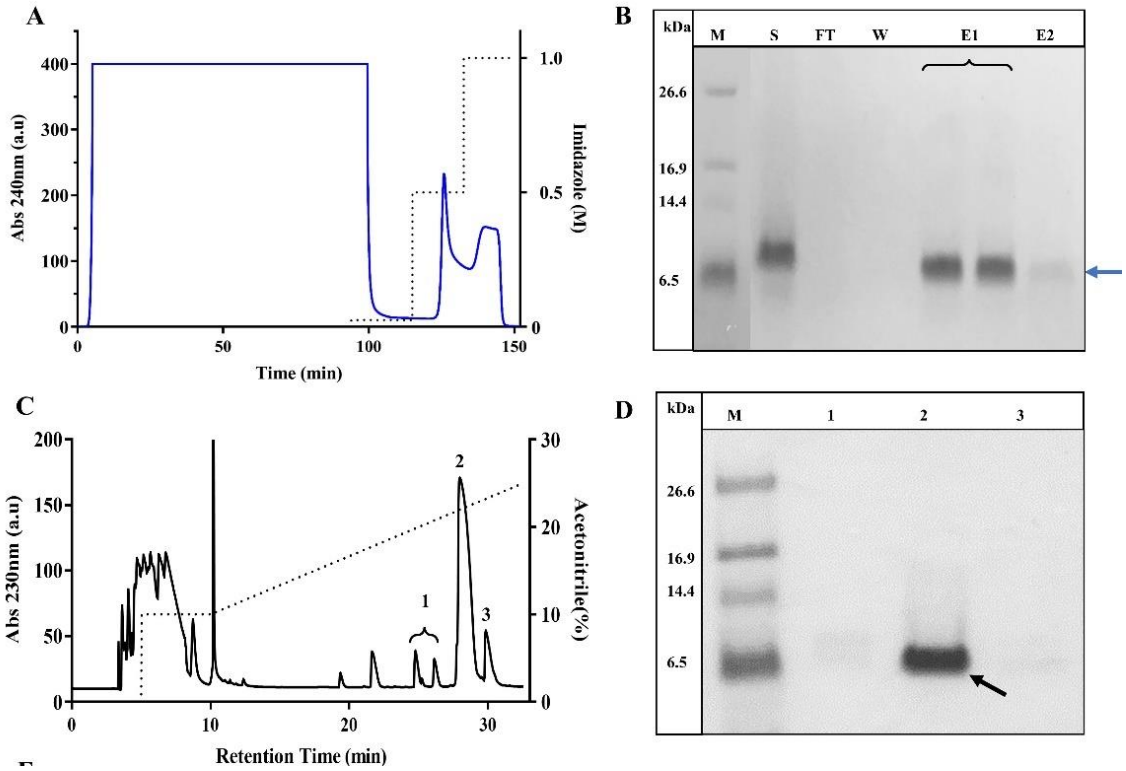

Figure 24: **Purification of TrMgTx (A)** The chromatogram shows the purification of culture supernatant (cultured for 72 h, pH 6, induced with 0.5% MeOH) by Ni^{2+} affinity column. Absorbance was measured at 240 nm (indicated with blue line, left axis) and dotted line denotes the concentration of imidazole in elution buffer (right axis). **(B)** 16% Tricine SDS-PAGE illustrates the analysis of fractions collected from Ni^{2+} affinity chromatography. **M**: low molecular weight (LMW) protein marker, **S**: raw (unpurified) supernatant, **FT**: flow through, **W**: wash with washing buffer, **E1**: Elution with 0.5 M imidazole and **E2**: Elution with 1 M imidazole. Blue arrow indicates the 6.5 kDa band of TrMgTx. **(C)** RP-HPLC chromatogram of TrMgTx. Partially purified TrMgTx in step 1 (A-B) was applied on RP C_{18} semi-prep column and eluted with a gradient of 10-30% acetonitrile (shown with dotted line, right axis) over 30 min. Absorbance was recorded at 230 nm (left axis). Numbers indicate the peaks collected. **(D)** 16% Tricine SDS-PAGE analysis of HPLC fractions. **M**: LMW protein marker, Lane **1-3**: fractions from corresponding peaks as indicated in HPLC chromatogram (panel **C**). The black arrow indicates the presence of TrMgTx in lane 2.

Western blot analysis verified the identity of TrMgTx by detecting a single band at the expected MW with the anti-His antibody (Fig. 25A). The purity of TrMgTx was >98% after the two-step purification as assessed by C_{18} RP-HPLC analytical column (Fig. 25B). Table 8 summarizes the purification scheme; on average 9.1 mg of pure TrMgTx was produced with 43% net recovery from 250 ml of *P. pastoris* culture under optimized conditions.

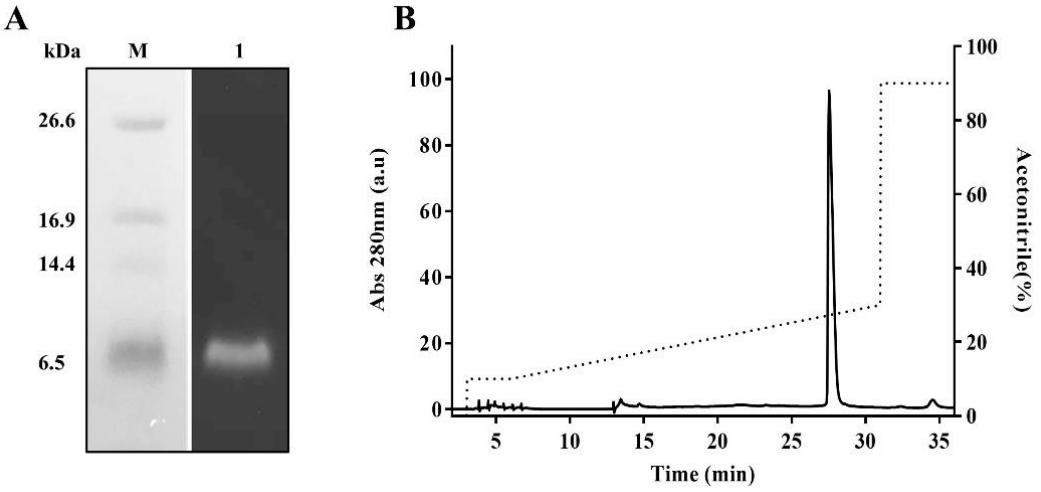

Figure 25: **Purity analysis of TrMgTx achieved by the two-step purification strategy**. **(A)** Western blot analysis of the TrMgTx sample eluted from the RP-HPLC column (Fig. 24C−D) using HRP conjugated anti-His antibodies. **Lane M**: LMW protein marker, **Lane 1**: RP-HPLC purified TrMgTx **(B)** HPLC chromatogram shows purity analysis of the TrMgTx using C_{18} analytical column. A gradient of 10-30% acetonitrile over 25 min was run for peptide elution (dotted line, right axis). The absorbance was measured at 280 nm (left axis). Single peak indicates TrMgTx. Purity was calculated as [(area under the peak of interest) / (cumulated area under all peaks) x 100] and shown in Table 8.

Table 8: **Tagged recombinant margatoxin (TrMgTx) purification scheme.**

	Purification Step	Avg. Vol. (ml)	Avg. TrMgTx Concentration (mg/ml)	Avg. total TrMgTx amount (mg)	*Avg. net Recovery (%)	Purity (%)
-	**Cultured supernatant**	246	0.085[a]	20.8	100	-
1	**Ni^{2+} affinity chromatography**	14.5	1.01[a]	14.7	70.6	-
2	**RP -HPLC**	32.6	0.279[b]	9.1	43.2	>98[c]

* Net recovery = TrMgTx acquired after a given step/ total TrMgTx in cultured supernatant

a. Gel scan analysis with Image Lab Software (see Fig. 23 caption)

b. The protein concentration was determined by using Pierce™ BCA Protein Quantification kit

c. % Purity was assessed by RP-HPLC (see Fig. 25B)

5.3.4 Recombinant MgTx with native N-terminus

N-terminus tag of 14 residues (EFHHHHHHLQIEGR) which mainly consists of 6x His and protease site was cleaved by digesting TrMgTx with factor Xa (FXa) protease. The recognition sequence of FXa is "IEGR" and FXa cleaves after Arg residue without leaving any extra residues at the N-terminus of recombinant peptide. Appearance of a protein band of ~4.1 kDa (theoretical MW of native MgTx) in overnight digested sample in tricine SDS-PAGE confirmed the successful removal of tag from TrMgTx (Fig. 26A). The liberated His-tag fragments were captured with Ni^{+} affinity beads and the untagged rMgTx (UrMgTx) was purified using C_{18} RP-HPLC column. The peak eluted at 21.6 min of R_T in the chromatogram (Fig. 26B) contained UrMgTx. The determined average mass of UrMgTx (4178.95 Da), provided by the MS analysis in Prof Gáspár's lab, is to the theoretical mass (4179.018 Da) of UrMgTx and also in full agreement with previously reported MW of native MgTx [142] indicating that there are no additional amino acid residues at either terminus of UrMgTx.

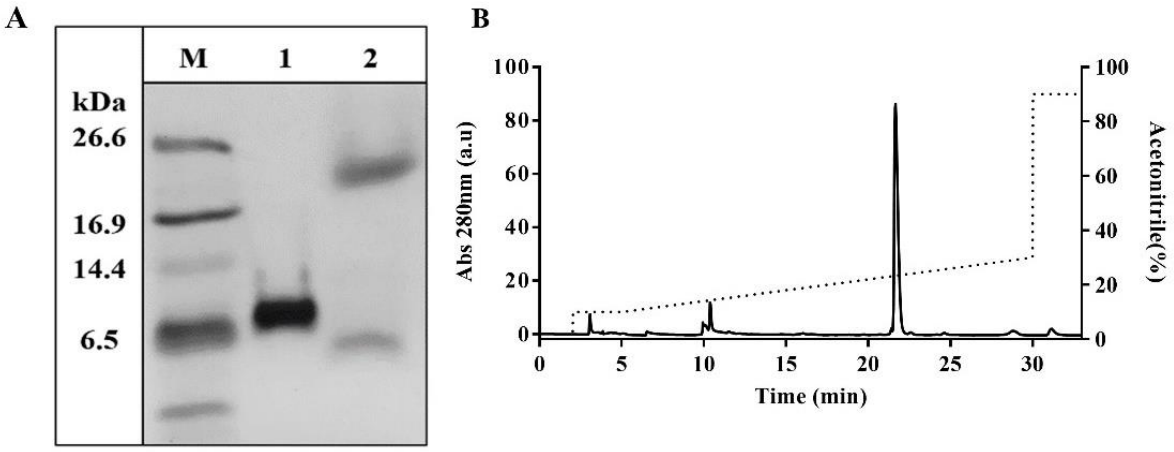

Figure 26: **Removal of tag from TrMgTx. (A)** 16% Tricine SDS-PAGE analysis of the TrMgTx samples incubated overnight at 25 °C without (lane 1) and with (lane 2) factor Xa protease (at 1:200 enzyme to peptide ratio) M: LMW protein marker. **(B)** RP-HPLC chromatogram of UrMgTx purification. The digested TrMgTx sample after removing the His-tag fragments was loaded to C_{18} column and a gradient of 10-30% acetonitrile over 25 min was run. The absorbance was measured at 280 nm (left axis) and dotted line indicates the acetonitrile gradient (right axis).

5.3.5 Effect of tagged and untagged recombinant MgTx on $K_V1.2$ and $K_V1.3$ ion channel

Since the MgTx blocks $K_V1.2$ and $K_V1.3$ channels with high potency, therefore the pharmacological activities of rMgTx analogues were tested against these two channels. The

$K_V1.2$ currents were recorded in CHO cells as described in section 5.1.1. TrMgTx and UrMgTx at 100 pM concentration inhibited ~60% and 90% of $K_V1.2$ current, respectively, as illustrated by current traces recorded in the presence and absence of respective MgTx analogues (Fig. 27A-B). The onset and relief from the steady-state block of $K_V1.2$ currents in the presence of TrMgTx or UrMgTx (indicated with colored bars) is demonstrated in Fig. 27C-D. The equilibrium block of $K_V1.2$ developed slower with TrMgTx than UrMgTx at the same concentration (100 pM). The time constants, obtained by fitting the appropriate exponential function (Eq. 3) to the normalized peak currents during the toxin wash-in procedure, were τ_{on} = 202 ± 2.3 s for TrMgTx and τ_{on} = 191 ± 12 s for UrMgTx. When cells were perfused with toxin-free solution, a slow but full recovery from the block was achieved in case of TrMgTx with τ_{off} = 532 ± 69 s (see Eq. 4 for the fitted function). However, like native MgTx, slow and partial recovery (τ_{off} = 1308 ± 351 s) from the block by UrMgTx was observed. We calculated the kinetic parameters (k_{on}, k_{off} and K_d) to reveal the impact of additional amino acid residues at N-terminus of TrMgTx on its binding to $K_V1.2$ channel considering simple bimolecular interaction between the toxin and the channel using Eqs. 5−7 and shown in Table 9 and Fig. 27F. The k_{on} for UrMgTx is slightly higher than that of TrMgTx (unpaired *t* test, n = 3−4, P <0.01), however the k_{off} rate of UrMgTx is considerably lower than that of TrMgTx (unpaired *t* test, n = 3−4, P <0.001). We also determined the dose-dependent inhibition of $K_V1.2$ by both analogues of rMgTx. RCF values at various concentrations were fitted with Hill equation (Eq. 1) and best fit resulted in K_d = 64 pM for TrMgTx and K_d = 14 pM for UrMgTx (Fig. 27E). TrMgTx exhibited ~5-fold less potency for $K_V1.2$ than the tag-free UrMgTx.

A similar set of experiments were performed for $K_V1.3$ channel. TrMgTx and UrMgTx at 200 pM concentrations inhibited ~70% and ~80% of whole-cell $K_V1.3$ currents in activated human T lymphocytes, respectively as shown by current traces in Fig. 28A-B. The change in the peak current of $K_V1.3$ upon application and wash-out of TrMgTx and UrMgTx (colored bars) is represented in Fig. 28C-D. Like $K_V1.2$, TrMgTx took more time to reach block equilibrium than UrMgTx upon application of 200 pM either toxin in bath solution (τ_{on} = 168 ± 19 s for TrMgTx and τ_{on} = 116 ± 10 s for UrMgTx were obtained, n = 4). However, unlike $K_V1.2$, the τ_{off} values were similar for both analogues of rMgTx (for TrMgTx τ_{off} = 568 ± 84 s and for UrMgTx τ_{off} = 560 ± 28 s were obtained, n = 4) with almost full recovery of initial peak current.

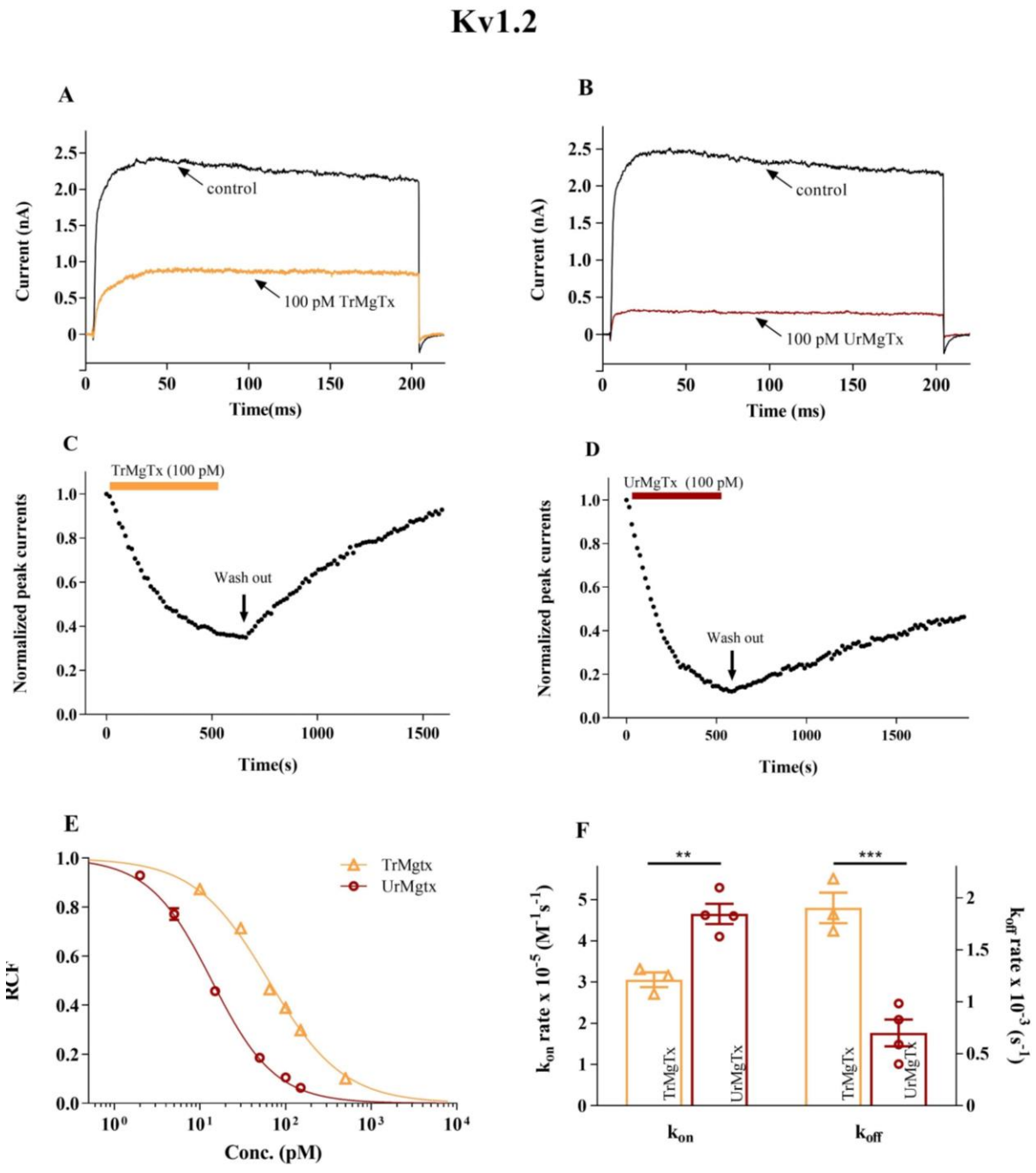

Figure 27: **Inhibition of Kv1.2 currents by TrMgTx and UrMgTx**. **(A, B)** The Kv1.2 currents were evoked from transiently transfected CHO cells either in whole-cell or outside-out patch configuration as described earlier (or for details see Materials and Methods). Representative traces show the K^+ current before the application of toxin (control) and after reaching the equilibrium block in the presence of 100 pM of TrMgTx (A) or UrMgTx (B). **(C, D)** Development of and recovery from steady-state block of Kv1.2 current at 100 pM of either TrMgTx (C, yellow bar) or UrMgTx (D, burgundy bar) is shown by plotting the normalized peak currents as function of time. Following block equilibrium, the recording chamber was perfused with toxin-free solution (arrow, wash-out) to assess reversibility of the block. **(E)**

dose-dependent block of $K_V1.2$ by analogues of rMgTx. The RCF values taken at different toxin concentrations were fitted with Hill equation (Eq. 1) The best fit yielded K_d = 14 pM for UrMgTx and K_d = 64 pM for TrMgTx. Error bars represent SEM and n = 3−5. **(F)** Comparison of block kinetics of TrMgTx and UrMgTx for $K_V1.2$. The k_{on} (left y-axis) and k_{off} (right y-axis) rates were calculated from measured time constants (τ_{on}, τ_{off}) for the onset of equilibrium block in the presence of 100 pM toxin and for the recovery from block (see panel C and D) using Eq. 9−10 and plotted on a bar graph. Symbols indicate individual data points (n = 3−4), bar heights and error bars indicate mean ± SEM. **P <0.01, ***P <0.001, ns = not significant, unpaired *t* test comparison.

Parameters of binding kinetics of both rMgTx analogues to $K_V1.3$ are given in Table 9 and plotted on bar graph (Fig. 28F). The k_{on} rate of UrMgTx is significantly higher than that of TrMgTx (P <0.001, n = 4), however the k_{off} rates of both peptides were statistically the same (P >0.05, n = 4). In the dose-response relationship the best fit of data points resulted in K_d 86pM and 50 pM for TrMgTx and UrMgTx, respectively (Fig. 28E). TrMgTx has slightly lower affinity for $K_V1.3$ than the UrMgTx.

Table 9. **Binding kinetics of rMgTx variants to $K_V1.2$ and $K_V1.3$ channels**

	Toxin	k_{on} ($M^{-1}s^{-1}$)	k_{off} (s^{-1})	K_d (pM)
$K_V1.3$	TrMgTx	2.14×10^{-5}	0.00179	83.90
	UrMgTx	3.43×10^{-5}	0.00179	52.20
$K_V1.2$	TrMgTx	3.05×10^{-5}	0.00190	62.29
	UrMgTx	4.62×10^{-5}	0.00098	15.04

The k_{on} and k_{off} were calculated (using Eq. 5 and 6) from averaged τ_{on} and τ_{off} values obtained from 3−5 independent experiments (see Materials and Methods). K_d was determined as k_{off}/k_{on}.

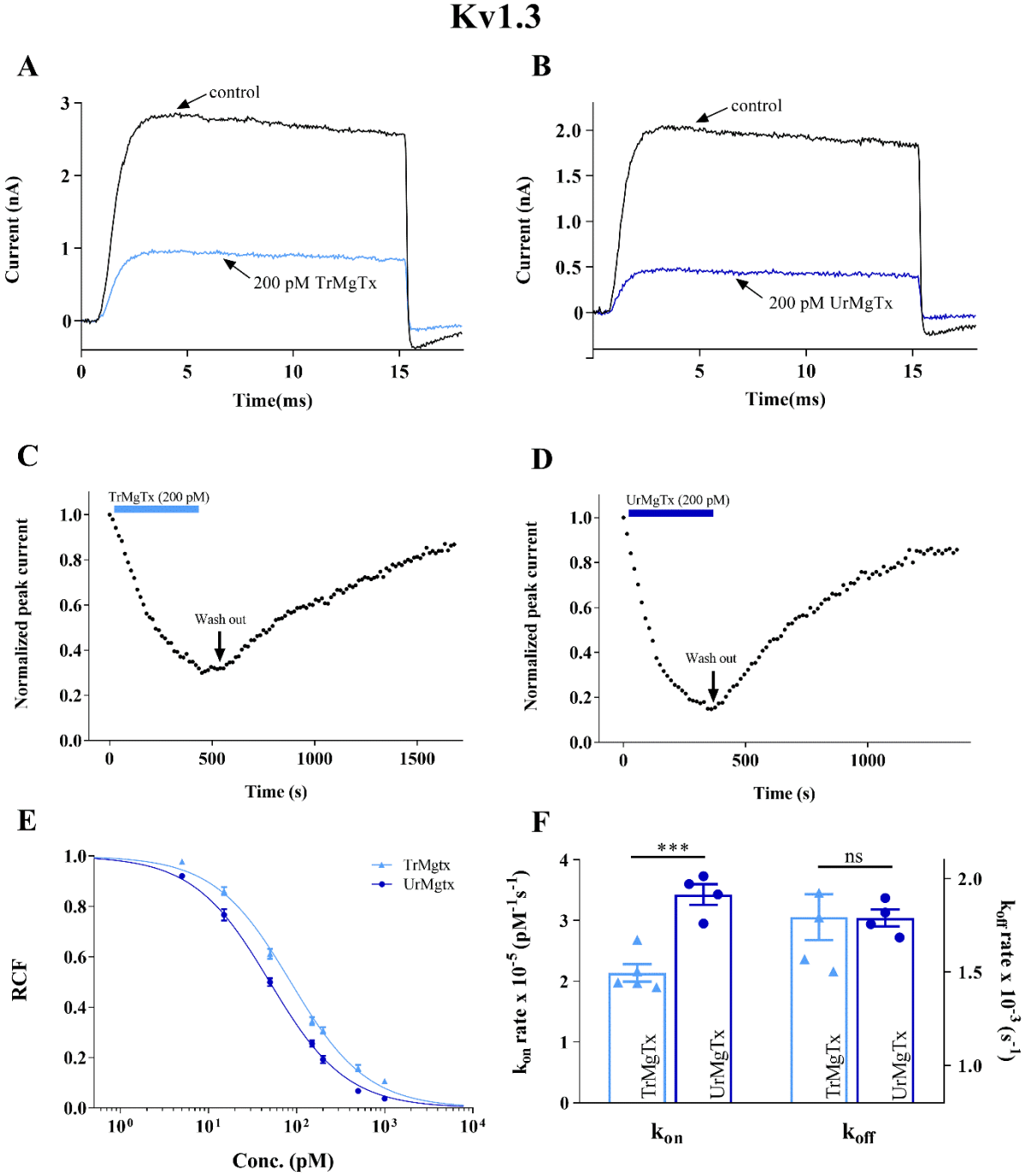

Figure 28: **Inhibition of Kv1.3 currents by TrMgTx and UrMgTx. (A, B)** Whole-cell currents through $K_V1.3$ were evoked from activated human peripheral lymphocytes by depolarization to +50 mV for 15 ms from a holding potential of −120 mV. Test pulses were applied every 15 s. Representative traces show the $K_V1.3$ currents in activated human T lymphocyte under control solution and at equilibrium block in the presence of TrMgTx (A) or UrMgTx (B) at 200 pM concentration (as indicated). **(C, D)** Development of and recovery from the steady-state block of $K_V1.3$ currents. Normalized peak currents during the application of 200 pM of TrMgTx (C, light blue bar) or UrMgTx (D, dark blue bar) and during the perfusion with toxin-free solution (arrow, wash-out) were plotted

against time. **(E)** Concentration-dependent block of $K_V1.3$ by TrMgTx or UrMgTx. The best fit to the RCF values yielded K_d = 50 pM for UrMgTx and K_d = 86 pM for TrMgTx. Error bars represent SEM and n = 3-4. **(F)** Comparison of binding kinetics of TrMgTx and UrMgTx to $K_V1.3$. k_{on} (left y-axis) and k_{off} rates (right y-axis) were calculated for the development of steady-state block with 200 pM of either toxin and for recovery procedure (panel C and D, see the details in the legend for Fig. 27F) and plotted on a bar graph. Symbols indicate individual data points (n = 4), bar heights and error bars indicate mean ± SEM. ***P <0.001, ns = not significant, unpaired *t* test.

5.3.6 $K_V1.3$ inhibition by rMgTx analogues suppresses the activation of $CD4^+$ T_{EM} cells

In order to demonstrate the biological function of the recombinant peptides we also studied the effect of TrMgTx and UrMgTx on the expression of IL2R and CD40L, early activation markers of $CD4^+$ T_{EM} cells, following the same procedure as described for Cm28 toxin (5.1.4). The presence of either TrMgTx or UrMgTx (at ~100× concentration of their respective K_d values) during the T_{EM} cell stimulation with plate-bound anti-human CD3 antibody for 24 h substantially reduced the upregulation of IL2R and CD40L expression (Fig. 29) as compared to the control cells stimulated in the same fashion but in the absence of the toxin. These findings are qualitatively demonstrated in the fluorescence histograms in Fig. 29A and C. The quantitative analysis showed that TrMgTx (8.5 nM) causes ~39% inhibition of IL2R (Fig. 29B) and ~36% of CD40L expression (Fig. 29D). Similarly, UrMgTx (5nM) hampered expression of both activation markers by ~45%. It is important to note that CD40L expression of the stimulated cells after treatment with either TrMgTx or UrMgTx was comparable to that of unstimulated cells (Fig. 29D). These results suggest that both analogues of rMgTx are biologically active and the presence of a His-tag at the N-terminus marginally reduces the efficacy of TrMgTx.

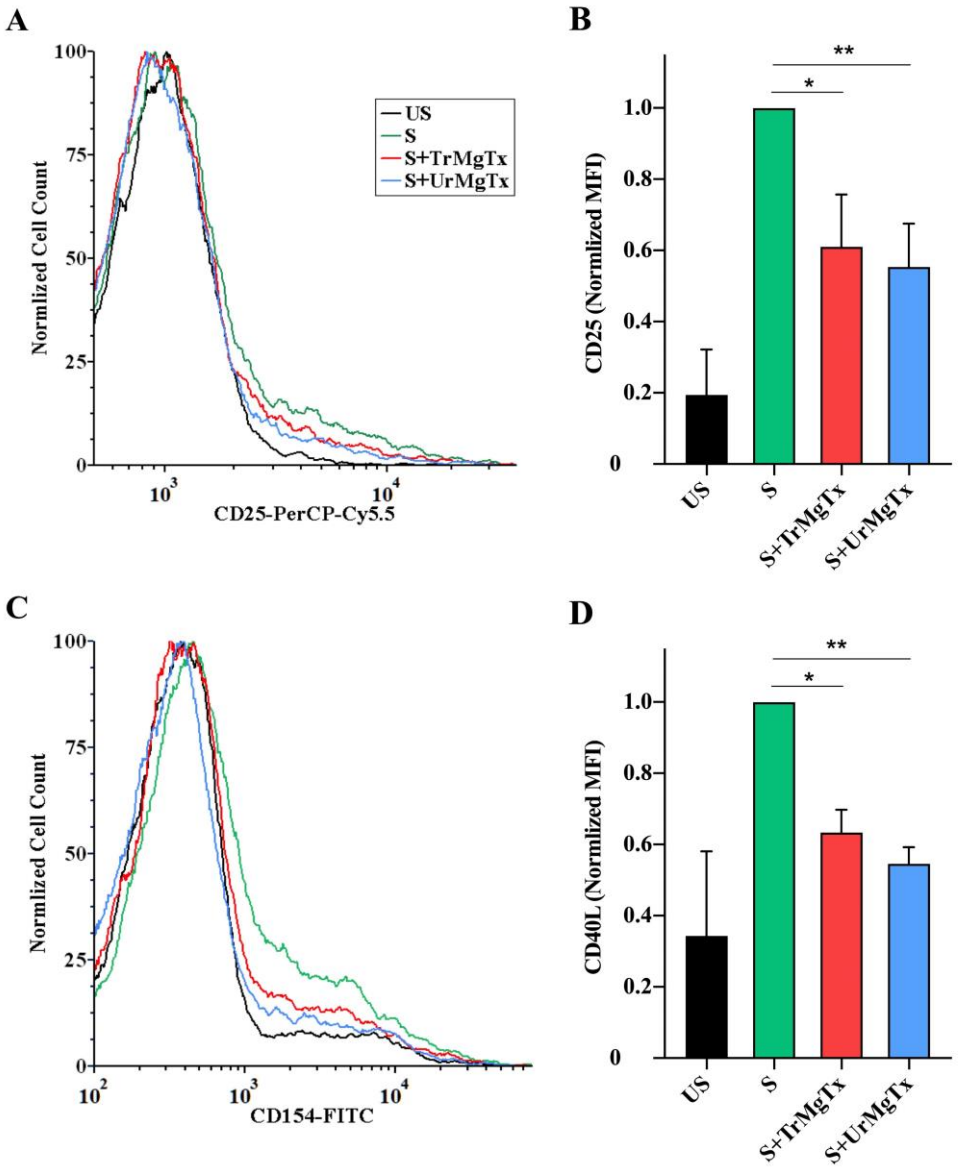

Fig 29: **rMgTx decreases the expression of IL2R and CD40L.** Isolated $CD4^+$ T_{EM} cells were stimulated for 24 h with anti-human CD3 antibody in the presence or absence of toxins and labelled with anti-CD154 (CD40L) **(A, B)** and anti-CD25 (IL2R) antibody **(C, D)**. **US**: unstimulated (black), **S**: stimulated (green), **S+ TrMgTx**: stimulated in the presence of TrMgTx (8.5 nM, red), **S+ UrMgTx**: stimulated in the presence of UrMgTx (5 nM, blue). **(A, C)** Fluorescence histograms were obtained from T lymphocytes gated based on their FSC and SSC parameters (10,000 events were recorded) and then, peak-normalized overlaid histograms were plotted for CD25 or CD154. Panel A-D has the same color code. **(B, D)** Mean fluorescence intensities (MFI) were determined from the histograms and normalized to that of their stimulated but not treated control (S). Data represent values from 3 independent experiments (two technical repeats in each) with SEM. Significant difference of IL2R and CD40L expression between the stimulated samples in the absence and presence of toxin is indicated with asterisks, (*P <0.05, **P <0.01, all pairwise multiple comparison with Tukey's test).

6. DISCUSSION

6.1 Pharmacological and functional characterization of a novel $K_V1.3$ inhibitor toxin from *C. margaritatus* scorpion

In this part of thesis, we investigated the *in vitro* pharmacological and immunological activities of Cm28, a novel peptide isolated from the scorpion *Centruroides margaritatus* of the Buthidae family. Cm28 is made up of only 27 amino acid residues including six cysteine residues. It is a high-affinity inhibitor of $K_V1.2$ and $K_V1.3$ channels with K_d values of 0.96 and 1.3 nM, respectively, and a low-affinity blocker of $K_V1.1$. Cm28 at high concentrations (~100× of K_d for $K_V1.3$) did not inhibit other ion channels examined in this work, which included four other subtypes of K^+ channels ($K_V1.5$, $K_V11.1$, $K_{Ca}1.1$, $K_{Ca}3.1$), two subtypes of Na^+ channels ($Na_V1.5$ and $Na_V1.4$) and the voltage-gated H^+ channel hH_V1. In biological assays, Cm28 (at 1.5 µM concentration, ~1000× of K_d for $K_V1.3$) markedly reduced the expression of IL2R and CD40L in activated human $CD4^+$ T_{EM} cells *in vitro* without impacting cell viability.

Cm28 has a unique primary structure, and it is quite different from all the previously known 195 peptide toxins identified in scorpion venom. The closest relatives found were members of the ε-KTx family (39-40% identity) and α-KTx subfamily 13 (29-33% identity) (Fig. 12). In phylogenetic tree analysis, Cm28 and ε-KTx family members appeared in the same clade belonging to the α-KTx family (Fig. 30). So far, only two members of the ε-KTx family are known and they exhibit an inhibitor-cystine knot (ICK) type scaffold instead of classical secondary structure [211]. Thus, evaluation of a large number of orthologs is needed to establish its phylogenetic position. The ε-KTx could be a subfamily of the α-KTx with an ICK motif. The branch support values (92 and 80) indicate that Cm28 is different than ε-KTx1.1 and ε-KTx1.2. Furthermore, the modeled structure of Cm28 has more resemblance to the classical structure of α-KTx toxins lacking the ICK scaffold. Therefore, we suggest that Cm28 is the first example of a new subfamily of α-KTxs and the proposed systematic number is α-KTx 32.1. The primary sequence of Cm28 has been deposited in Uniprot database under the accession number (C0HM22). However, a structural study is necessary to ascertain whether Cm28 has an ICK scaffold like the ε-KTxs or whether Cm28 has the characteristic scaffold of the α-KTxs.

We demonstrated that Cm28 is not a gating modifier as the voltage dependence of steady-state-activation and threshold voltage of activation of either $K_V1.2$ or $K_V1.3$ ion channel were not affected by the Cm28 (Fig. 14A−E). On the contrary, we proposed that Cm28 is a pore

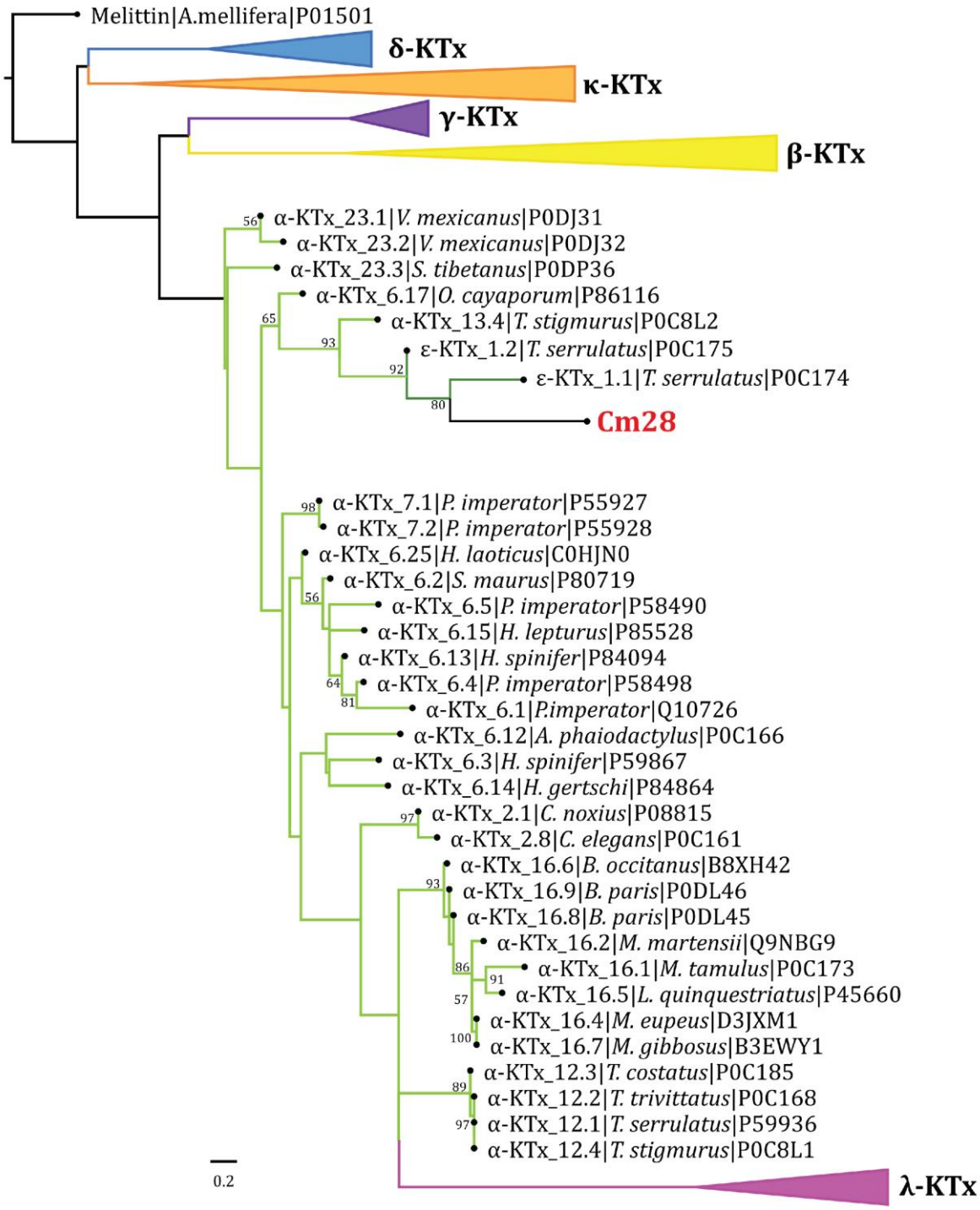

Figure 30: **Phylogenetic analysis of Cm28.** Maximum likelihood tree topology obtained from the analysis of Cm28 and other related KTxs (Log-likelihood = −4445.324618). The numbers below the nodes indicate bootstrap support values (UFBoot) > 50. The analysis was performed in Prof. Possani's lab; therefore, the methods are not detailed in this Dissertation.

blocker. It followed the blocking kinetics of a simple bimolecular interaction between channel and toxin described previously for classical pore blockers such as ChTx [66]. The apparent 1st-

order association rate showed linear correlation with toxin concentration and the dissociation rate remained insensitive to the change in Cm28 concentration (Fig. 14F). Moreover, the dissociation constants calculated by the k_{off}/k_{on} ratio (K_d = 1.15 nM for K_V1.2 and K_d = 2.15 nM for K_V1.3) are similar to those determined by fitting the Hill equation to the concentration dependence of current inhibition (K_d = 0.96 nM for K_V1.2 and K_d = 1.3 nM for K_V1.3).

The blocking mechanism of Cm28 is coherent with pore blocker toxins. However, unlike classical pore blocker peptides it lacks the typical functional dyad (Lys and Tyr) or at least the critically positioned lysine residue which protrudes into the selectivity filter of the channel [38, 66] but still it inhibits K_V1.2 and K_V1.3 with high affinity. Few other short α-KTx peptides (<30 amino acids) are known which block K_V1.3 with high affinity despite lacking the functional dyad. BmP02 (α-KTx 9.1) and BmP03 (α-KTx 9.2) toxins, for example, differ only in a single amino acid at position 16, which is Lys in BmP02 and Asn in BmP03. Both toxins block the K_V1.3 channel with IC_{50} values of 7 nM and 85.4 nM, respectively. This 12-fold decrease in potency indicate that Lys16 is involved in functional surface even though the typical dyad was missing [157]. Kbot1 (α-KTx 9.5), has 93% identity with BmP02 differing only by two amino acids (N14H, K16V). Nevertheless, Kbot1 is also a potent inhibitor of K_V1.3 (IC_{50} = 15 nM). Like BmP03, Kotb1 lacks Lys16 but has a potency closer to BmP02 toxin which can be explained by the loss of a cationic charge through the addition of a histidine residue at position 14. Kbot1 also blocks the ChTx binding in the rat brain synaptosomes with an IC_{50} of 10 nM [157, 212]. A short peptide Tt28 from another α-KTx 20 subfamily also lacks typical dyad motif but still inhibits K_V1.3 current with high affinity (IC_{50} = 7.9 nM), although it has only 25% similarity with BmP02 [213], explaining that these short peptides without dyad can be present in other α-KTx subfamilies.

Some longer α-KTx peptides (>30 amino acids) have also been demonstrated to lack the functional dyad. These native toxins or modified toxins (lacking the typical dyad motif) are used as models to uncover the mechanism underlying the interaction between these peptides and K_V1 channels. For example, A24-A33-Pil is a double mutant of toxin Pil (α-KTx 6.1) which lacks the functional dyad K24-Y33. However, this analogue of Pil was able to bind the channel (K_d = 22 μM), inferring that the functional dyad is not critical for recognition and binding to the channel [156]. Another report about Tc32 (α-KTx 18.1) described that during the interaction with K_V1.3 channel, the differences in the electrostatic properties of the toxin and the channel, the contact surfaces, and the total dipole moment orientations, lead to a Lys residue, even if it located at a different position from the typical functional dyad, physically plugging the pore of

the channel [214]. Computer simulation of the interaction between BmP02 and the K_V1.3 channel also demonstrated this effect of rearrangement. After the electrostatic interaction, the side chain of Lys11 (different position than the typical dyad) was oriented to enter the pore directly [215]. Thus, it could be speculated that the basic residues in Cm28 are involved in the recognition of the channel and the electrostatic forces may rearrange the toxin in such a way that the side chain of Lys located in either position protrude into the pore. Likewise, there is a possibility that the dyad is in the opposite orientation. This fact has already been reported for the κ-KTx 1.1 toxin, which interacts with ion channel through a reversed dyad motif, consisting of an aromatic residue Tyr5 and the Lys19 [216]. In Cm28, the reversely oriented function dyad might consist of Tyr13 and Lys22, which could have a similar interaction as the reversed dyad in κ-KTx 1.1 toxin. Obviously, a detailed structural study and molecular docking is needed to reveal the hidden mechanism of Cm28 interaction with K_V1.1-K_V1.3 channels.

Numerous scorpion toxins have been described which inhibit K_V1.3 with great affinity, however these toxins also affect the function of other physiologically critical ion channels thereby compromising the therapeutical potential of such peptides. Cm28 inhibits the K_V1.2 and K_V1.3 with similar potency (Fig. 13) and shows ~400-fold less affinity for K_V1.1 (Fig. 15). The order of the blocking potency of Cm28 for various ion channels was $hK_V1.2 \approx hK_V1.3 >> hK_V1.1 > hK_V1.5 \approx hK11_V.1 \approx hK_{Ca}3.1 \approx mK_{Ca}1.1 \approx hNa_V1.4 \approx hNa_V1.5 \approx hH_V1$ (Fig. 15). The selectivity for a certain target over other channels can be enhanced by proteins engineering. For example, Anuroctoxin (α-KTx 6.12, AnTx) with double substitution (N17A/F32T) was developed previously by our group which retained its natural potency for K_V1.3 while achieving 16,000-fold selectivity over K_V1.2 [167]. After revealing the key residues involved in the interaction with K_V1 channels, analogue of Cm28 can be created with improved selectivity for K_V1.3 over other Cm28 sensitive channels through mutation cycle analysis.

Cm28 exhibited immunosuppressive effects in biological functional assay by substantially downregulating the expression of IL2R and CD40L in human $CD4^+$ T_{EM} lymphocytes following TCR-mediated activation, like the positive control MgTx (Fig. 17). These results agree with previous reports and confirm the role of the K_V1.3 ion channels in T cell activation through maintaining the Ca^{2+} influx [75, 201, 217]. Excess concentration of Cm28 (~1000-fold the K_d for K_V1.3) was applied to ensure the complete blockade of K_V1.3 channels in cell culture setting, which is in accordance with the literature, where significantly higher concentrations of Vm24 and ShK were used in biological assays than the K_d of the toxin

for K_V1.3 [200, 201]. Additionally, it was also shown that treatment of cells with Cm28 for 24 h did not compromise their viability (Fig. 16).

The drug development process following the discovery of a potential peptide candidate involves various steps, especially the designing of modification that enhances the selectivity of the peptide to minimize side effects and improve its serum half-life. There is a wide variety of toxins that inhibit K_V1 channels with varying affinity and selectivity. However, the small size and unique primary structure of Cm28 may hold an advantage over other K_V1.3-inhibiting peptides. Shorter analogues of ShK toxin showed improved resistance to proteolysis because reduction in the peptide length makes the structure of the analogues more constrained and also the number of positively charged (Lys and Arg) residues and aromatic residues are decreased, making the peptides less susceptible to trypsin and chymotrypsin [218]. Besides, peptide cyclization of shorter peptides is a more feasible method not only to improve their proteolytic resistance but also their serum half-life [219]. Although Cm28 is a promising novel peptide, the strategies to improve its selectivity for K_V1.3 as discussed above must be employed and the benefits of the shorter Cm28 over other peptides must be experimentally confirmed to exploit the potential of Cm28 in the treatment of autoimmune disorders.

6.2 Characterization of a fluorescent peptide toxin as a probe for K_V1.3

This part of my thesis reports on the pharmacological characterization of Cy5-HsTX1[R14A], a peptide-based fluorescent probe that retains sub-nanomolar affinity for K_V1.3. Cy5 conjugation of the HsTX1[R14A] peptide lowered the affinity for K_V1.3 about 20-fold compared with the original unmodified peptide HsTX1[R14A] (K_d 853 pM vs 45 pM, respectively, Fig. 18). Previous studies have reported that N-terminus modification of α-KTxs can lead to loss of activity for K_V1.3 channel perhaps due to steric effects and unfavorable interactions between the channel and the toxin [175, 207]. For example, as we showed in section 5.3, His-tagged rMgTx lost ~1.6-fold affinity for K_V1.3 and K_V1.2 as compared with untagged rMgTx. Similarly, N-terminus modification of HsTX1[R14A] with 30 kDa monomethoxy-PEG lowered the affinity for K_V1.3 about 1000-fold [220], however, N-terminus tagging of HsTX1[R14A] with NOTA (1,4,7-triazacyclononane-triacetic acid) tag did not affect significantly the affinity for K_V1.3 (K_d = ~68 pM) [221]. Cy5-HsTX1[R14A] exhibited high selectivity for K_V1.3 over closely related K_V1 family channels (Fig. 19). Selectivity Cy5-HsTX1[R14A] for K_V1.3 over K_V1.5 and K_V1.3-K_V1.5 heterotetramers is valuable in perspectives where both channel subunits are co-expressed and functionally relevant, such as

in macrophages and microglia [23, 222]. We experimentally demonstrated that Cy5-HsTX1[R14A] is ~20-fold more selective for homotetrameric $K_V1.3$ over $K_V1.3$-$K_V1.5$ heterotetramers (Fig. 20). This will provide a significant advantage over anti-$K_V1.3$ antibodies which to date only target epitopes on single subunits and are therefore unable to distinguish homo- and heterotetrameric channels.

Cy5-HsTX1[R14A] is a promising tool for the detection of $K_V1.3$ overexpression in tissue samples (*e.g.*, peripheral blood mononuclear cells) for validation of novel autoimmune indications, using either microscopy or flow cytometry methods. $K_V1.3$ is endogenously expressed at a relatively low level, with an estimated 200−400 channels/cell in non-activated (naïve) T cells and 1500−2000 channels/cell in chronically activated T_{EM} cells [90, 173]. In the current work, initially as a proof of concept of probing capability of Cy5-HsTX1[R14A] was illustrated by flow cytometry using a heterologous system in which CHO cells stably overexpressed $K_V1.3$ channels (Fig. 21). However, ShK-F6CA has been used successfully in flow cytometry experiments to detect $K_V1.3$ in CNS-infiltrating monocytes in a mouse model of ischemic stroke [223], thereby suggesting that this might also be a viable approach for the use of Cy5-HsTX1[R14A].

The ability of Cy5-HsTX1[R14A] to enable live-cell imaging offers a valuable tool to immunohistochemistry for direct visualization of $K_V1.3$. It only binds to surface-localized functional channels, this would also allow to distinguish between folded and unfolded $K_V1.3$ channels. Another important advantage of Cy5-HsTX1[R14A] is its potential for *ex vivo* and *in vivo* tissue studies, due to tissue penetrating properties of far-red fluorescence emission of Cy5. Although fluorescence-based detection methods are typically less sensitive than radiolabeling-based techniques, our collaborators, Prof. Raymond Norton and his colleagues, have illustrated a potential application of Cy5-HsTX1[R14A] in a disease-relevant model of neuroinflammation. Using microscopy, they demonstrated that Cy5-HsTX1[R14A] can be used to identify the upregulation of $K_V1.3$ in lipopolysaccharide-stimulated immortalized murine BV-2 microglial cells. They have also demonstrated the utilization of Cy5-HsTX1[R14A] to track the peptide biodistribution in healthy mice following sc. injection of the peptide [206].

6.3 Optimization of recombinant production of margatoxin and the functional characterization of the tagged and untagged versions of the peptide

In this part of my thesis, we report enhanced production of rMgTx in *Pichia pastoris* using codon-optimized gene, by selecting Zeocin hyper-resistant transformants and optimizing

culturing conditions *i.e.*, pH, MeOH induction and fermentation duration. *Pichia* clones secreted 83 ± 3 mg/L of TrMgTx (*i.e.*, His-tagged rMgTx) into the culture medium of pH 6.0 after 72 h of fermentation following 0.5% MeOH induction. A two-step purification scheme including Ni^{2+} affinity chromatography and RP-HPLC yielded 36 ± 4 mg/L of >98% pure TrMgTx. Analytical RP-HPLC and mass spectrometry analysis confirmed the purity and homogeneity of the recombinant peptides. To study the impact of His-tag on the activity of rMgTx, an untagged version of rMgTx (UrMgTx) having native N-terminus was created by cleaving the tag from TrMgTx using factor Xa protease. In the single cell electrophysiology experiments we found that TrMgTx is slightly less potent than UrMgTx in the inhibition of either $K_V1.2$ (K_d = 64 pM vs. 14 pM, respectively) or $K_V1.3$ (K_d = 86 pM vs. 50 pM, respectively), although both peptides display picomolar affinity for the channels. The binding kinetics analysis showed that the slight reduction in the affinity of TrMgTx for $K_V1.2$ can be attributed to the decreased association and increased dissociation rate of the toxin-channel complex as compared to UrMgTx. Moreover, we demonstrated that both peptides markedly suppressed the IL2R and CD40L expression in activated $CD4^+$ T_{EM} cells in biological functional assays.

As discussed in previous sections, venom-derived peptide toxins have been under spotlight in the last two decades because of their huge therapeutic potential in treating various channelopathies. For examples α-KTxs which block $K_V1.3$ with remarkably high potency and can be exploited to treat autoimmune diseases and neuroinflammatory disorders [99, 224]. In addition, peptide toxins are widely used to investigate the physiological functions of various ion channels in different cell types *in vivo* as well as *in vitro* [225-228]. Therefore, a reliable and economical system is required to produce ample amount of peptide toxins and their engineered analogues for therapeutic development and to study the physiological role of ion channels. The natural resources (*e.g.*, venom glands) offer a very minute quantity of pure wild-type peptide which is usually insufficient for functional studies. Since the peptide toxins have complex structural features due to the presence of multiple disulfide-bridges, thus, their preparation either by chemical synthesis or recombinant synthesis in *E. coli* needs oxidative refolding and multiple repurification steps to acquire the biologically active conformers of the peptide [137]. Some engineered *E. coli* strains can form disulfide bonds [179, 180]. However, the yield of active conformers of disulfide-rich peptides either from chemical synthesis or in *E. coli* is not sufficient. For example, margatoxin produced in *E. coli* yields 3-4 mg/L of active peptide [142]. The *Pichia pastoris* expression system offers an economical and better approach

to overcome these limitations and produce higher amounts of active peptide. This system has many advantages as a host for heterologous production of proteins such as high biomass production in simple medium, ease of genetic manipulation, capability of performing post-translational modifications. Additionally, *P. pastoris* secretes the heterologous proteins into the medium with a very few endogenous proteins which significantly simplifies the downstream processing [186, 188]. In line with these Anangi *et al.* expressed and purified the His-tagged margatoxin and agitoxin in *Pichia* expression system with a yield of 12−15 mg/L and 14−18 mg/L, respectively [229].

The expression level of heterologous proteins in *P. pastoris* can be improved by implementing different approaches *e.g.*, the usage of codon-optimized genes, screening for high copy integrant, choice of efficient promoter and optimization of cell fermentation conditions [188, 194]. The usage of codon-optimized gene sequence increases the expression of heterologous protein about 1 to 10-fold in *P. pastoris* over the native gene sequence [191, 230-232]. For example, codon-optimization significantly enhanced the production of glucanase (10-fold larger than it produced by wild-type gene) in *P. pastoris* [192]. We designed the codon-biased MgTx gene according to the codon usage table for *P. pastoris* to improve the rMgTx expression. Generally, it is considered that the high copy number of the target gene linearly correlates with the higher expression of target protein [233-236]. Upon transformation into *P. pastoris*, multi-copy integration of expression cassette could occur spontaneously at a single locus by homologous recombination. We followed the post-transformational vector amplification method described by Sunga *et al*. [237] to create multi-copy clones of *P. pastoris*. Initially, transformants were selected on low concentration of Zeocin and then subject to gradually increasing higher concentrations (up to 2 mg/ml). Nordén *et al*. reported that hyper-resistance against Zeocin was linked with enhanced expression of foreign proteins in *P. pastoris* [236].

The overexpression of heterologous proteins in *P. pastoris* is a function of various fermentation factors such as biomass production, pH of the medium, MeOH induction, dissolved oxygen, and medium types. These factors differently influence the expression of a certain foreign protein in *P. pastoris* [188, 238-240]. Therefore, in this study, we first optimized the time-course of MeOH-induced peptide production and later determined the optimum concentration of MeOH for induction and the optimal pH of the medium to obtain the high-level expression of rMgTx. Since *AOX1* is a strong MeOH-induced promoter, it may alter the expression level of foreign protein upon feeding the different concentration of MeOH. The

optimized MeOH concentration for high-level expression of various proteins ranges between 0.1% to 3% (v/v) [240]. In our study, the yield of TrMgTx was maximal upon induction with 0.5% MeOH for 72 h (Fig. 23). Likewise, Mu *et al*. achieved enhanced expression (150 mg/L) of basic fibroblast growth factor at 0.5% (v/v) MeOH after 72 h of induction [241]. However, Zhang *et al*. found that the optimal MeOH concentration and induction time to attain higher yield of inulinase from are *P. pastoris* are 1.5% (v/v), 72 h, respectively [242]. The pH of the culture medium has also been optimized to improve the titer of recombinant proteins in *P. pastoris* since the pH is an important parameter which can affect the stability of a foreign protein. *P. pastoris* can grow on a wide pH range 3.0-7.0 without severely compromising the growth rate, however, the optimal pH varies for the overexpression of different heterologous proteins [188, 240]. In the case of TrMgTx, we observed that the best expression at pH 6.0 (Fig. 23). Similarly, the production of α-amylase, mouse epidermal growth factor and human serum albumin in *P. pastoris* was reported highest at pH 6.0 as well [243, 244] however, in case of insulin-like growth factor-I and human growth hormone the optimal pH was 5.0 and 3.0, respectively [245, 246]. These findings suggested that the culturing conditions must be optimized to achieve enhanced expression and secretion of foreign genes in *P. pastoris*. Conclusively, under the optimized conditions (0.5% MeOH induction, pH 6.0 for 72 h) *P. pastoris* produced 83 ± 3 mg/L of TrMgTx. The final yield of more than 98% pure TrMgTx was 36 ± 4 mg/L (Fig. 23−25) which is 3-fold higher than the previously reported yield for tagged rMgTx in *P. pastoris* and 10-12 times higher than the production in *E. coli* [142, 181, 229].

Both versions of recombinant MgTx (tagged and untagged) potently inhibited the $K_V1.2$ and $K_V1.3$ channels and the K_d values are consistent with previously reported data on native or recombinant MgTx [134, 142, 143]. However, TrMgTx is marginally less potent than UrMgTx (Fig. 27−28). This decrease in affinity of TrMgTx may be due to the presence of 14 additional residues at its N-terminus which may affect its interaction with the pore region of ion channel. As Chang *et al*. reported that N-terminally extended analogs of ShK toxin showed decreased affinity for $K_V1.3$ as compared with the native peptide toxin [247]. The kinetic parameters of UrMgTx binding are also parallel to that of native MgTx as described previously [66]. The block of $K_V1.3$ is full reversible with moderately fast association and dissociation rates, whereas the onset of the equilibrium block of $K_V1.2$ is relatively slow and reversibility of the block is limited during the time scale of the whole-cell patch-clamp recording (Fig. 26−27) [143]. TrMgTx exhibited ~1.6-fold lower association rate than that of UrMgTx for both $K_V1.2$ and

$K_V1.3$. This reduction in k_{on} rate could be explained by non-diffusion limited bimolecular toxin-channel interactions described by Escobar *et al*. [182] and Peter *et al*. [199]. In this model the transition from the toxin-channel encounter complex (EC) to the toxin bound state (B) is a rate limiting step which may involve the rearrangement of amino acid side chains, hydrogen-bond formation, and squeezing water molecules and cations out from the pore of the channel to make stable toxin-channel complex [199]. The additional amino acid residues at N-terminus of TrMgTx may affect this transition step thereby leading to the decrease in the k_{on} observed in this study. On the other hand, TrMgTx showed identical dissociation rate to that of UrMgTx for $K_V1.3$ however, the block of $K_V1.2$ by TrMgTx is fully reversible with considerably higher k_{off} than that of UrMgTx (Fig. 27−28). The high k_{off} might indicate that the presence of the N-terminus His-tag in TrMgTx creates unfavorable interactions between the channel and the toxin thereby shortening the toxin residence time [199].

In conclusion, we report that *Pichia* expression system is a powerful method to produce the disulfide-rich peptide MgTx and through optimization strategies expression of similar peptides could be improved remarkably, making it more cost-effective. rMgTx was produced with a very high yield as compared to the previous reports by optimizing several factors. We showed that the presence of the His-tag on rMgTx only slightly altered the block equilibrium and binding kinetics for K^+ channels. Furthermore, both tagged and untagged rMgTx equipotently suppress the proliferation of $CD4^+$ T_{EM} cells. Hence, TrMgTx can be an excellent tool as (i) it inhibits $K_V1.2$ and $K_V1.3$ in picomolar concentration (ii) the reversible nature of the block of $K_V1.2$ might be preferable for physiological studies and (iii) the production of TrMgTx does not require removal of tag and downstream purification steps rendering the process straightforward, easy, and economical. Additionally, the presence of His-tag can be exploited to detect and quantify the toxin concentration in biological fluids using anti-His-tag antibodies at the various steps of therapeutic development of toxins.

7. SUMMARY

The voltage-gated $K_V1.3$ potassium ion channels express in immune cells and are implicated in a range of autoimmune diseases and neuroinflammatory disorders. Selective blocking of $K_V1.3$ using peptides isolated from scorpion venom holds a great potential in developing immunomodulatory therapies. We discovered and characterized a novel short peptide in the venom of *C. margaritatus* (Cm28). Cm28 obeys a unique primary structure, consists of 27 amino acid residues and has <40% similarity with other known α-KTxs from scorpions. Cm28 reversibly inhibited $K_V1.2$ and $K_V1.3$ channels with K_d values of 0.96 and 1.3 nM, respectively. The biophysical characterization of the block revealed that Cm28 is not a gating modifier, but rather a pore blocker. Cm28 is ~400-fold selective for $K_V1.2$ and Kv1.3 over Kv1.1 and did not inhibit a variety of other K^+, Na^+ and H^+ channels at 150 nM concentration. Cm28 strongly downregulated the expression of two key early activation markers IL2R and CD40 ligand in stimulated human effector memory T cells. Cm28, due to its unique structure, may serve as a template for the generation of novel peptides targeting $K_V1.3$.

The high affinity and selectivity of peptide toxins for $K_V1.3$ make them suitable for the development of visualization tools to study the expression and the pharmacokinetics of peptide toxins. We developed a fluorescent analogue of HsTX1[R14A] having an N-terminus Cy5 tag. We showed that Cy5-HsTX1[R14A] retained high affinity and selectivity for $K_V1.3$ (K_d ~0.9 nM), even against channels formed by $K_V1.3$-$K_V1.5$ tandem dimers. Furthermore, flow cytometry demonstrated that Cy5-HsTX1[R14A] can identify $K_V1.3$-expressing CHO cells.

To generate ample amounts of $K_V1.3$ inhibitor toxins for pharmacology and therapeutic development processes we optimized *Pichia pastoris* expression system to produce ~36 mg/L of His-tagged margatoxin with >98% purity. This yield, which is 3-fold higher than has been previously reported, was achieved by optimizing the codon, the selection process, and the culturing conditions. Moreover, we showed that the His-tagged MgTx inhibited $K_V1.2$ and $K_V1.3$ channels with similar potency to the untagged MgTx, and significantly inhibited the IL2R and CD40 ligand in activated human effector memory T cells, thus, elimination of the tag removal reduces the cost of the production. These results suggest that *Pichia* expression system is a powerful method to produce the disulfide-rich peptide MgTx, the overexpression of similar peptides could be enhanced noticeably through optimization strategies, making it more cost-effective.

In summary, the data presented in the PhD dissertation resulted in a novel ion channel inhibitor peptide (Cm28), a new visualization tool for $K_V1.3$ (Cy5-HsTX1[R14A]) and an optimized method to produce MgTx in the *Pichia* expression system.

8. REFERENCES

1. Petkov, G.V., *Ion channels*, in *Pharmacology*. 2009, Elsevier. p. 387-427.
2. Zheng, J. and M.C. Trudeau, *Handbook of ion channels*. 2015: Crc Press.
3. Alexander, S.P., et al., *The concise guide to pharmacology 2019/20: Catalytic receptors.* British Journal of Pharmacology, 2019. **176**: p. S247-S296.
4. Capera, J., et al., *The potassium channel odyssey: mechanisms of traffic and membrane arrangement.* International Journal of Molecular Sciences, 2019. **20**(3): p. 734.
5. González, C., et al., *K+ channels: function-structural overview.* Comprehensive physiology, 2012. **2**(3): p. 2087-2149.
6. Hille, B., *Ionic channels: molecular pores of excitable membranes.* Harvey lectures, 1986. **82**: p. 47-69.
7. Benarroch, E.E., *Potassium channels: brief overview and implications in epilepsy.* Neurology, 2009. **72**(7): p. 664-669.
8. Gutman, G.A., et al., *International Union of Pharmacology. XLI. Compendium of voltage-gated ion channels: potassium channels.* Pharmacological reviews, 2003. **55**(4): p. 583-586.
9. Gutman, G.A., et al., *International Union of Pharmacology. LIII. Nomenclature and molecular relationships of voltage-gated potassium channels.* Pharmacological reviews, 2005. **57**(4): p. 473-508.
10. Wei, A.D., et al., *International Union of Pharmacology. LII. Nomenclature and molecular relationships of calcium-activated potassium channels.* Pharmacological reviews, 2005. **57**(4): p. 463-472.
11. Kaczmarek, L.K., et al., *International union of basic and clinical pharmacology. C. Nomenclature and properties of calcium-activated and sodium-activated potassium channels.* Pharmacological reviews, 2017. **69**(1): p. 1-11.
12. Brown, B.M., et al., *Pharmacology of small-and intermediate-conductance calcium-activated potassium channels.* Annual review of pharmacology and toxicology, 2020. **60**: p. 219-240.
13. Xia, X.-M., et al., *Mechanism of calcium gating in small-conductance calcium-activated potassium channels.* Nature, 1998. **395**(6701): p. 503-507.
14. Ishii, T.M., et al., *A human intermediate conductance calcium-activated potassium channel.* Proceedings of the National Academy of Sciences, 1997. **94**(21): p. 11651-11656.
15. Joiner, W.J., et al., *hSK4, a member of a novel subfamily of calcium-activated potassium channels.* Proceedings of the National Academy of Sciences, 1997. **94**(20): p. 11013-11018.
16. Sheng, M., et al., *Subcellular segregation of two A-type K+ channel proteins in rat central neurons.* Neuron, 1992. **9**(2): p. 271-284.
17. Rusznak, Z., et al., *Voltage-gated potassium channel (Kv) subunits expressed in the rat cochlear nucleus.* J Histochem Cytochem, 2008. **56**(5): p. 443-65.
18. Pérez-García, M.T., P. Cidad, and J.R. López-López, *The secret life of ion channels: Kv1.3 potassium channels and proliferation.* Am J Physiol Cell Physiol, 2018. **314**(1): p. C27-c42.
19. Feske, S., H. Wulff, and E.Y. Skolnik, *Ion channels in innate and adaptive immunity.* Annual review of immunology, 2015. **33**: p. 291.
20. Stühmer, W., et al., *Molecular basis of functional diversity of voltage-gated potassium channels in mammalian brain.* The EMBO journal, 1989. **8**(11): p. 3235-3244.
21. Tamkun, M.M., et al., *Molecular cloning and characterization of two voltage-gated K+ channel cDNAs from human ventricle.* The FASEB Journal, 1991. **5**(3): p. 331-337.

22. Blair, T.A., et al., *Functional characterization of RK5, a voltage-gated K+ channel cloned from the rat cardiovascular system.* FEBS Lett, 1991. **295**(1-3): p. 211-3.
23. Vicente, R., et al., *Association of Kv1.5 and Kv1.3 contributes to the major voltage-dependent K+ channel in macrophages.* J Biol Chem, 2006. **281**(49): p. 37675-85.
24. Glazebrook, P.A., et al., *Potassium channels Kv1. 1, Kv1. 2 and Kv1. 6 influence excitability of rat visceral sensory neurons.* The Journal of physiology, 2002. **541**(2): p. 467-482.
25. Sanguinetti, M.C., et al., *A mechanistic link between an inherited and an acquird cardiac arrthytmia: HERG encodes the IKr potassium channel.* Cell, 1995. **81**(2): p. 299-307.
26. Anderson, C.L., et al., *Large-scale mutational analysis of Kv11. 1 reveals molecular insights into type 2 long QT syndrome.* Nature communications, 2014. **5**(1): p. 1-13.
27. Grimm, P.R., et al., *Identification and localization of BK-β subunits in the distal nephron of the mouse kidney.* American Journal of Physiology-Renal Physiology, 2007. **293**(1): p. F350-F359.
28. Goldin, A.L., *Diversity of mammalian voltage-gated sodium channels.* Annals of the New York Academy of Sciences, 1999. **868**(1): p. 38-50.
29. de Lera Ruiz, M. and R.L. Kraus, *Voltage-gated sodium channels: structure, function, pharmacology, and clinical indications.* Journal of medicinal chemistry, 2015. **58**(18): p. 7093-7118.
30. Catterall, W.A., A.L. Goldin, and S.G. Waxman, *International Union of Pharmacology. XLVII. Nomenclature and structure-function relationships of voltage-gated sodium channels.* Pharmacological reviews, 2005. **57**(4): p. 397-409.
31. Wu, L.-J., *Voltage-gated proton channel HV1 in microglia.* The Neuroscientist, 2014. **20**(6): p. 599-609.
32. He, J., R.M. Ritzel, and J. Wu, *Functions and mechanisms of the voltage-gated proton channel Hv1 in brain and spinal cord injury.* Frontiers in Cellular Neuroscience, 2021. **15**: p. 662971.
33. Cestèle, S. and W.A. Catterall, *Molecular mechanisms of neurotoxin action on voltage-gated sodium channels.* Biochimie, 2000. **82**(9-10): p. 883-892.
34. Doyle, D.A., et al., *The structure of the potassium channel: molecular basis of K+ conduction and selectivity.* science, 1998. **280**(5360): p. 69-77.
35. Jiang, Y., et al., *X-ray structure of a voltage-dependent K+ channel.* Nature, 2003. **423**(6935): p. 33-41.
36. Long, S.B., E.B. Campbell, and R. MacKinnon, *Crystal structure of a mammalian voltage-dependent Shaker family K+ channel.* Science, 2005. **309**(5736): p. 897-903.
37. Long, S.B., et al., *Atomic structure of a voltage-dependent K+ channel in a lipid membrane-like environment.* Nature, 2007. **450**(7168): p. 376-382.
38. Selvakumar, P., et al., *Structures of the T cell potassium channel Kv1.3 with immunoglobulin modulators.* Nature Communications, 2022. **13**(1): p. 3854.
39. Tyagi, A., et al., *Rearrangement of a unique Kv1. 3 selectivity filter conformation upon binding of a drug.* Proceedings of the National Academy of Sciences, 2022. **119**(5): p. e2113536119.
40. Liu, S., et al., *Structures of wild-type and H451N mutant human lymphocyte potassium channel KV1. 3.* Cell discovery, 2021. **7**(1): p. 1-5.
41. DeCoursey, T.E., et al., *Voltage-gated K+ channels in human T lymphocytes: a role in mitogenesis?* Nature, 1984. **307**(5950): p. 465-468.
42. Cahalan, M., et al., *A voltage-gated potassium channel in human T lymphocytes.* The Journal of physiology, 1985. **358**(1): p. 197-237.

43. Panyi, G., *Biophysical and pharmacological aspects of K+ channels in T lymphocytes.* Eur Biophys J, 2005. **34**(6): p. 515-529.
44. Long, S.B., E.B. Campbell, and R. MacKinnon, *Voltage sensor of Kv1. 2: structural basis of electromechanical coupling.* Science, 2005. **309**(5736): p. 903-908.
45. Matthies, D., et al., *Single-particle cryo-EM structure of a voltage-activated potassium channel in lipid nanodiscs.* Elife, 2018. **7**: p. e37558.
46. Tan, X.-F., et al., *Structure of the Shaker Kv channel and mechanism of slow C-type inactivation.* Science advances, 2022. **8**(11): p. eabm7814.
47. Zhou, Y., et al., *Chemistry of ion coordination and hydration revealed by a K+ channel–Fab complex at 2.0 Å resolution.* Nature, 2001. **414**(6859): p. 43-48.
48. Heginbotham, L., et al., *Mutations in the K+ channel signature sequence.* Biophysical journal, 1994. **66**(4): p. 1061-1067.
49. Nimigean, C.M. and T.W. Allen, *Origins of ion selectivity in potassium channels from the perspective of channel block.* Journal of General Physiology, 2011. **137**(5): p. 405-413.
50. Morais-Cabral, J.H., Y. Zhou, and R. MacKinnon, *Energetic optimization of ion conduction rate by the K+ selectivity filter.* Nature, 2001. **414**(6859): p. 37-42.
51. Bezanilla, F., *The voltage sensor in voltage-dependent ion channels.* Physiological reviews, 2000. **80**(2): p. 555-592.
52. Larsson, H.P., et al., *Transmembrane movement of the shaker K+ channel S4.* Neuron, 1996. **16**(2): p. 387-397.
53. Baker, O., et al., *Three transmembrane conformations and sequence-dependent displacement of the S4 domain in shaker K+ channel gating.* Neuron, 1998. **20**(6): p. 1283-1294.
54. Yellen, G., *The voltage-gated potassium channels and their relatives.* nature, 2002. **419**(6902): p. 35-42.
55. Ledwell, J.L. and R.W. Aldrich, *Mutations in the S4 region isolate the final voltage-dependent cooperative step in potassium channel activation.* The Journal of general physiology, 1999. **113**(3): p. 389-414.
56. MacKinnon, R., *Determination of the subunit stoichiometry of a voltage-activated potassium channel.* Nature, 1991. **350**(6315): p. 232-235.
57. Panyi, G., Z. Sheng, and C. Deutsch, *C-type inactivation of a voltage-gated K+ channel occurs by a cooperative mechanism.* Biophysical journal, 1995. **69**(3): p. 896-903.
58. Lee, T., L. Philipson, and D. Nelson, *N-type inactivation in the mammalian Shaker K+ channel Kv1. 4.* The Journal of membrane biology, 1996. **151**(3): p. 225-235.
59. Hoshi, T. and C.M. Armstrong, *C-type inactivation of voltage-gated K+ channels: pore constriction or dilation?* Journal of General Physiology, 2013. **141**(2): p. 151-160.
60. Cuello, L.G., et al., *Structural basis for the coupling between activation and inactivation gates in K+ channels.* Nature, 2010. **466**(7303): p. 272-275.
61. Pau, V., et al., *Crystal structure of an inactivated mutant mammalian voltage-gated K+ channel.* Nature structural & molecular biology, 2017. **24**(10): p. 857-865.
62. Hoshi, T., W.N. Zagotta, and R.W. Aldrich, *Two types of inactivation in Shaker K+ channels: effects of alterations in the carboxy-terminal region.* Neuron, 1991. **7**(4): p. 547-556.
63. Ong, S.T., et al., *Mechanisms Underlying C-type Inactivation in Kv Channels: Lessons From Structures of Human Kv1. 3 and Fly Shaker-IR Channels.* Frontiers in Pharmacology, 2022. **13**.
64. Reddi, R., et al., *Structural basis for C-type inactivation in a Shaker family voltage-gated K+ channel.* Science advances, 2022. **8**(16): p. eabm8804.

65. Aiyar, J., et al., *Topology of the pore-region of a K+ channel revealed by the NMR-derived structures of scorpion toxins.* Neuron, 1995. **15**(5): p. 1169-1181.
66. Goldstein, S. and C. Miller, *Mechanism of charybdotoxin block of a voltage-gated K+ channel.* Biophysical journal, 1993. **65**(4): p. 1613-1619.
67. Pahapill, P. and L. Schlichter, *Modulation of potassium channels in human T lymphocytes: effects of temperature.* The Journal of physiology, 1990. **422**(1): p. 103-126.
68. Verheugen, J.A., et al., *Voltage-gated and Ca(2+)-activated K+ channels in intact human T lymphocytes. Noninvasive measurements of membrane currents, membrane potential, and intracellular calcium.* Journal of General Physiology, 1995. **105**(6): p. 765-794.
69. Pahapill, P.A. and L.C. Schlichter, *Modulation of potassium channels in intact human T lymphocytes.* J Physiol, 1992. **445**: p. 407-30.
70. Tajti, G., et al., *Immunomagnetic separation is a suitable method for electrophysiology and ion channel pharmacology studies on T cells.* Channels, 2021. **15**(1): p. 53-66.
71. Papp, F., et al., *Tst26, a novel peptide blocker of Kv1. 2 and Kv1. 3 channels from the venom of Tityus stigmurus.* Toxicon, 2009. **54**(4): p. 379-389.
72. Janeway Jr, C.A., et al., *The components of the immune system*, in *Immunobiology: The Immune System in Health and Disease. 5th edition*. 2001, Garland Science.
73. Janeway Jr, C.A., et al., *Autoimmune responses are directed against self antigens*, in *Immunobiology: The Immune System in Health and Disease. 5th edition*. 2001, Garland Science.
74. Perez-Verdaguer, M., et al., *The voltage-gated potassium channel Kv1. 3 is a promising multitherapeutic target against human pathologies.* Expert opinion on therapeutic targets, 2016. **20**(5): p. 577-591.
75. Panyi, G., et al., *K+ channel blockers: novel tools to inhibit T cell activation leading to specific immunosuppression.* Current pharmaceutical design, 2006. **12**(18): p. 2199-2220.
76. Cahalan, M.D. and K.G. Chandy, *The functional network of ion channels in T lymphocytes.* Immunological reviews, 2009. **231**(1): p. 59-87.
77. Perez-Villar, J.J. and S.B. Kanner, *Regulated association between the tyrosine kinase Emt/Itk/Tsk and phospholipase-Cγ1 in human T lymphocytes.* The Journal of Immunology, 1999. **163**(12): p. 6435-6441.
78. Zhang, S.L., et al., *STIM1 is a Ca2+ sensor that activates CRAC channels and migrates from the Ca2+ store to the plasma membrane.* Nature, 2005. **437**(7060): p. 902-905.
79. Lewis, R.S., *Store-operated calcium channels.* Advances in second messenger and phosphoprotein research, 1999: p. 279-307.
80. Vaeth, M., S. Kahlfuss, and S. Feske, *CRAC channels and calcium signaling in T cell-mediated immunity.* Trends in immunology, 2020. **41**(10): p. 878-901.
81. Rao, A., C. Luo, and P.G. Hogan, *Transcription factors of the NFAT family: regulation and function.* Annual review of immunology, 1997. **15**(1): p. 707-747.
82. Panyi, G., C. Beeton, and A. Felipe, *Ion channels and anti-cancer immunity.* Philosophical Transactions of the Royal Society B: Biological Sciences, 2014. **369**(1638): p. 20130106.
83. Vaeth, M. and S. Feske, *NFAT control of immune function: New Frontiers for an Abiding Trooper*. F1000Research, 2018. **7**.
84. Jin, J., et al., *Deletion of Trpm7 disrupts embryonic development and thymopoiesis without altering Mg2+ homeostasis.* Science, 2008. **322**(5902): p. 756-760.

85. Brock, V.J., et al., *P2X4 and P2X7 are essential players in basal T cell activity and Ca2+ signaling milliseconds after T cell activation.* Science advances, 2022. **8**(5): p. eabl9770.
86. Chiang, E.Y., et al., *Potassium channels Kv1. 3 and KCa3. 1 cooperatively and compensatorily regulate antigen-specific memory T cell functions.* Nature communications, 2017. **8**(1): p. 1-16.
87. Chandy, K., et al., *Voltage-gated potassium channels are required for human T lymphocyte activation.* The Journal of experimental medicine, 1984. **160**(2): p. 369-385.
88. Lam, J. and H. Wulff, *The lymphocyte potassium channels Kv1. 3 and KCa3. 1 as targets for immunosuppression.* Drug development research, 2011. **72**(7): p. 573-584.
89. Ghanshani, S., et al., *Up-regulation of the IKCa1 potassium channel during T-cell activation: molecular mechanism and functional consequences.* Journal of Biological Chemistry, 2000. **275**(47): p. 37137-37149.
90. Wulff, H., et al., *The voltage-gated Kv1. 3 K+ channel in effector memory T cells as new target for MS.* The Journal of clinical investigation, 2003. **111**(11): p. 1703-1713.
91. Reise, S.P. and N.G. Waller, *Item response theory and clinical measurement.* Annual review of clinical psychology, 2009. **5**(1): p. 27-48.
92. Hu, L., et al., *Functional blockade of the voltage-gated potassium channel Kv1. 3 mediates reversion of T effector to central memory lymphocytes through SMAD3/p21cip1 signaling.* Journal of Biological Chemistry, 2012. **287**(2): p. 1261-1268.
93. Varga, Z., et al., *Potassium channel expression in human CD4+ regulatory and naïve T cells from healthy subjects and multiple sclerosis patients.* Immunol Lett, 2009. **124**(2): p. 95-101.
94. Chandy, K.G. and R.S. Norton, *Peptide blockers of Kv1. 3 channels in T cells as therapeutics for autoimmune disease.* Current opinion in chemical biology, 2017. **38**: p. 97-107.
95. Serrano-Albarrás, A., et al., *Fighting rheumatoid arthritis: Kv1. 3 as a therapeutic target.* Biochemical Pharmacology, 2019. **165**: p. 214-220.
96. Tajti, G., et al., *The voltage-gated potassium channel KV1. 3 as a therapeutic target for venom-derived peptides.* Biochemical pharmacology, 2020. **181**: p. 114146.
97. Hayter, S.M. and M.C. Cook, *Updated assessment of the prevalence, spectrum and case definition of autoimmune disease.* Autoimmun Rev, 2012. **11**(10): p. 754-65.
98. Chatenoud, L., *Precision medicine for autoimmune disease.* Nature biotechnology, 2016. **34**(9): p. 930-932.
99. Shen, B., et al., *Treating autoimmune disorders with venom-derived peptides.* Expert opinion on biological therapy, 2017. **17**(9): p. 1065-1075.
100. Beeton, C., et al., *Selective blockade of T lymphocyte K+ channels ameliorates experimental autoimmune encephalomyelitis, a model for multiple sclerosis.* Proceedings of the national academy of sciences, 2001. **98**(24): p. 13942-13947.
101. Beeton, C., et al., *Kv1. 3 channels are a therapeutic target for T cell-mediated autoimmune diseases.* Proceedings of the National Academy of Sciences, 2006. **103**(46): p. 17414-17419.
102. Kundu-Raychaudhuri, S., et al., *Kv1. 3 in psoriatic disease: PAP-1, a small molecule inhibitor of Kv1. 3 is effective in the SCID mouse psoriasis–xenograft model.* Journal of autoimmunity, 2014. **55**: p. 63-72.
103. Gilhar, A., et al., *Blocking potassium channels (Kv1. 3): a new treatment option for alopecia areata?* The Journal of Investigative Dermatology, 2013. **133**(8): p. 2088-2091.

104. Hyodo, T., et al., *Voltage-gated potassium channel Kv1. 3 blocker as a potential treatment for rat anti-glomerular basement membrane glomerulonephritis.* American Journal of Physiology-Renal Physiology, 2010. **299**(6): p. F1258-F1269.
105. Rus, H., et al., *The voltage-gated potassium channel Kv1. 3 is highly expressed on inflammatory infiltrates in multiple sclerosis brain.* Proceedings of the National Academy of Sciences, 2005. **102**(31): p. 11094-11099.
106. Beeton, C. and K.G. Chandy, *Potassium channels, memory T cells, and multiple sclerosis.* The Neuroscientist, 2005. **11**(6): p. 550-562.
107. Gocke, A.R., et al., *Kv1. 3 deletion biases T cells toward an immunoregulatory phenotype and renders mice resistant to autoimmune encephalomyelitis.* The Journal of Immunology, 2012. **188**(12): p. 5877-5886.
108. Matheu, M.P., et al., *Imaging of effector memory T cells during a delayed-type hypersensitivity reaction and suppression by Kv1. 3 channel block.* Immunity, 2008. **29**(4): p. 602-614.
109. Cañas, C.A., S. Castaño-Valencia, and F. Castro-Herrera, *Pharmacological blockade of KV1. 3 channel as a promising treatment in autoimmune diseases.* Journal of Translational Autoimmunity, 2022: p. 100146.
110. Watanabe, M., Y. Toyama, and A. Nishiyama, *Differentiation of proliferated NG2-positive glial progenitor cells in a remyelinating lesion.* J Neurosci Res, 2002. **69**(6): p. 826-36.
111. Attali, B., et al., *Characterization of delayed rectifier Kv channels in oligodendrocytes and progenitor cells.* J Neurosci, 1997. **17**(21): p. 8234-45.
112. Nörenberg, W., P.J. Gebicke-Haerter, and P. Illes, *Inflammatory stimuli induce a new K+ outward current in cultured rat microglia.* Neurosci Lett, 1992. **147**(2): p. 171-4.
113. Charolidi, N., T. Schilling, and C. Eder, *Microglial Kv1.3 Channels and P2Y12 Receptors Differentially Regulate Cytokine and Chemokine Release from Brain Slices of Young Adult and Aged Mice.* PLoS One, 2015. **10**(5): p. e0128463.
114. Stebbing, M.J., J.M. Cottee, and I. Rana, *The Role of Ion Channels in Microglial Activation and Proliferation - A Complex Interplay between Ligand-Gated Ion Channels, K(+) Channels, and Intracellular Ca(2.).* Front Immunol, 2015. **6**: p. 497.
115. Pannasch, U., et al., *The potassium channels Kv1.5 and Kv1.3 modulate distinct functions of microglia.* Mol Cell Neurosci, 2006. **33**(4): p. 401-11.
116. Rangaraju, S., et al., *Potassium channel Kv1.3 is highly expressed by microglia in human Alzheimer's disease.* J Alzheimers Dis, 2015. **44**(3): p. 797-808.
117. Sarkar, S., et al., *Kv1.3 modulates neuroinflammation and neurodegeneration in Parkinson's disease.* J Clin Invest, 2020. **130**(8): p. 4195-4212.
118. Chen, Y.-J., et al., *Inhibition of the potassium channel Kv1.3 reduces infarction and inflammation in ischemic stroke.* Annals of Clinical and Translational Neurology, 2018. **5**(2): p. 147-161.
119. Liu, J., et al., *Involvement of Kv1.3 and p38 MAPK signaling in HIV-1 glycoprotein 120-induced microglia neurotoxicity.* Cell Death Dis, 2012. **3**(1): p. e254.
120. Koshy, S., et al., *Blocking KV1.3 channels inhibits Th2 lymphocyte function and treats a rat model of asthma.* J Biol Chem, 2014. **289**(18): p. 12623-32.
121. Azam, P., et al., *Targeting effector memory T cells with the small molecule Kv1.3 blocker PAP-1 suppresses allergic contact dermatitis.* J Invest Dermatol, 2007. **127**(6): p. 1419-29.
122. Wu, X., et al., *Effect of the Kv1.3 voltage-gated potassium channel blocker PAP-1 on the initiation and progress of atherosclerosis in a rat model.* Heart Vessels, 2015. **30**(1): p. 108-14.

123. Kazama, I., *Roles of lymphocyte kv1.3-channels in the pathogenesis of renal diseases and novel therapeutic implications of targeting the channels.* Mediators Inflamm, 2015. **2015**: p. 436572.
124. Yanaba, K., et al., *B cell depletion delays collagen-induced arthritis in mice: arthritis induction requires synergy between humoral and cell-mediated immunity.* J Immunol, 2007. **179**(2): p. 1369-80.
125. Yang, Y., et al., *Specific Kv1.3 blockade modulates key cholesterol-metabolism-associated molecules in human macrophages exposed to ox-LDL.* J Lipid Res, 2013. **54**(1): p. 34-43.
126. Upadhyay, S.K., et al., *Selective Kv1.3 channel blocker as therapeutic for obesity and insulin resistance.* Proc Natl Acad Sci U S A, 2013. **110**(24): p. E2239-48.
127. Kourrich, S., C. Mourre, and B. Soumireu-Mourat, *Kaliotoxin, a Kv1.1 and Kv1.3 channel blocker, improves associative learning in rats.* Behav Brain Res, 2001. **120**(1): p. 35-46.
128. Comes, N., et al., *The voltage-dependent K(+) channels Kv1.3 and Kv1.5 in human cancer.* Front Physiol, 2013. **4**: p. 283.
129. Szabo, I., et al., *Biophysical characterization and expression analysis of Kv1.3 potassium channel in primary human leukemic B cells.* Cell Physiol Biochem, 2015. **37**(3): p. 965-78.
130. Teisseyre, A., et al., *Voltage-Gated Potassium Channel Kv1.3 as a Target in Therapy of Cancer.* Front Oncol, 2019. **9**: p. 933.
131. Checchetto, V., E. Prosdocimi, and L. Leanza, *Mitochondrial Kv1.3: a New Target in Cancer Biology?* Cell Physiol Biochem, 2019. **53**(S1): p. 52-62.
132. Prosdocimi, E., V. Checchetto, and L. Leanza, *Targeting the Mitochondrial Potassium Channel Kv1.3 to Kill Cancer Cells: Drugs, Strategies, and New Perspectives.* SLAS Discov, 2019. **24**(9): p. 882-892.
133. Gubič, Š., et al., *Discovery of K(V) 1.3 ion channel inhibitors: Medicinal chemistry approaches and challenges.* Med Res Rev, 2021. **41**(4): p. 2423-2473.
134. Chandy, K.G., et al., *K+ channels as targets for specific immunomodulation.* Trends in pharmacological sciences, 2004. **25**(5): p. 280-289.
135. Vennekamp, J., et al., *Kv1.3-blocking 5-phenylalkoxypsoralens: a new class of immunomodulators.* Mol Pharmacol, 2004. **65**(6): p. 1364-74.
136. Schmitz, A., et al., *Design of PAP-1, a selective small molecule Kv1. 3 blocker, for the suppression of effector memory T cells in autoimmune diseases.* Molecular pharmacology, 2005. **68**(5): p. 1254-1270.
137. Kuzmenkov, A., E. Grishin, and A. Vassilevski, *Diversity of potassium channel ligands: focus on scorpion toxins.* Biochemistry (Moscow), 2015. **80**(13): p. 1764-1799.
138. Banks, B., et al., *Apamin blocks certain neurotransmitter-induced increases in potassium permeability.* Nature, 1979. **282**(5737): p. 415-417.
139. Hugues, M., et al., *Apamin as a selective blocker of the calcium-dependent potassium channel in neuroblastoma cells: voltage-clamp and biochemical characterization of the toxin receptor.* Proceedings of the National Academy of Sciences, 1982. **79**(4): p. 1308-1312.
140. Carbone, E., et al., *Selective blockage of voltage-dependent K+ channels by a novel scorpion toxin.* Nature, 1982. **296**(5852): p. 90-91.
141. Miller, C., et al., *Charybdotoxin, a protein inhibitor of single Ca2+-activated K+ channels from mammalian skeletal muscle.* Nature, 1985. **313**(6000): p. 316-318.
142. Garcia-Calvo, M., et al., *Purification, characterization, and biosynthesis of margatoxin, a component of Centruroides margaritatus venom that selectively inhibits voltage-*

dependent potassium channels. Journal of Biological Chemistry, 1993. **268**(25): p. 18866-18874.
143. Bartok, A., et al., *Margatoxin is a non-selective inhibitor of human Kv1. 3 K+ channels.* Toxicon, 2014. **87**: p. 6-16.
144. Castañeda, O., et al., *Characterization of a potassium channel toxin from the Caribbean Sea anemone Stichodactyla helianthus.* Toxicon, 1995. **33**(5): p. 603-613.
145. Kalman, K., et al., *ShK-Dap22, a potent Kv1. 3-specific immunosuppressive polypeptide.* Journal of Biological Chemistry, 1998. **273**(49): p. 32697-32707.
146. Garcia, M., et al., *Potassium channels: from scorpion venoms to high-resolution structure.* Toxicon, 2001. **39**(6): p. 739-748.
147. Hidalgo, P. and R. MacKinnon, *Revealing the architecture of a K+ channel pore through mutant cycles with a peptide inhibitor.* Science, 1995. **268**(5208): p. 307-310.
148. Tabakmakher, V.M., et al., *Kalium 2.0, a comprehensive database of polypeptide ligands of potassium channels.* Scientific data, 2019. **6**(1): p. 1-8.
149. Tytgat, J., et al., *A unified nomenclature for short-chain peptides isolated from scorpion venoms: α-KTx molecular subfamilies.* Trends in pharmacological sciences, 1999. **20**(11): p. 444-447.
150. de la Vega, R.C.R.g. and L.D. Possani, *Current views on scorpion toxins specific for K+-channels.* Toxicon, 2004. **43**(8): p. 865-875.
151. Dauplais, M., et al., *On the convergent evolution of animal toxins: conservation of a diad of functional residues in potassium channel-blocking toxins with unrelated structures.* Journal of Biological Chemistry, 1997. **272**(7): p. 4302-4309.
152. Gurrola, G.B., et al., *Structure, function, and chemical synthesis of Vaejovis mexicanus peptide 24: a novel potent blocker of Kv1. 3 potassium channels of human T lymphocytes.* Biochemistry, 2012. **51**(19): p. 4049-4061.
153. Jouirou, B., et al., *Toxin determinants required for interaction with voltage-gated K+ channels.* Toxicon, 2004. **43**(8): p. 909-914.
154. M'Barek, S., et al., *Synthesis and characterization of Pi4, a scorpion toxin from Pandinus imperator that acts on K+ channels.* European journal of biochemistry, 2003. **270**(17): p. 3583-3592.
155. LEBRUN, B., et al., *A four-disulphide-bridged toxin, with high affinity towards voltage-gated K+ channels, isolated from Heterometrus spinnifer (Scorpionidae) venom.* Biochemical journal, 1997. **328**(1): p. 321-327.
156. Mouhat, S., et al., *The functional dyad of scorpion toxin Pi1 is not itself a prerequisite for toxin binding to the voltage-gated Kv1. 2 potassium channels.* Biochemical Journal, 2004. **377**(1): p. 25-36.
157. Zhu, L., et al., *Two dyad-free Shaker-type K+ channel blockers from scorpion venom.* Toxicon, 2012. **59**(3): p. 402-407.
158. Batista, C.V., et al., *Two novel toxins from the Amazonian scorpion Tityus cambridgei that block Kv1. 3 and Shaker B K+-channels with distinctly different affinities.* Biochimica et Biophysica Acta (BBA)-Proteins and Proteomics, 2002. **1601**(2): p. 123-131.
159. Swartz, K.J., *Tarantula toxins interacting with voltage sensors in potassium channels.* Toxicon, 2007. **49**(2): p. 213-230.
160. Swartz, K.J. and R. MacKinnon, *Hanatoxin modifies the gating of a voltage-dependent K+ channel through multiple binding sites.* Neuron, 1997. **18**(4): p. 665-673.
161. Mouhat, S., et al., *K+ channel types targeted by synthetic OSK1, a toxin from Orthochirus scrobiculosus scorpion venom.* Biochemical Journal, 2005. **385**(1): p. 95-104.

162. Bagdáany, M., et al., *Anuroctoxin, a new scorpion toxin of the α-KTx 6 subfamily, is highly selective for Kv1. 3 over IKCa1 ion channels of human T lymphocytes.* Molecular pharmacology, 2005. **67**(4): p. 1034-1044.
163. Varga, Z., et al., *Vm24, a natural immunosuppressive peptide, potently and selectively blocks Kv1. 3 potassium channels of human T cells.* Molecular pharmacology, 2012. **82**(3): p. 372-382.
164. Varga, Z., G. Tajti, and G. Panyi, *The Kv1. 3 K+ channel in the immune system and its "precision pharmacology" using peptide toxins.* Biologia futura, 2021. **72**(1): p. 75-83.
165. Mouhat, S., et al., *Pharmacological profiling of Orthochirus scrobiculosus toxin 1 analogs with a trimmed N-terminal domain.* Molecular Pharmacology, 2006. **69**(1): p. 354-362.
166. Rashid, M.H., et al., *A potent and Kv1. 3-selective analogue of the scorpion toxin HsTX1 as a potential therapeutic for autoimmune diseases.* Scientific reports, 2014. **4**(1): p. 1-9.
167. Bartok, A., et al., *An engineered scorpion toxin analogue with improved Kv1. 3 selectivity displays reduced conformational flexibility.* Scientific reports, 2015. **5**(1): p. 1-13.
168. Csoti, A., et al., *sVmKTx, a transcriptome analysis-based synthetic peptide analogue of Vm24, inhibits Kv1. 3 channels of human T cells with improved selectivity.* Biochemical Pharmacology, 2022. **199**: p. 115023.
169. Pennington, M.W., et al., *Development of highly selective Kv1. 3-blocking peptides based on the sea anemone peptide ShK.* Marine Drugs, 2015. **13**(1): p. 529-542.
170. Tarcha, E.J., et al., *Durable pharmacological responses from the peptide ShK-186, a specific Kv1.3 channel inhibitor that suppresses T cell mediators of autoimmune disease.* J Pharmacol Exp Ther, 2012. **342**(3): p. 642-53.
171. Tarcha, E.J., et al., *Safety and pharmacodynamics of dalazatide, a Kv1.3 channel inhibitor, in the treatment of plaque psoriasis: A randomized phase 1b trial.* PLoS One, 2017. **12**(7): p. e0180762.
172. Bednenko, J., et al. *A multiplatform strategy for the discovery of conventional monoclonal antibodies that inhibit the voltage-gated potassium channel Kv1. 3*. in *MAbs*. 2018. Taylor & Francis.
173. Beeton, C., et al., *A novel fluorescent toxin to detect and investigate Kv1. 3 channel up-regulation in chronically activated T lymphocytes.* Journal of Biological Chemistry, 2003. **278**(11): p. 9928-9937.
174. Denisova, K.R., et al., *GFP–Margatoxin, a Genetically Encoded Fluorescent Ligand to Probe Affinity of Kv1. 3 Channel Blockers.* International Journal of Molecular Sciences, 2022. **23**(3): p. 1724.
175. Kuzmenkov, A.I., et al., *Fluorescent protein-scorpion toxin chimera is a convenient molecular tool for studies of potassium channels.* Scientific reports, 2016. **6**(1): p. 1-10.
176. Nekrasova, O.V., et al., *N-Terminal Tagging with GFP Enhances Selectivity of Agitoxin 2 to Kv1. 3-Channel Binding Site.* Toxins, 2020. **12**(12): p. 802.
177. Jensen, J.E., et al., *Chemical synthesis and folding of APETx2, a potent and selective inhibitor of acid sensing ion channel 3.* Toxicon, 2009. **54**(1): p. 56-61.
178. Rudolph, R. and H. Lilie, *In vitro folding of inclusion body proteins.* The FASEB Journal, 1996. **10**(1): p. 49-56.
179. Lobstein, J., et al., *SHuffle, a novel Escherichia coli protein expression strain capable of correctly folding disulfide bonded proteins in its cytoplasm.* Microbial cell factories, 2012. **11**(1): p. 753.

180. Klint, J.K., et al., *Production of recombinant disulfide-rich venom peptides for structural and functional analysis via expression in the periplasm of E. coli.* PloS one, 2013. **8**(5): p. e63865.
181. Johnson, B.A., S.P. Stevens, and J.M. Williamson, *Determination of the three-dimensional structure of margatoxin by 1H, 13C, 15N triple-resonance nuclear magnetic resonance spectroscopy.* Biochemistry, 1994. **33**(50): p. 15061-15070.
182. Escobar, L., M.J. Root, and R. MacKinnon, *Influence of protein surface charge on the bimolecular kinetics of a potassium channel peptide inhibitor.* Biochemistry, 1993. **32**(27): p. 6982-6987.
183. Ogata, K., H. Nishikawa, and M. Ohsugi, *A yeast capable of utilizing methanol.* Agricultural and biological chemistry, 1969. **33**(10): p. 1519-1520.
184. Cregg, J.M., T.S. Vedvick, and W.C. Raschke, *Recent advances in the expression of foreign genes in Pichia pastoris.* Nature Biotechnology, 1993. **11**(8): p. 905-910.
185. Türkanoğlu Özçelik, A., S. Yılmaz, and M. Inan, *Pichia pastoris promoters.* Recombinant Protein Production in Yeast, 2019: p. 97-112.
186. Cregg, J.M., *Introduction: distinctions between Pichia pastoris and other expression systems.* Methods in molecular biology (Clifton, NJ), 2007. **389**: p. 1-10.
187. Cereghino, J.L. and J.M. Cregg, *Heterologous protein expression in the methylotrophic yeast Pichia pastoris.* FEMS microbiology reviews, 2000. **24**(1): p. 45-66.
188. Macauley-Patrick, S., et al., *Heterologous protein production using the Pichia pastoris expression system.* Yeast, 2005. **22**(4): p. 249-270.
189. Anangi, R., et al., *Recombinant expression of margatoxin and agitoxin-2 in Pichia pastoris: an efficient method for production of KV1. 3 channel blockers.* PLoS One, 2012. **7**(12): p. e52965.
190. Borrego, J., et al., *Recombinant Expression in Pichia pastoris System of Three Potent Kv1. 3 Channel Blockers: Vm24, Anuroctoxin, and Ts6.* Journal of Fungi, 2022. **8**(11): p. 1215.
191. Yu, P., et al., *Codon optimisation improves the expression of Trichoderma viride sp. endochitinase in Pichia pastoris.* Scientific reports, 2013. **3**(1): p. 1-6.
192. Teng, D., et al., *Codon optimization of Bacillus licheniformis β-1, 3-1, 4-glucanase gene and its expression in Pichia pastoris.* Applied microbiology and biotechnology, 2007. **74**(5): p. 1074-1083.
193. Nordén, K., et al., *Increasing gene dosage greatly enhances recombinant expression of aquaporins in Pichia pastoris.* BMC biotechnology, 2011. **11**(1): p. 47.
194. Yu, M., S. Wen, and T. Tan, *Enhancing production of Yarrowia lipolytica lipase Lip2 in Pichia pastoris.* Engineering in Life Sciences, 2010. **10**(5): p. 458-464.
195. Beltrán-Vidal, J., et al., *Colombian Scorpion Centruroides margaritatus: Purification and Characterization of a Gamma Potassium Toxin with Full-Block Activity on the hERG1 Channel.* Toxins, 2021. **13**(6): p. 407.
196. Bergmans, H., I. Van Die, and W. Hoekstra, *Transformation in Escherichia coli: stages in the process.* Journal of bacteriology, 1981. **146**(2): p. 564-570.
197. Schägger, H., *Tricine–sds-page.* Nature protocols, 2006. **1**(1): p. 16-22.
198. Hamill, O.P., et al., *Improved patch-clamp techniques for high-resolution current recording from cells and cell-free membrane patches.* Pflügers Archiv, 1981. **391**: p. 85-100.
199. Peter Jr, M., et al., *Effects of toxins Pi2 and Pi3 on human T lymphocyte Kv1. 3 channels: the role of Glu7 and Lys24.* The Journal of membrane biology, 2001. **179**(1): p. 13-25.
200. Beeton, C., M. W Pennington, and R. S Norton, *Analogs of the sea anemone potassium channel blocker ShK for the treatment of autoimmune diseases.* Inflammation &

Allergy-Drug Targets (Formerly Current Drug Targets-Inflammation & Allergy)(Discontinued), 2011. **10**(5): p. 313-321.
201. Veytia-Bucheli, J.I., et al., *Kv1. 3 channel blockade with the Vm24 scorpion toxin attenuates the CD4+ effector memory T cell response to TCR stimulation.* Cell Communication and Signaling, 2018. **16**(1): p. 1-15.
202. Naseem, M.U., et al., *Optimization of Pichia pastoris expression system for high-level production of margatoxin.* Frontiers in pharmacology, 2021: p. 2454.
203. Marinkelle, C. and H. Stahnke, *Toxicological and clinical studies on Centruroides margaritatus (Gervais), a common scorpion in western Colombia.* Journal of medical entomology, 1965. **2**(2): p. 197-199.
204. Rezazadeh, S., et al., *An activation gating switch in Kv1. 2 is localized to a threonine residue in the S2-S3 linker.* Biophysical Journal, 2007. **93**(12): p. 4173-4186.
205. Balajthy, A., et al., *7DHC-induced changes of Kv1. 3 operation contributes to modified T cell function in Smith-Lemli-Opitz syndrome.* Pflügers Archiv-European Journal of Physiology, 2016. **468**(8): p. 1403-1418.
206. Wai, D.C.C., et al., *A Fluorescent Peptide Toxin for Selective Visualization of the Voltage-Gated Potassium Channel KV1.3.* Bioconjugate Chemistry, 2022. **33**(11): p. 2197-2212.
207. Beeton, C., et al., *Targeting effector memory T cells with a selective peptide inhibitor of Kv1. 3 channels for therapy of autoimmune diseases.* Molecular pharmacology, 2005. **67**(4): p. 1369-1381.
208. Panyi, G. and C. Deutsch, *Assembly and suppression of endogenous Kv1. 3 channels in human T cells.* The Journal of general physiology, 1996. **107**(3): p. 409-420.
209. Villalonga, N., et al., *Kv1. 3/Kv1. 5 heteromeric channels compromise pharmacological responses in macrophages.* Biochemical and biophysical research communications, 2007. **352**(4): p. 913-918.
210. Ogielska, E., et al., *Cooperative subunit interactions in C-type inactivation of K channels.* Biophysical Journal, 1995. **69**(6): p. 2449-2457.
211. Cremonez, C.M., et al., *Structural and functional elucidation of peptide Ts11 shows evidence of a novel subfamily of scorpion venom toxins.* Toxins, 2016. **8**(10): p. 288.
212. Mahjoubi-Boubaker, B., et al., *Kbot1, a three disulfide bridges toxin from Buthus occitanus tunetanus venom highly active on both SK and Kv channels.* Peptides, 2004. **25**(4): p. 637-645.
213. Abdel-Mottaleb, Y., et al., *A novel toxin from the venom of the scorpion Tityus trivittatus, is the first member of a new α-KTX subfamily*. FEBS letters, 2006. **580**(2): p. 592-596.
214. Stehling, E.G., et al., *Looking over Toxin–K+ Channel Interactions. Clues from the Structural and Functional Characterization of α-KTx Toxin Tc32, a Kv1. 3 Channel Blocker*. Biochemistry, 2012. **51**(9): p. 1885-1894.
215. Wu, B., et al., *Mapping the interaction anatomy of BmP02 on Kv1. 3 channel.* Scientific reports, 2016. **6**(1): p. 1-9.
216. Srinivasan, K.N., et al., *κ-Hefutoxin1, a Novel Toxin from the ScorpionHeterometrus fulvipes with Unique Structure and Function: IMPORTANCE OF THE FUNCTIONAL DIAD IN POTASSIUM CHANNEL SELECTIVITY*. Journal of Biological Chemistry, 2002. **277**(33): p. 30040-30047.
217. Feske, S., H. Wulff, and E.Y. Skolnik, *Ion channels in innate and adaptive immunity.* Annual review of immunology, 2015. **33**: p. 291-353.
218. Krishnarjuna, B., et al., *Structure, folding and stability of a minimal homologue from Anemonia sulcata of the sea anemone potassium channel blocker ShK.* Peptides, 2018. **99**: p. 169-178.

219. González-Castro, R., M.A. Gómez-Lim, and F. Plisson, *Cysteine-Rich Peptides: Hyperstable Scaffolds for Protein Engineering.* ChemBioChem, 2021. **22**(6): p. 961-973.
220. Tanner, M.R., et al., *Prolonged immunomodulation in inflammatory arthritis using the selective Kv1. 3 channel blocker HsTX1 [R14A] and its PEGylated analog.* Clinical Immunology, 2017. **180**: p. 45-57.
221. Bergmann, R., et al., *Distribution and kinetics of the Kv1.3-blocking peptide HsTX1[R14A] in experimental rats.* Scientific Reports, 2017. **7**(1): p. 3756.
222. Felipe, A., C. Soler, and N. Comes, *Kv1. 5 in the immune system: the good, the bad, or the ugly?* Frontiers in physiology, 2010. **1**: p. 152.
223. Gao, T., et al., *Temporal profiling of Kv1. 3 channel expression in brain mononuclear phagocytes following ischemic stroke.* Journal of Neuroinflammation, 2019. **16**(1): p. 1-11.
224. Tajti, G., et al., *The voltage-gated potassium channel KV1. 3 as a therapeutic target for venom-derived peptides.* Biochemical pharmacology, 2020: p. 114146.
225. Erdogan, A., et al., *Margatoxin inhibits VEGF-induced hyperpolarization, proliferation and nitric oxide production of human endothelial cells.* Journal of vascular research, 2005. **42**(5): p. 368-376.
226. Tubert, C., et al., *Decrease of a current mediated by Kv1. 3 channels causes striatal cholinergic interneuron hyperexcitability in experimental parkinsonism.* Cell reports, 2016. **16**(10): p. 2749-2762.
227. Toldi, G., et al., *Calcium Influx Kinetics and the Characteristics of Potassium Channels in Peripheral T Lymphocytes in Systemic Sclerosis.* Pathobiology, 2020. **87**(5): p. 311-316.
228. Schwartz, A.B., et al., *Olfactory bulb-targeted quantum dot (QD) bioconjugate and Kv1. 3 blocking peptide improve metabolic health in obese male mice.* Journal of Neurochemistry, 2020.
229. Anangi, R., et al., *Recombinant Expression of Margatoxin and Agitoxin-2 in Pichia pastoris: An Efficient Method for Production of KV 1.3 Channel Blockers.* PLoS One, 2012. **7**(12): p. e52965.
230. Li, Y., et al., *Improvement of Aspergillus sulphureus endo-β-1, 4-xylanase expression in Pichia pastoris by codon optimization and analysis of the enzymic characterization.* Applied biochemistry and biotechnology, 2010. **160**(5): p. 1321-1331.
231. Yadava, A. and C.F. Ockenhouse, *Effect of codon optimization on expression levels of a functionally folded malaria vaccine candidate in prokaryotic and eukaryotic expression systems.* Infection and immunity, 2003. **71**(9): p. 4961-4969.
232. Wang, J.-R., et al., *Codon optimization significantly improves the expression level of α-amylase gene from Bacillus licheniformis in Pichia pastoris.* BioMed research international, 2015. **2015**.
233. Clare, J., et al., *High-level expression of tetanus toxin fragment C in Pichia pastoris strains containing multiple tandem integrations of the gene.* Bio/technology, 1991. **9**(5): p. 455-460.
234. Mansur, M., et al., *Multiple gene copy number enhances insulin precursor secretion in the yeast Pichia pastoris.* Biotechnology letters, 2005. **27**(5): p. 339-345.
235. Vassileva, A., et al., *Expression of hepatitis B surface antigen in the methylotrophic yeast Pichia pastoris using the GAP promoter.* Journal of biotechnology, 2001. **88**(1): p. 21-35.
236. Nordén, K., et al., *Increasing gene dosage greatly enhances recombinant expression of aquaporins in Pichia pastoris.* BMC biotechnology, 2011. **11**(1): p. 1-12.

237. Sunga, A.J., I. Tolstorukov, and J.M. Cregg, *Posttransformational vector amplification in the yeast Pichia pastoris.* FEMS yeast research, 2008. **8**(6): p. 870-876.
238. André, N., et al., *Enhancing functional production of G protein-coupled receptors in Pichia pastoris to levels required for structural studies via a single expression screen.* Protein Science, 2006. **15**(5): p. 1115-1126.
239. Khatri, N.K. and F. Hoffmann, *Oxygen-limited control of methanol uptake for improved production of a single-chain antibody fragment with recombinant Pichia pastoris.* Applied microbiology and biotechnology, 2006. **72**(3): p. 492-498.
240. Minjie, G. and S. Zhongping, *Process control and optimization for heterologous protein production by methylotrophic Pichia pastoris.* Chinese journal of chemical engineering, 2013. **21**(2): p. 216-226.
241. Mu, X., et al., *High-level expression, purification, and characterization of recombinant human basic fibroblast growth factor in Pichia pastoris.* Protein Expression and Purification, 2008. **59**(2): p. 282-288.
242. Zhang, T., et al., *Optimization for high-level expression of the Pichia guilliermondii recombinant inulinase in Pichia pastoris and characterization of the recombinant inulinase.* Process Biochemistry, 2009. **44**(12): p. 1335-1339.
243. Kobayashi, K., et al., *Addition of oleic acid increases expression of recombinant human serum albumin by the AOX2 promoter in Pichia pastoris.* Journal of bioscience and bioengineering, 2000. **89**(5): p. 479-484.
244. Park, E.Y., *Enhanced production of mouse α-amylase by feeding combined nitrogen and carbon sources in fed-batch culture of recombinant Pichia pastoris.* Process biochemistry, 2006. **41**(2): p. 390-397.
245. Çalık, P., et al., *Influence of pH on recombinant human growth hormone production by Pichia pastoris.* Journal of Chemical Technology & Biotechnology, 2010. **85**(12): p. 1628-1635.
246. Brierley, R.A., G.R. Davis, and G.C. Holtz, *Production of insulin-like growth factor-1 in methylotrophic yeast cells*. 1994, Google Patents.
247. Chang, S.C., et al., *N-terminally extended analogues of the K+ channel toxin from Stichodactyla helianthus as potent and selective blockers of the voltage-gated potassium channel Kv1. 3.* The FEBS journal, 2015. **282**(12): p. 2247-2259.

9. KEY WORDS

Voltage-gated potassium channel

Kv1.3

Autoimmune diseases

Scorpion toxins

Margatoxin

HsTX1 toxin

Fluorescent-labeled toxin

Patch-clamp electrophysiology

Flow cytometry

Recombinant protein production

Yeast expression system

HPLC

10. ACKNOWLEDGEMENT

All praise to Allah Almighty and thanks to Him Who bestowed me with lucid intelligence and energy to complete my PhD dissertation.

I appreciate my supervisor, Prof. Dr. György Panyi, for his support over the five years of my PhD. For the time, the experiences, and the knowledge he invested in supervising this scientific work. For all the doors he opened for me and the experiences and skills I acquired in his lab. For his big trust and for giving me enough space to think, to learn and to structure my work according to my own vision and interest.

I also would like to thank all the kind and collaborative colleagues in my lab. Special thanks to Dr. Tibor G. Szántó for his guidance in learning patch-clamp, Dr. Tajti Gábor for help in learning T-cell assays and Dr. Jesus Borrego for help and fruitful discussion regarding recombinant peptide production. And to our golden technical lab assistants Cecilia Nagy and Adrienn Bagosi who make great efforts to set our working environment always to perfect.

A big thank to our collaborators at UNAM, Mexico Prof. Lourival D. Possani's laboratory members and at Monash University, Australia Prof. Raymod S. Norton's laboratory for providing us peptide toxins.

Thanks for the workers at the faculty of Medicine, Doctoral School of Molecular Medicine, and especially at the department of Biophysics and Cell Biology for offering the researchers a great environment to do their research, equipped labs, and qualified staff.

Finally, I express my deepest appreciations to my family, especially to my mother and my wife Kashmala Shakeel, who never gave up on me and have always supported me.

The experimental work was supported by the following research grants from Hungarian National Research, Development, and Innovation Office: K143071, K119417, EFOP-3.6.1-16-2016-00022 and GINOP2.3.2-15-2016-00044. The doctoral training program was supported by Tempus Public Foundation and the Stipendium Hungaricum scholarship.

11. APPENDIX

UNIVERSITY of DEBRECEN

UNIVERSITY AND NATIONAL LIBRARY
UNIVERSITY OF DEBRECEN
H-4002 Egyetem tér 1, Debrecen
Phone: +3652/410-443, email: publikaciok@lib.unideb.hu

Registry number: DEENK/40/2023.PL
Subject: PhD Publication List

Candidate: Muhammad Umair Naseem
Doctoral School: Doctoral School of Molecular Medicine

List of publications related to the dissertation

1. Wai, D. C. C., **Naseem, M. U.**, Mocsár, G., Babu Reddiar, S., Pan, Y., Csóti, Á., Hajdu, P., Nowell, C., Nicolazzo, J. A., Panyi, G., Norton, R. S.: A Fluorescent Peptide Toxin for Selective Visualization of the Voltage-Gated Potassium Channel Kv1.3.
   Bioconjugate Chem. 33 (11), 2197-2212, 2022.
   DOI: http://dx.doi.org/10.1021/acs.bioconjchem.2c00436
   IF: 6.069 (2021)
2. **Naseem, M. U.**, Carcamo-Noriega, E., Beltrán-Vidal, J., Borrego, J., Szántó, G. T., Zamudio, F. Z., Delgado-Prudencio, G., Possani, L. D., Panyi, G.: Cm28, a scorpion toxin having a unique primary structure, inhibits KV1.2 and KV1.3 with high affinity.
   J. Gen. Physiol. 154 (8), 1-18, 2022.
   DOI: http://dx.doi.org/10.1085/jgp.202213146
   IF: 4 (2021)
3. **Naseem, M. U.**, Tajti, G., Gáspár, A., Szántó, G. T., Borrego, J., Panyi, G.: Optimization of Pichia pastoris Expression System for High-Level Production of Margatoxin.
   Front. Pharmacol. 12, 1-18, 2021.
   DOI: http://dx.doi.org/10.3389/fphar.2021.733610
   IF: 5.988

List of other publications

4. **Naseem, M. U.**, Gurrola-Briones, G., Romero-Imbachi, M. R., Borrego, J., Carcamo-Noriega, E., Beltrán-Vidal, J., Zamudio, F. Z., Shakeel, K., Possani, L. D., Panyi, G.: Characterization and Chemical Synthesis of Cm39 (α-KTx 4.8): a Scorpion Toxin That Inhibits Voltage-Gated K+ Channel KV1.2 and Small- and Intermediate-Conductance Ca2+-Activated K+ Channels KCa2.2 and KCa3.1.
   Toxins. 15 (1), 1-21, 2023.
   DOI: http://dx.doi.org/10.3390/toxins15010041
   IF: 5.075 (2021)

UNIVERSITY AND NATIONAL LIBRARY
UNIVERSITY OF DEBRECEN
H-4002 Egyetem tér 1, Debrecen
Phone: +3652/410-443, email: publikaciok@lib.unideb.hu

5. Bosire, R., Fadel, L., Mocsár, G., Nánási, P. P. i., Sen, P., Sharma, A. K., **Naseem, M. U.**, Kovács, A., Kugel, J., Kroemer, G., Vámosi, G., Szabó, G.: Doxorubicin impacts chromatin binding of HMGB1, Histone H1 and retinoic acid receptor.
Sci. Rep. 12 (1), 1-14, 2022.
DOI: http://dx.doi.org/10.1038/s41598-022-11994-z
IF: 4.996 (2021)

6. Borrego, J., **Naseem, M. U.**, Sehgal, A. N. A., Panda, L. R., Shakeel, K., Gáspár, A., Nagy, C., Varga, Z., Panyi, G.: Recombinant Expression in Pichia pastoris System of Three Potent Kv1.3 Channel Blockers: Vm24, Anuroctoxin, and Ts6.
J. Fungi. 8 (11), 1-15, 2022.
DOI: http://dx.doi.org/10.3390/jof8111215
IF: 5.724 (2021)

7. **Naseem, M. U.**, Ahmed, N., Khan, M. A., Tahir, S., Zafar, A. U.: Production of potent long-lasting consensus interferon using albumin fusion technology in Pichia pastoris expression system.
Protein Expr. Purif. 166, 1-8, 2020.
DOI: http://dx.doi.org/10.1016/j.pep.2019.105509
IF: 1.65

Total IF of journals (all publications): 33,502
Total IF of journals (publications related to the dissertation): 16,057

The Candidate's publication data submitted to the iDEa Tudóstér have been validated by DEENK on the basis of the Journal Citation Report (Impact Factor) database.

10 February, 2023

DEBRECENI EGYETEM * Egyetemi és Nemzeti Könyvtár *